INVESTIGATING AND MODELING THE MECHANICAL CONTRIBUTIONS TO TRAUMATIC BRAIN INJURY IN CONTACT SPORTS AND CHRONIC NEURAL IMPLANT PERFORMANCE

A Dissertation

Submitted to the Faculty

of

Purdue University

by

Roy J. Lycke

In Partial Fulfillment of the

Requirements for the Degree

of

Doctor of Philosophy

May 2019

Purdue University

West Lafayette, Indiana

THE PURDUE UNIVERSITY GRADUATE SCHOOL
STATEMENT OF DISSERTATION APPROVAL

Dr. Eric Nauman, Chair

School of Mechanical Engineering and

Weldon School of Biomedical Engineering

Dr. Thomas Talavage

School of Electrical and Computer Engineering and

Weldon School of Biomedical Engineering

Dr. Edward Bartlett

School of Biology and

Weldon School of Biomedical Engineering

Dr. Lia Stanciu

School of Materials Engineering

Approved by:

Dr. George Wodicka

Head of the Weldon School of Biomedical Engineering

I am a simple man who just wants to help others. May these works and those to follow help my fellow man, and pray my words fork lightning before the night.

ACKNOWLEDGMENTS

I'd like to give thanks to those who have helped me grow into the researcher I am today. I'd like to begin by thanking Dr. Eric Nauman who accepted me into his lab when the Otto Lab disbanded, who shared his engineering insights and expertise with me over the years, and through self example showed me what it is to truly be an ethical engineer.

I'd like to thank all the graduate and undergraduate students in the HIRRT Lab. I am glad for all I've learned, all that I've been able to teach, and for the friendships we've forged, in particular Taylor Lee, Kevin McIver, Michael Dziekan, Nicolas Leiva, and Ninad Trifale.

Finally, I would like to thank the members of the Otto Lab, now scattered to the wind but who taught me so much. In particular Ryan Verner, Matt McDermott, Hayden Carney, Andrew Ready and Dr. Kevin Otto who started me on my path at Purdue.

TABLE OF CONTENTS

Page

Page

Page

LIST OF TABLES

LIST OF FIGURES

Figure Page

ABBREVIATIONS

CNS	Central Nervous System
CSF	Cerebral Spinal Fluid
CTE	chronic traumatic encephalopathy
DBS	Deep Brain Stimulation
DMN	Default Mode Network
DTI	Diffusion tensor imaging
ECoG	Electrocorticography
fMRI	Functional Magnetic Resonance Imaing
GFAP	Glial fibrillary acidic protein
HAE	Head Acceleration Events
MMP	matrix metalloproteinases
MRI	Magnetic Resonance Imaging
MRS	Magnetic Resonance Spectroscopy
NET	Nanoelectronic Thread
NGF	Neural Growth Factor
OCD	Obsessive Compusive Disorder
PEDOT	Poly 3,4-ethylene dioxythiophene
SNR	Signal to Noise Ratio
TBI	Traumatic Brain Injury

ABSTRACT

Lycke, Roy J. Ph.D., Purdue University, May 2019. Investigating and Modeling the Mechanical Contributions to Traumatic Brain Injury in Contact Sports and Chronic Neural Implant Performance . Major Professor: Eric A. Nauman.

Mechanical trauma to the brain, both big and small, and the method to protect the brain in its presence is a crucial field of research given the large population exposed to neuronal trauma daily and the benefit available through better understanding and injury prevention. A population of particular interest and risk are youth athletes in contact sports due to large accelerations they expose themselves to and their developing brains. To better monitor the risk these athletes are exposed to, their accumulation of head acceleration events (HAEs), a measure correlated with harmful neurological changes, was tracked over sport seasons. It was observed that few significant differences in HAEs accumulated existed between players of ages from middle school to high school, but there did exist a difference between sports with girls' soccer players accumulating fewer HAEs than football players. This highlights to risk youth athletes are exposed to and the importance of improved technique and individual player size. To better monitor HAEs for each individual, a novel head segmentation program was developed that extracts player specific geometries from a single T1 MRI scan that can improve the accuracy of HAE monitoring. Acceleration measures processed with individualized head model versus those using a standardized head model typically displayed higher accelerations, highlighting the need for individualized measure for accurate monitoring of HAEs and risk of neurological changes. In addition to the large accelerations present in contact sports, the small but constant strains produced by neural implants embedded in the brain is also an important field of neuro-mechanical research as the physical properties of neural implants have been

found to contribute to the chronic immune response, a major factor preventing the widespread implementation of neural implants. To reduce the severity of the immune response and provide improved chronic functionality, researchers have varied neural implant design and materials, finding general trends but not precise relationships between the design factors and how they contribute the mechanical strain in the brain. Performing a large series of mechanical simulations and Cotter's sensitivity analyses, the relationships between neural design factors and the stain they produce in the brain was examined. It was found that the direction which neural implants are loaded contributes the most to the strain produced in the brain followed by the degree of bonding between the brain and the electrode. Directly related to the design of electrodes themselves, it was found that in most cases reducing the cross-sectional area of the probe resulted in a larger decrease of mechanical strain compared to softening the implant. Finally, a study was performed quantifying the resting micromotion of the brain utilizing a novel method of soft tissue micromotion measurement via microCT, applicable within the skull and the throughout the rest of the body.

1. INTRODUCTION

The brain is the center of thought, the origin of all our actions, the matter that makes us who we are, and, as it turns out, quite prone to injury. The importance of the brain cannot be understated as it makes us who we are and all other organs serve to nourish, protect, or follow the commands sent by the brain. It's logical then that people would take great efforts to protect their brains, but individuals put their brains at risk every day, in big and small ways. Of particular interest are the mechanical forces that the brain is exposed to and the damage they can result.

Chief among the ways that the brain can be injured is by exposure to impact, blastwave, or whiplash forces that induce traumatic brain injuries (TBIs). From blast waves and shrapnel experienced by soldiers, to punches to the head by pugilists, from head to head impacts over a season of football, to even just falling from a bike, there are a plethora of incidents that can subject the brain to forces that can cause neurological damage. But in recognizing these dangers, people have developed methods to protect themselves and their brains, by utilizing helmets, padding, and techniques or safety guards that can minimize our exposure to injury. But many of the existing safety measures do not adapt to the changing world or are insufficient at providing complete protection.

One particular interest in the current era of brain imaging and initiatives pushing for healthy brains and mental health is TBI in athletics. In recent years, the concern of brain health in contact sports has become more active in public discourse due to advances in TBI research and high publicity cases of retired football players exhibiting chronic traumatic encephalopathy (CTE), a neurodegenerative disease characterized by the shrinking of the brain (state specific regions) and an increase in aggression, forgetfulness, depression, and even suicidal tendencies. Due to a large number of amateur and professional athletes in the US who are involved in contact sports and

at risk for neurological damage, it is paramount that methods to protect and prevent damage through observation be developed and implemented.

From our research on youth football athletes, we observed player exposure to head accelerations is not dependent on the level of play from the middle school through the high school level, indicating that middle school athletes need to take more protective measures to reduce their risk of neurological damage. This is also concerning since the consequences of sustaining TBI at younger ages may lead to more severe and long-lasting consequences.

The second finding of our recent research is that to properly monitor player impact exposure, a personalized system must be used. In an effort to track head impacts and stop the accrual of asymptomatic brain trauma before injury occurs, a number of companies and research groups have developed systems to monitor head accelerations, but a common trend with these systems is their generalized approach to calculating the accelerations experienced by an individual. Due to variations in head size, tissue composition, and sensor placement, a uniform measure for each player is insufficient. To properly track the accumulation of accelerations sustained by the brain, a personalized model should be used for each individual player. Researchers have developed a system to quantify individual head metrics and generate models for simulations and investigations into the mechanisms underlying the accelerations and forces each player is exposed to.

From this investigation on TBI, one might think that trauma to the brain is limited to the massive blows to the head as encountered on the field of play, but some trauma is the result of microscopic medical interventions seeking to heal, in particular, neural implants. Since the brain is the core of who we are and controls all other bodily functions, it has long been a prime target to interface with for medical interventions. Regretfully, current neural implants may cause harm and actively limit the research and medical interventions that can be achieved.

Neural implants, devices which allow for the stimulation of the brain or recording of brain activity, are a young and developing technology which hold great potentials

for improving the quality of life for large sections of the population. Their primary benefit is as a potential treatment for a bevy of neurological, sensory, and neuromuscular disorders that do not respond well to traditional medical interventions but could be corrected with neural stimulation, similar to cochlear implant or auditory brainstem stimulators for hearing. Thus, with such potential, the current lack of implementation of neural implants is an area of unrealized advancement.

In general, neural implants can interface well with the brain and in a variety of ways, from detecting local field potentials down to resolving the firing of individual neurons in real time. But this interface does not last and most devices being to fail after few weeks or months after implantation due in large part to the brain's immune response to the implanted device. To solve this limitation and create chronically functioning neural implants, researchers have tried hundreds of novel and creative neural implant design, materials, and drug/protein coatings but with little success. One aspect of neural implants that has not received much attention though and may be key for creating a stable brain-machine interface is the physical properties of the probe and how it can be altered to reduce the mechanical strain it imparts on the brain and thus optimize its function within the brain.

In the endeavor to better understand the impact that neural implant design has on the strain in the brain, and by extension the chronic immune response, several neural implant design properties were investigated and revealed trends that may lead toward a device optimized for chronic implanted functionality. The most notable finding was that the orientation of brain motion relative to the probe was the most sensitive factor contributing to the strain imparted by an implanted electrode. Second to this was the bonding of the probe to the brain, in which a higher degree of bonding produced larger strain values and affected more local tissue than less bonded probes. This is concerning though as both micromotion and electrode to brain bonding are currently ill-defined for existing animal models and if future models are to accurately model the in vivo electrode to brain environment, they must be accurately and thoroughly quantified. It was also found that to reduce strain, neural implant design should focus

on reducing device cross-sectional area before stiffness as implant size was found to be more sensitive relative to other factors when regarding electrode induced strain in the brain. This agrees with recent studies which found chronically functioning electrode designs with cross-sectional areas less than 50 μm demonstrate unparalleled chronic function, indicating that researchers approach novel electrode design utilizing optimization rather than developing new designs based on trends alone which are often ill-suited for comparisons due to confounded changes in design elements.

To that end, a study developing a methodology to quantify the brain micromotion in rats utilizing a novel technique to measure soft tissue deformations of the brain via microCT was performed. In brief, radiopaque markers were implanted in the brain at different relevant regions to quantify the micromotion throughout the brain in three dimensions over the course of the wound healing process. The developed micromotion imaging process avoids the confounds inherent from surgically removing the skull and measuring the brain as we previously performed and opens a new avenue of research to quantify soft tissue motion throughout the body in a relatively non-invasive manner, only requiring the injection of microbeads.

2. BACKGROUND

The brain is subject to a wide variety of forces that can cause damage, disrupt neurological function, or prevent medical interventions for working. In this paper, two sources of disruptive strain on the brain are detailed: traumatic brain injuries acquired during contact sports and the mechanical perturbation of implanted neural electrodes upon the brain.

2.1 Brain Injury in Contact Sports

Since there have been humans there's been humans hitting their heads and subsequently injuring their brain. As time has marched on, new and different past-times in athletics have entered the daily lives of humanity, some of which have the risk of injuring the brain. Of particular interest is traumatic brain injury (TBI) that occurs during contact sports such as boxing, football, and soccer. While a number of injuries can befall an athlete during play in contact sports, brain injuries, concussions, and chronic traumatic encephalopathy (CTE) are of particular interest given their severe impact on quality of life and recent public interest [1, 2].

CTE is a progressive neurodegenerative disease marked physically by a decrease in white matter and grey matter volume and expansion of the cerebral spinal fluid (CSF) and ventricles causing mental changes such as memory loss, parkinsonism, poor impulse control, aggression, dementia, depression, and suicidal behavior [1]. First observed in pugilists in the 1920's and called "punch drunk" at the time [3], CTE has gained public attention in recent years due to a string of high profile football players diagnosed with CTE posthumously (Figure 2.1). As a result research has focused on understanding and developing methods to prevent CTE in athletes across various sports [4, 5]. While originally many tied the risk of CTE development to a

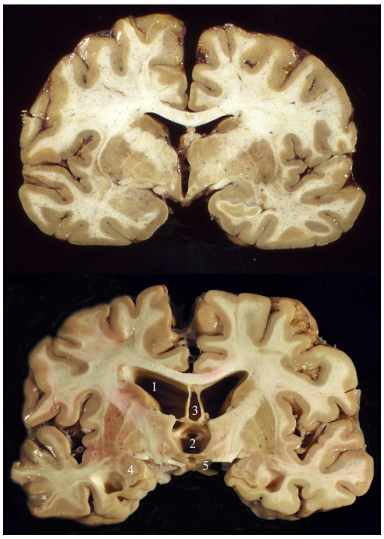

Fig. 2.1. The coronal section of normal brain (top), and a brain from a retired professional football player (bottom) showing the characteristic gross pathology of CTE. Figure retrieved from [1]

history of concussions, it has been found that repeated head trauma, most of which are asymptomatic, is correlated with an increased change in neurological morphology and function, and by extension CTE [6–9].

The impact of this revelation is that an extremely large population is at risk of neurological injury due to TBI. Each year 1.6-3.8 million sports-related TBIs are reported in the US each year and in 2010 alone the estimated lifetime total costs due to TBI was $76.5 billion [10]. Though it should be noted that the number of individuals and costs to the public are of likely underestimates due to the under-reporting of symptoms and difficulty in diagnosing TBI outside of the symptomatic cases [11]. While the precise number of those affected by CTE is unknown due to the difficulty in diagnosing CTE and the biased sample surveyed, concussion rates are used instead to approximate the populations most at risk of developing potentially long-lasting neurological impairments since both populations share a history of repetitive head trauma. It is known that each year 2.4 per 10,000 adolescent athletes experience concussions, with football players sustaining 6 diagnosed concussions per 10,000 [12].

Other sports with high rates of concussions include boys lacrosse and girls soccer with 3.0 per 10,000 and 3.5 per 10,000 respectively. This illustrates a large population at risk from developing neurological changes, trauma, and injury potentially resulting CTE without an effective means of treatment or prevention.

The risk of developing CTE over the course of an athlete's career and the hazards inherent with repeated concussions highlights an especially vulnerable population of adolescent athletes whose brains are still developing and are especially susceptible to brain damage [2]. The need to understand the mechanisms underlying TBI in adolescents has led to a number of youth monitoring studies in which athletes are observed during the normal activity of play and in response to injury events such as concussions [13]. But, while many researchers have examined subjects during and after their game seasons in an endeavor to quantify neurological change and possible damage, researchers with the Purdue Neurotrauma Group (PNG) have developed a methodology to quantify the functional state of the brain before and after a game season to quantify the change from resting baseline [4,5,14]. This approach allows for the individual neurological changes for each player as measured by magnetic resonance imaging (MRI) & functional MRI (fMRI) to be quantified and correlated to the respective player's accumulated hits over the season, providing in-depth insight to the brain's response to accumulated hits.

From research examining the effects of the accumulation of head acceleration events (HAEs) over time, it has been observed via fMRI that the brain has a profound response after only one season. When exposed to repeated head accelerations, a player without any concussion symptoms, thus not clinically diagnosed with a concussion, and one with a diagnosed concussion display similar changes in neurological activity patterns. And both players are significantly altered from their respective pre-season brain activity [4] or compared to non-contact athletes like runners. MRI has also been used to detect changes in fraction anisotropy in white matter via diffusion tensor imaging (DTI) [15], concentrations of metabolites in the brain via magnetic resonance

spectroscopy (MRS), and the number of connections in the default mode network (DMN) via resting state-fMRI [16–18].

While all these observations paint the act of playing in contact sports as dire, the brain can heal over days, weeks, and months depending on the severity and if the athlete takes the appropriate time to heal [19]. Though if athletes do not allow for recovery, the result will likely lead to permanent neurological changes and possibly resulting in CTE. Thus to protect athletes, it is crucial to determine when they have accumulated more HAEs and strains on their brain that is safe and need to either take time off or change play style to protect themselves. To this end, the HAEs for each player needs to be monitored to quantify their exposure and implement appropriate preventative measures (recovery periods or changes in play technique).

Another concern with the current approaches in monitoring HAEs is the use of acceleration and force measures based off averaged player body sizes rather than individualized measures. This is because averaged measures may be insufficient or inaccurate, as occurred when the US air force failed to heed the flaw of averages [20]. In short, during the 1940s and 50's the US air force was having issues with well-trained pilots crashing at an alarming rate due to their inability to control their aircraft. It was proposed that many pilots could not properly access all the cockpit controls even though it was designed to fit the ideal body of a pilot averaged from thousands of active airmen. Problem was, out of the 4,063 pilots measured to design the cockpit, not a single one fit within the average range on all 10 dimensions leading to a cockpit that fitted no one. Once adjustable fittings and instruments were implemented the air force saw a dramatic improvement and adjustable equipment has been the standard since. This historical example shows that even with an accurate measure for an averaged individual, the mean may not match any subjects and such is the concern with many existing acceleration measurement systems that use an averaged model for calculating the transformed accelerations measured at the sensor to those experienced by an athlete's brain. It is already documented that there exits considerable head size variability between players of the same and different age groups or genders [21–23] and

not accounting for this could lead to cases of overestimating exposure to accelerations during play, or more dangerously, underestimating exposure. This highlights the need to accurately measure the head geometries for individual players to accurately measure the accelerations they are experiencing for both accurate monitoring, safe preventative care, and more accurate design criteria for protective equipment.

2.2 Neural Implants

Neural implants are devices designed to interface between computers and the nervous system. They offer a potential method for treating a wide variety of disorders and disabilities by providing stimulation where it is lacking or corrective stimulation to establish normal brain function. In brief, neural implants are designed to record brain activity, stimulate, or both, most often via electrical stimulation.

First developed and approved for use in human brains, deep brain stimulation (DBS) electrodes have been used to treat Parkinson's disease since 2002 and obsessive-compulsive disorder (OCD) since 2009, helping to improve the quality of life for thousands of people every day [24–28]. These devices have been explored to treat a wide range of other conditions such as obesity, depression, and dystopia [29, 30]. This demonstrates the great potential for neural implants given even the simplest designed electrode can accomplish so much, then more complex electrodes with higher resolution, more channels, and more dynamic signaling have the possibility to treat so many more disorders.

Since the primary aim of neural implants is to serve as a treatment for neurological and physical diseases or disorders that are not well managed by existing therapies, there exists a large population which would benefit from neural implant derived treatments. Conditions such as blindness and retinitis pigmentosa which currently affects 1.2 million and 50,000 to 100,000 individuals, respectively, have no treatment aside from donor organs [31, 32]. Similarly, 30 million are afflicted with bilateral hearing loss [33] and of those 12,000 have neurofibromatosis type 2 [34] which can not benefit

from the existing cochlear implants or other peripheral neural stimulators. And then there are the many affected by lack of motor control such as the 5.5 million suffering from paralysis, [35, 36], 1.5 million Americans with limb loss [37], approximately 116,000 with muscular dystrophy [38], all of which currently have little in the way of restorative treatments. This represents a massive, and most likely underestimated, the population of those who could gain or restore bodily function with the development of advanced neural prosthetics. While neural implants posses the possibility to treat these conditions and expand the medical field, they have been limited in one crucial aspect: their ability to function chronically.

2.2.1 Neural Implant Failure

Initially, after implantation, neural implants are able to record neural activity with low noise and stimulate local neural networks efficiently, but over time they begin to fail [39, 40]. After a few days in vivo, the electrical impedances for implant contact sites to the brain begin to rise indicating electrical insulation forming between the implant and the brain [41]. As a result of this insulation, the amplitude of recorded neuron activity begins to fall and background noise rises, lowering the overall signal to noise ratio (SNR) of the observed brain activity making monitoring of brain activity difficult [42]. In the first several weeks post-implantation, this increase in impedance and drop in SNR is rapid, but after several weeks or months post-implantation, the rate of signal degradation slows and almost plateaus, yet device performance still decreases. Over the following weeks and months, the observed neural activity becomes indistinguishable from the background noise. Eventually, most, if not all, contact sites on the neural implant are rendered useless due to the inability to electrically interact with neurons or due to breakage.

Neural implant failure has also demonstrated a sporadic and unpredictable pattern post-implantation which further complicates the chronic implementation of neural implants and methods developed to mitigate device failure. Williams et al. showed that

different electrode sites within the same animal can evoke small or large immune responses resulting in normal or impaired function, respectively, although all sites are from the same implant and only a few hundred micrometers apart [43]. Likewise, McConnell et al. found that site performance varied over time, with some sites demonstrating on-and-off functionality (working some days but not others), and others sites silent for weeks only to function again for a few days at a time [44]. Additionally, studies using identical electrodes, in the same manner, can have substantially different performance and failures rates, such as 20% site failure [42] versus 80% after a month implanted [45], further emphasizing the sporadic nature of the immune response. This sporadic failure even extends to the human studies done thus far and their reliance on complex signal analysis software to calculate motor commands from small neurons, even though motor neuron commands have been defined in previous studies [46, 47]. Additionally, different devices produce a variety of different immune responses from the brain due to factors such as device design, material composition, device coating, or location of implantation making generalizations regarding the electrode induced immune response difficult due to the confounded nature of the studies [42, 45, 48–51].

The ubiquitous neural implant failure has prompted researchers to investigate the brains immune response to implanted devices, in particular, the development of a layer of immune cells that surround the implanted device called the "glial sheath" and the loss of neurons near the implant [52]. By understanding the immune response, researchers can develop techniques to avoid and treatments to reduce the severity of the immune reaction and improve the chronic performance of neural implants.

2.2.2 Neural Implant Immune Response

The immune response begins when a penetrating neural electrode is inserted into the brain, cutting and compressing cortical tissue and damaging the local neurovasculature. As a result of this initial injury to the central nervous system (CNS), local vasculature networks are disrupted hampering the supply of nutrients to local cells

while bleeding into the insertion track [53]. Neurons, microglia, astrocytes, & oligodendrocytes directly rupture, releasing a wash of cytokines and messenger molecules which signal the local microglia population and begin the immune response [54]. Microglia are the primary immune cells of the CNS and usually are in a ramified state with projections in a stellate formation monitoring the state of the surrounding tissue [55, 56]. In response to an implant injury, the microglia activate, becoming amoeboid and begin migrating toward the injury site within hours [57–59]. At the injury site, the microglia phagocytize local cellular debris and foreign matter, but also release neurotoxins which can kill off local neurons during early reactive response [60]. Additionally, microglia release cytokines and signaling molecules which recruit astrocytes to the injury site, further progressing the immune response [54].

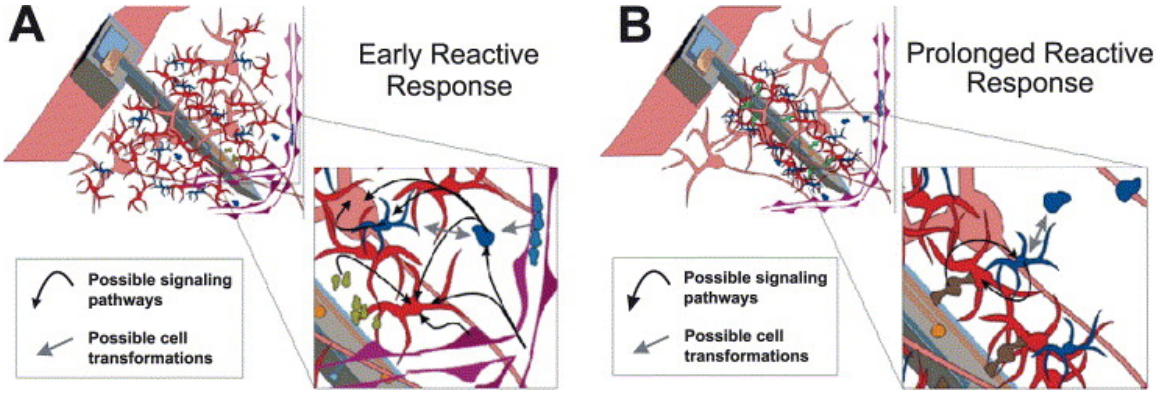

Fig. 2.2. Illustrations depicting cellular responses during early (A) and sustained (B) reactive responses observed following device insertion. The early response (A) is characterized by a large region containing reactive astrocytes and microglia around inserted devices. The sustained response (B) is characterized by a compact sheath of cells around insertion sites. Inserts depict potential cell-cell interactions and signaling pathways. Neurons (pink), astrocytes (red), monocyte-derived cells including microglia (blue), and vasculature (purple) are depicted. Figure retrieved from [61]

Signaled by the microglia, astrocytes migrate toward the injury site approximately one week after the initial injury [61] and change their morphology to a reactive hypertrophic state [54]. While the astrocytes are still migrating, microglia begin to phago-

cytize the implant but are unable to break down the implant due to the material properties of the device, thus causing them to enter a state of fatigued phagocytosis [62]. In this state, the microglia adhere to the surface of the implant and form multinucleated cells encapsulating the implant. After 4 weeks there is a substantial population of astrocytes around the injury site, and after 6 weeks there is a loose glial sheath formed primarily of activated astrocytes slowly constricting and releasing neural growth proteins [60, 62]. As they reach the injury site, astrocytes attempt to phagocytize the implant and upon failure to remove the implant, enter a state of fatigue phagocytosis, creating a tight network of interwoven activated astrocytes around the implant [62–64]. These astrocytes and the microglia create a thick layer of glial cells referred to as the glial sheath [65] which isolates the implant from the brain (Figure 2.2). The glial sheath extends tens to hundreds of micrometers away from the implant depending on the severity of the immune response [52, 64, 66].

This glial sheath is composed of different cell types with non-uniform spatial concentrations. Microscopy studies have shown that anti-CD68 antibody ED1 positive cells, macrophages, are highest in concentration immediately adjacent to the implant, less than 25 μm from the surface of the implant , whereas vimentin positive cells, activated astrocytes, peak in concentration between 25 to 50 μm away and GFAP positive cells, mature astrocytes, peak between 50 to 100 μm away from the implant [54,67,68]. This variation in cell concentration and morphology also extends along the length of the electrode [69] where it has been observed that higher concentrations of glial cells and meningeal cells are present at the surface of the implant and fewer deeper within the brain indicating cellular in-growth from the meninges.

In addition to killing off local neurons and creating a physical barrier around the implant, the glial sheath electrically insulates the implant from the surrounding neural tissue [66, 70–72]. This layered collection of microglia and astrocytes creates both a physical and electrical barrier which increase the impedance between the electrode and local neurons, effectively reducing the amplitude of electrical signals passing through the sheath and distorting the stimulation waveform due to capacitive nature

of the glial sheath [73]. This impedance has been modeled to relate the changes in complex impedance to changes in the cellular structure of the glial sheath and the electrode contact site due to the immune response [74–76]. Even with models that describe the impedance of the glial sheath, researchers are investigating how individual cell types contribute to the impedance changes and the tissue response such as Frampton et al., who evaluated the contribution of microglia and astrocytes to the impedance [70]. This study found that increasing microglia density increased overall impedance and increasing the astrocyte density had no effect on impedance, as we would expect given Williams et al. [76]. However, this study was an in vitro analysis and the cellular scaffold resembled a growing culture rather than an in vivo immune response. Observing the time course of the impedance changes in vivo as in Vetter et al., it is seen that the impedance rises sharply during the first 7 days after implantation and then decreases over the following week to approximately the same level as seen immediately after device insertion [42]. Beyond this point the impedance slowly rises, reflecting the glial sheath encapsulation. This method of evaluating the immune response by impedance is useful because it allows for approximate evaluation of the glial sheath while the device is still implanted and the animal is alive. Though not as detailed as histology and susceptible to extraneous electrical confounds and noise, the impedance can be used in conjunction with histology or other endpoint analyses to describe the electrode environment over time and the resulting tissue response.

The last and most important cell type affected by the neuronal immune response are the neurons themselves. As stated above, neurons are killed by factors such as direct mechanical assault via the implant insertion, neurotoxins and reactive oxygen species released by microglia [77], and disruptions to the astrocyte homeostatic system, all contributing to a neural kill-zone immediately surrounding the implant [60, 64, 68]. This kill-zone is found only in cases of chronically implanted electrodes as stab wounds produce a negligible change in cell concentrations after a several months [78]. The size of the kill-zone varies widely between different implants,

even among sites in a single multi-shank or microwire array implant ranging in size from 10 μm to over 100 μm [43, 49, 51]. Although the neuronal deadzone represents signification neuronal loss local neural networks, particularly neuronal dendrites forming the intercellular connections, have been found disrupted more than 100 μm away from the neural kill-zone which was only 20 μm [44]. This suggests that even when a neuronal kill-zone is kept small, there is damage to the distal neural network and processing.

2.2.3 Mechanical Basis for the Chronic Immune Response

A number of theories have been proposed to explain the sources of the chronic immune response seen post-implantation of neural implants, some researchers describe the damage to vasculature as a large source for the immune response, others describe the chemical environment created by the indwelling probe, still others analyze the electrical stimulation of electrodes, but perhaps the most significant source is mechanical strain on the brain produced by electrodes. The first piece of evidence indicates that the mechanical presence of a neural implant may contribute to the chronic immune response is the time course of the immune reaction. As discussed earlier the post-implantation the CNS experiences an acute immune response to the electrode due to the damage caused the implanted electrode and the response of the microglia and astrocytes [61]. After several weeks a glial sheath forms around the neural implant and continues to isolate the electrode from the brain more and more over time [42, 66]. If the immune response was solely due to events initiated during initial implantation such as the damage to the blood-brain barrier or to neuronal cells, then the immune reaction should subside after approximately a month post surgery as was observed with stab wound injuries [59, 78]. But since the immune response does not follow this time course it is far more likely that the physical presence of the probe induces a chronic response from the brain after the initial immune response in overall multiphase response. First starting with an acute immune response due

to the damage of the initial assault during the first-week [52] This is followed by a period of increasing device performance degradation over the first month due to the formation of a glial sheath, the influx of immune cells, and disruption of local neural networks [79]. The final stage is a chronic response to the electrode where performance continually degrades due to the constant mechanical irritation to local tissue disrupting neighboring neural networks and constantly re-initializing the immune response, thus preventing healing and maintaining the glial sheath [66].

In addition to the time course of the immune response, there are strain-specific ion channels on astrocytes and microglia that when activated contribute to the immune response. The neuro-cellular mechanisms sensitive to strain were investigated after it was found that there is a constant micromotion of the brain at rest [80], of approximately 10 - 25 μm at 2 - 8 Hz, that coupled with the mechanical mismatch between electrodes and the brain, 5 kPa versus 200 GPa for the Young's modulus of the brain and electrode respectively [81–83], give rise to regions of strain local to the implant. It's been found there exists stretch-activated calcium channels on astrocytes [84] that under deformation allow for an influx of calcium (Ca^{2+}) into the cell and a release of calcium from internal stores triggering the up-regulation of endothelin-1 (ET-1) production, a vasoconstrictor which contributes to the immune response along with alterations to calcium-mediated signaling pathways disrupting normal local glial activity energy expended to restore resting voltage potential and over-activation of calcium-gated cellular mechanisms. [85]. Other research has found that interleukin-36Ra (IL-36Ra) production increases under the low strain of neural tissue, 3% to 5%, resulting in increased neuron apoptosis in spite of its anti-inflammatory properties [86, 87]. Additionally straining neuronal tissue resulted in an upregulation of matrix metalloproteinases 9 (MMP-9), which has been found to induced excitotoxicity and neural death through inflammation [88], in both strained astrocytes and microglia as well as an upregulation of MMP-2, which are correlated with wound healing [89], in strained microglia. These results indicate the role that strain plays in triggering and prolonging the neural-immune response, and given the

constant micromotion of the brain may be a substantial cause for the chronic immune response.

2.2.4 Existing Neural Implant Design Methodology

In efforts to develop an implant that can function chronically and overcome the chronic immune response, a variety of electrode designs and modifications have been tested. From the design to the material, coatings and electrical simulations parameters the electrode brain interface has been explored.

One of the earliest implemented methods for reducing the immune response and still used in conjunction with other methods is the application of drugs. are the oldest methods that have been used, but arguably have the most diverse range of interactions with the CNS. The classic method for administering drug treatments is through injection, either repeatedly through the periphery or once at the site of implantation during surgery. Some drugs aim to suppress the immune system, such as the anti-inflammatory Dexamethasone which inhibits the ability of microglia to both produce neurotoxic nitric oxide [90] and recruit astrocytes to the injury [91, 92]. Similarly, protein kinase 2 inhibitor (MK2i) inhibits pro-inflammatory cytokine TNF- and IL-8 release from monocytes further reducing the immune response [93]. The protein, -melanocyte, also suppresses the immune response by stimulating hormones which inhibit nuclear transcription factor NF-B, and reducing cytokine production from glial cells, factors are known to increase inflammatory immune response [94, 95], but like all drug treatments is limited by application through the blood-brain barrier post implantation and side effects from general application of the drug rather than local injection. Though there has been promising research examining the use of melatonin to reduce the immune response of neural implants and enhance device performance, though it's unknown if this is an effect of melatonin alone or the behavioral changes it induces, increased rest and sleep [96]. Aside from drug treatments inhibiting the immune response there other drug treatments that aim to promote neural regrowth and

healing, rather than suppressing the immune response. Most of the restorative compounds used are neurotrophins which are involved in both neural development and neural survival such as neural growth factor (NGF): a signaling protein that promotes axon growth and neuron health promoting neuron survival after CNS injuries [95,97]. For example, Neurotrophin-3 (NT-3) is a neurotrophin which promotes axon growth and serves to guide axon regeneration [98] and as a brain-derived neurotrophic factor promotes neural progenitor cell differentiation and neuron regrowth [41, 99, 100]. While all these treatments show promise in improving chronic device performance, they are limited by their application and target the symptoms of the immune response rather than the causes, still, they will likely be a key component in any viable chronically functioning electrode.

In addition to the direct application of drugs to the injury site or through the blood-brain barrier, assuming the compound is permeable, researchers have developed techniques to coat implants with directly with beneficial drugs/compounds or in impregnated polymers surrounding the solid electrode core which may improve neuronal survival or adhesion [101–103]. This method of drug administration has several advantages; first of which is the direct local release of drugs to the injury site such as [91, 104] with dexamethasone embedded polymers reducing the immune response to the same extent as a daily treatment of peripheral injections. Another advantage of drug coatings is the ability to control the release of the drug into the surrounding tissue over days or weeks. This can be a passive release of drugs that begins immediately after implantation and follows a designed release curve for drugs like peptides, polyethylene glycol [105, 106], poly (ethyl-vinyl) acetate [91], and Dextran [107]. Alternatively, drug release can be controlled via the use of electrically initiated polypyrrole reduction-oxidation (redox) reactions to release Dexamethasone to surrounding tissue [108]. But polymers themselves can also influence the neural response by controlling the adherence of different cell types to electrode surfaces as previously observed with Parylene-C coatings which inhibit the attachment of microglia [50], Poly-L-lysine promoting neuron adhesion [101], and microgel which can

reduce cellular adhesion of astrocytes, microglia, and neurons [109]. This combined with polymers such as poly 3,4-ethylene dioxythiophene (PEDOT) [110–112], polypyrrole [108, 111, 113, 114], and sol-gel [115–117] that improve the electrical performance of contact sites can help overcome some of the immune reaction by combining cell adhesion and improved electrical signaling .

Another factor of neural implants affected during chronic implantation is the quality of stimulating electrodes is the electrical stimulation applied through the electrode contact sites. Aiming to depolarize local neurons to the point of firing action potentials [44], stimulation parameters must be chosen so that the implant is able to produce action potentials in neurons without aggravating the immune response or causing damage to other brain regions. In previous studies focusing on DBS, electrodes have overcome the glial sheath simply by using high stimulating amplitudes [26]. This higher stimulation kills off local neurons and increases the size of the immune response, thus requiring stronger stimulation to reach neurons further from the implant, leading to a positive feedback loop of increasing stimulation levels killing more and more neurons and exciting additional brain regions. In Johnson et al. researchers used high amplitude stimulation, termed rejuvenation, to remove the glial sheath over the contact site and restore pre-encapsulation electrical conditions [74, 118]. Regretfully, this technique only provides transient improvement for stimulation and recording as device SNR and impedances returned to their pre-rejuvenation levels within a day; even multiple rejuvenation sessions were found to only provide the same transitory improvements. These studies show that high amplitude stimulation to achieve short term functionality results in decreased chronic function. Therefore to ensure chronic functioning electrodes safer stimulation parameters must be used. To avoid aggravating the immune system and damaging local neurons, electrical stimulation needs to follow the safe stimulation guidelines as outlined in [119–122]. In general, electric stimulation must not exceed a particular charge density and stimulation must be biphasic to prevent permanent charge injection. By following these guidelines, implant sites can be repeatedly stimulated longer without damaging local tissue, killing

local neurons, or aggravating the immune response. Improving upon these safe stimulation techniques, Koivuniemi et al. developed low power stimulation parameters and optimized waveforms to elicit high behavioral responses from animals at low stimulation amplitudes [123, 124]. These methods have not been reported to reduce the immune response, but they do not aggravate it, allowing for longer device operation. These are advantages that should be used in all implants, regardless of the immune response, but do serve to give the additional performance to devices that are suffering from the effects of the chronic immune response.

Researchers have investigated methods of bypassing the immune reaction by implementing non-penetrating or non-electrical electrodes such as electrocorticography (ECoG) implants [125–128], magnetic field stimulators [129], or recently developed optical stimulators (optrodes) [130, 131] researchers have attempted to establish a stable chronic neural interface with the brain without the use of penetrating electrical neural implants. Studies investigating these modalities have shown successes, with stimulating the brain without directly interacting with the brain tissues of the CNS and avoiding the complications that accompany a chronically implanted electrode. But these methodologies all share several drawbacks, first, they are effective at stimulating the brain, but not nearly as accurate as implanted electrical electrodes at monitoring brain activity either temporally or spatially. ECoG and MicroECoG arrays have the reverse signal problem to deal with as well as the non-linear electrical properties of the brain distorting signals making it challenging to quantify the location and strength of their signal, though recent high density recording systems have improved the spatial resolution of these devices [132].

In an effort to better treat the source of the chronic immune response rather than just treat the symptoms created by it, there has been a wealth of research exploring the design and composition of neural implants. In short, the physical design of neural implants, their shape, material, size, adhesion to the brain are believed to contribute to the brains chronic immune response and by optimizing their values the subsequent immune response can be reduced. This is due to the observed constant motion of

the brain [80] and the mismatch of material properties between the brain and most electrodes, with have a Young's modulus of 5 kPa and 200 GPa for brain and silicon electrode respectively, that result in strain produced in the brain. Due to the constant mechanical perturbations of the electrode onto the brain, it is likely that the mechanical strain produced by neural implants play a role in the chronic immune response. Focusing on this aspect of electrode design researchers have developed a variety of materials and electrode designs to reduce the strain produced and by extension the immune response. Most researchers have found that softer electrodes produce reduced immune responses [133–136], and others have observed that electrodes with smaller cross-sections produce significantly smaller immune responses [137, 138]. Following along these trends recent advances made by groups such as the Kozai Lab [45] and the Xie Lab [139] have produced extremely small and flexible electrodes that show promise as chronically stable neural implants which produce little to no immune response and perform simulations and recordings months post-implantation (Figure 2.3). In addition to establishing a stable neural interface, electrodes engineered to produce minimal strain in the brain appear to avoid eliciting the chronic immune response, avoiding the need for many of the intervention strategies discussed and creating a stable system due to the fundamental design of the device rather than interventions used to mitigate the immune response. This highlights the benefits that can be gained by further exploring this branch of neural implant design to develop electrodes optimized for chronic function.

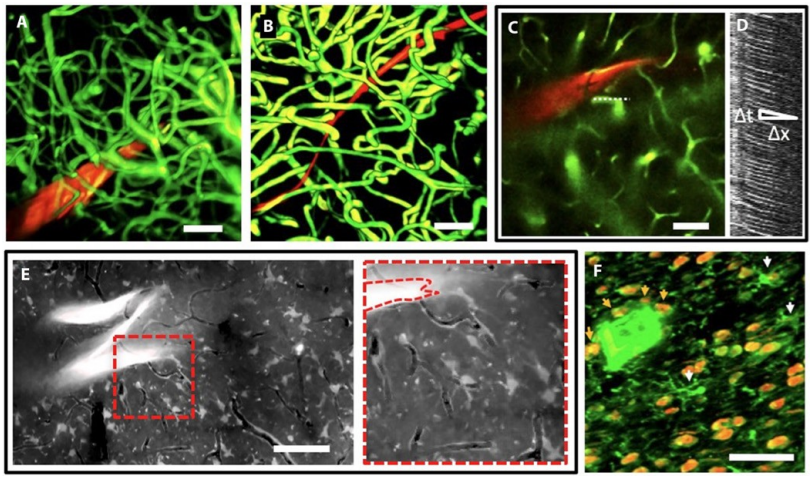

Fig. 2.3. Sample immune response observed to implantation of nanoelectronic thread (NET) neural implant developed by the Xie Lab. (A and B) Three-dimensional (3D) reconstruction of vasculatures by in vivo 2P microscopy around NET-50 (A) and NET-10 (B) probes (red) 2 months after implantation, highlighting fully recovered capillary networks (green). (E) Projection of in vivo 2-photon images at 210 to 250 μm below the brain surface at 3.5 months after implantation showing normal astrocytes and capillaries. The bright z-shaped object is a folded NET-50 probe. The capillaries are visible as dark lines. Right: Zoom-in view of the dashed area. See movie S3 for the full image stack 125 to 360 μm below the brain surface. (F) Projection of confocal micrographs of an immunochemically labeled cross-sectional slice (30 μm thick, 5 months after implantation). False-color code: orange, NeuN, labeling neuron nuclei. green, lba-1 labeling microglia. White arrows denote microglia soma. Orange arrows denote neurons in contact with the NET probe. All scale bars, 50 μm. Figure retrieved from [139]

Regrettably, a limitation of the current electrode chronically functioning designs is a clear understanding of why their designs work as well as they do and how other electrodes could be designed to achieve similar performances. This highlights one of the key inefficiencies in the current approach to neural implant design, that being the relatively under the constrained approach to devise design. Most novel implants are designed, fabricated, then tested in vivo to quantify their performance [45, 139–145]. While this approach provides absolute evidence of an electrodes performance post-

implantation it is also expensive due to fabrication costs, slow as a result of in vivo testing, and provides confounded results difficult to compare to other electrodes depending on device design. This highlights a common trend in implant design, where improvements to electrode feature are examined in a confounded manner (multiple design changes at once) when compared to a baseline, often a 15 um thick Michigan style neural implant [45] or microwire probe while having an electrode of different design and/or material. Few studies examine multiple levels for a feature and even fewer examine multiple design features at the same time [138, 146, 147]. These observations highlight the need for a more structured approach to designing neural implants so that progress made by one lab or research group can aid others rather than demonstrate a small change in design may have a marginal improvement over a baseline design. Accurate simulations have yet to be developed for the brain-machine interface and could greatly enhance electrode design answering many of the questions raised regarding optimal electrode design and describe some of the mechanisms underlying the interaction.

The value of simulations to solve this problem though is predicated on the accuracy of the simulations. As of current existing simulations have been lacking in their scope and accuracy. Is the metric of strain or stress in the brain an appropriate measure to predict the effect of electrode design on the immune response? Second, many of the properties of the simulations from boundary conditions, mesh density, and material properties are insufficient for the simulation results to be extendable to most implanted electrodes. Developing an accurate simulation model, and validating it, would solve these issues and provide researchers with a powerful tool for efficient electrode design.

3. HEAD ACCELERATION EVENT METRICS IN YOUTH SPORTS WITH HIGH CONCUSSION RATES MORE DEPENDENT ON SPORT THAN LEVEL OF PLAY

Material found in this chapter is currently under review for journal publication

3.1 Abstract

Subconcussive impacts sustained during athletic events can lead to diminished cognitive abilities, but it is unknown if subconcussive impacts sustained by athletes are dependent on the sport and level of play. A total of 16 middle school football players, 107 high school football players, and 65 high school female soccer players participated. Players were separated into levels of play based on allotted playing time during games: middle school (MS), freshman (FR), junior varsity (JV), junior varsity-varsity (JV-V), and varsity (V). xPatch sensors were used to measure peak linear and rotational accelerations (PLA, PRA) for each head acceleration event (HAE) during sessions. Data were analyzed using a custom MATLAB program to compare session metrics (median HAEs per session), season metrics (total HAEs, cumulative PLA/PRA), and regressions (cumulative PLA/PRA versus total HAEs, total HAEs versus median HAEs). Football players had a greater session ($p<.001$) and season ($p<.001$) metrics than soccer players, but soccer players had a significantly greater PRA per HAE than football players ($p<.001$). Middle school football players had a similar session and season metrics ($p<.05$) to high school levels. Sport has a greater influence on HAE characteristics than the level of play.

3.2 Introduction

Traumatic brain injuries (TBIs) result from direct head impacts and whiplash motions [148]. If not treated promptly and properly, TBI can result in diminished cognitive, motor, and sensory function, and in severe cases, permanent brain damage [149]. It was estimated that diagnosed concussions, a type of TBI, in 2010 resulted in $76.5 billion in medical costs, both direct and indirect [10]. In the United States, approximately 1.6-3.8 million TBIs occur each year due to sports-related activities [150–152]. In reality, this number is considerably higher due to documented under-reporting of symptoms [11, 153]. Traditionally among contact sports, football exhibits the highest rate of concussions, followed by women's soccer [12, 154]. There has been growing concern about the long-term effects playing football can have on a player's cognitive health [155–158]. The problem was first identified and documented in football players by Omalu et al. when a series of ex-NFL players' autopsies revealed they had a neurodegenerative disease known as chronic traumatic encephalopathy (CTE; [159–161]), previously observed only in retired pugilists [3, 162]. CTE has since been confirmed postmortem in 110 retired NFL players, as well as 48 collegiate and three high school football players [163]. The development of CTE has no correlation with history of diagnosed concussions but does correlate with a history of repetitive brain trauma, suggesting that continuous exposure to impacts that do not cause a diagnosed concussion may be the critical aspect contributing to CTE [6–9]. These findings are consistent with the results of studies by Talavage and colleagues, who determined that over the course of a season, high school football players experience impaired neurocognitive and neurophysiological capabilities without being diagnosed with a concussion or displaying any of the classic concussion symptoms [5, 150]. Specifically, they found that repetitive head trauma can cause contact sport athletes to significantly deviate from baseline measures or significantly differ from non-contact athletes [4, 5, 13, 16, 17, 150, 164–171]. It has been established that the number of impacts, as well as the location of the impact, are important factors to consider when

determining whether a player is going to experience decreased neurocognitive function by the end of a season [5, 150]. Moreover, similar results have been observed in soccer, where participation in the sport and repeated heading of a soccer ball can also produce neurological alterations [172–178]. While female soccer players traditionally have the highest rate of a concussion after football, few studies have been conducted on this group of athletes to adequately characterize how heading and other head acceleration events (HAEs) contribute to the neurological deficits [12,18,154,156,179–181]. To assess whether the injury mechanisms are similar, one must first determine how HAE distributions depend on the sport, age, or skill level. Consequently, this study was designed to examine the hypothesis that HAEs are dependent on sport/sex and level of play of the athlete. To this end, this study examined differences in HAE characteristics at different competition levels high school freshman (FR), junior varsity (JV), junior varsity-varsity (JV-V), and varsity (V) during a season of football (also including a middle school, MS) and seasons of girls soccer. Players at the high school level are assigned to a level of play based on skill level, which better reflects a players size, speed, and/or skill relative to simply age or grade.

3.3 Methods

3.3.1 Participants

All research methods involving human participants were approved by Purdue's Institutional Review Board prior to beginning the study. For participants over the age of 18, written informed participant consent was obtained. For participants under the age of 18, parental consent and participant assent were obtained. This study consists of 123 football (FB) athletes, 107 from three high schools (ages 14-18, 106 male and 1 female) and 16 from one middle school (MS; ages 12-14, all male). Data from high school girls soccer (GS) players were collected from two schools over two consecutive seasons (season 1 n=31; season 2 n=34), resulting in a total of 65 player observations (ages 14-18). A partial season occurs when a player misses three or

Table 3.1.
Number of players in each group with full seasons of data (FSD) and partial seasons of data (PSD).

Sport	Level of Play	FSD	PSD
Football	MS	16	0
Football	FR	11	0
Football	JV	28	0
Football	JV-V	8	2
Football	V	48	5
Girls' Soccer	JV	11	2
Girls' Soccer	JV-V	15	1
Girls' Soccer	V	35	1

more consecutive weeks of play (FB n=12: 1 female, 11 male; GS n=4). Within each sport, the high school athletes were divided into levels of play based on the amount of playing time received at different levels (Table 3.1). Several players saw significant playing time on both V and JV, and typically played more than those who only played at one level. Since these players cannot be solely specified as only a JV or V player, they were labeled as JV-V players and it was considered its own level of play.

3.3.2 Data Collection

Head acceleration events (HAEs) were monitored using the xPatch (X2 Biosystems; Seattle, WA). Each practice and each game was considered a separate session. Sensors were placed on FB players if the session required full pads and were used in all sessions for GS. An xPatch sensor was affixed behind a player's right ear with an adhesive patch after cleaning the area with rubbing alcohol [181, 182]. Each head impact was recorded as a separate event on the sensor when the peak linear accel-

eration (PLA) projected on any axis was greater than 10 g. Data were downloaded using the Head Impact Monitoring System software (X2 Biosystems; Seattle, WA) after sessions.

3.3.3 Data Analysis

For the purposes of this study, the clack recognition algorithm (X2 Biosystems; Seattle, WA) was not used so as to include events caused by different mechanisms (e.g. whiplashes, dives, direct impacts, and falls) [181, 182]. This study analyzed all significant head accelerations, whether they are the result of direct impacts or whiplash events, noting that the latter are no less deleterious to brain health [183–189]. Data from the sensors were processed using a custom MATLAB (MathWorks; Natick, MA) program to isolate events that occurred within the valid time window of each session and registered a PLA greater than or equal to 20 g. While the sensors collected low acceleration events (10-20 g), these were excluded from the analysis since they are typically caused by non-impact mechanisms (changing direction, kicking the ball, stopping) [181]. Data were also analyzed to remove sessions when sensors exhibited ringing or other forms of errors.

A total of 151,304 HAEs for the 123 FB players (both high school and MS) and 48,562 HAEs for the 65 GS players occurred within the valid time windows for all the sessions. Although other studies have used video systems to limit analysis to HAEs in which direct head impacts occurred, in this study, threshold and outlier analysis lead to the acceptance of 31,774 (FB; 21.0%) and 8,368 (GS; 17.2%) HAEs as valid (used to generate Figure 3.1). Of these impacts, full-season athletes accounted for 30,675 (FB) and 8,238 (GS) HAEs. Following HAE validation, data for players with full seasons were adjusted (as described in Appendix A) for times where a participant was playing without a sensor (e.g. the sensor had fallen off). Data generated to account for missing collection time is referred to as repair data and comprises 3,421 (football; 10.0%) and 176 (soccer; 2.09%) of the total accepted. This brings the total

number of HAEs for all analyses (other than in Figure 3.1) to 34,096 (FB) and 8,414 (GS).

Data were analyzed for full-season athletes on a per player basis, and the following impact metrics were established: median number of HAEs per contact session (a session where at least one HAE occurred), total number of HAEs per season, cumulative PLA per season, cumulative peak rotational acceleration (PRA) per season, number of contact sessions, and percent of contact sessions. Head acceleration events without repair data for full and partial season players were used to generate the HAE PLA magnitude histogram (Figure 3.1). Regressions for each level of play were used to determine the relationship between the following metrics: cumulative PLA per season and the total number of HAEs, cumulative PRA per season and the total number of HAEs, and the total number of HAEs and the median number of HAEs per contact session.

3.3.4 Statistical Analysis

Statistical analyses were performed using SAS 9.4 (SAS Institute; Cary, NC) to determine if the metrics were significant ($p<0.05$) as a function of the level of play. The chi-squared test was used to compare histograms. If the overall chi-squared test indicated statistical significance between the levels, then pairwise chi-squared tests with a Bonferroni correction was used to determine which levels were different. Analysis of variance (ANOVA) was used if the normality (Shapiro-Wilk) and constant variance (Brown and Forsythe) assumptions were met, and the Kruskal-Wallis (KW) test was used if they were not. If ANOVA indicated a significant difference between levels, Tukey's post hoc test was used to determine which levels were different. If the KW test was used, Dunn's post hoc test was used to compare differences between levels [190]. These methods were used to test the median number of HAEs per contact session, total HAEs per season, cumulative PLA/ PRA per season, number of contact sessions, and percent of contact sessions. Similar tests were conducted to compare

the regressions. The slope was computed for each data point and then slopes were grouped by level of play. Comparisons were performed within each sport to analyze differences between levels. High school FB levels were grouped to compare against grouped GS levels for a between-sport/sex comparison.

Outlier Analysis: Two separate outlier analysis methods were used. For each session, HAEs that occurred within a 10-second window were considered. If five or more HAEs occurred within those 10 seconds, all the readings in the time window were flagged. If the number of flagged HAEs in a session accounted for more than 50% of the impacts for that session, all the HAEs from that session were removed because this was indicative of a faulty sensor. A second analysis was also applied to sessions where more than 100 HAEs were recorded since all sessions were observed and athletes never approached this many HAEs in a single session. If a session with 100 HAEs or greater had an impact rate of one impact per minute or greater, the session was removed. If the session had more than double the number of HAEs than the session with the greatest number of HAEs less than 100, the session was removed. The sensors were power cycled before re-deploying for the next session.

Repair Data Calculation: Session type refers to the session and the players that participated (all practice, V game, FR practice, etc.). An impact rate was calculated for each player and each session type. For the player and the session type, the impact rate was calculated by dividing the total number of recorded HAEs the player sustained during session type in a season by the total participation time the player registered for the session type during a season, with being the total number of type sessions in a season.

$$ImpactRate_j^i = \frac{\sum_{k=1}^{n} HAEs_{j_k}^i}{\sum_{k=1}^{n} Time_{j_k}^i} \tag{3.1}$$

If the player did not participate in a session type, the impact rate for the players session type was set to zero. The number of repair HAEs for the session was calculated by multiplying the players impact rate for the corresponding session type by the time missed in the session. Outlier days were also replaced using the same repair equation with the missed time equal to the total time for the session.

3.3.5 Histograms

Only recorded HAEs for full and partial seasons of data were used to generate the histograms and were separated by sport and level of play. The recorded HAEs were sorted based on the PLA and were binned at 20 g intervals with a lower bound of 20 g. The percentage of HAEs in each bin was determined by dividing the number of recorded HAEs in each bin by the total number of recorded HAEs for that group.

3.3.6 Number of Hits

Only players with full seasons of data were used to calculate the median number of HAEs per contact session and total HAEs per season. The HAEs were separated by player and session. The total number of HAEs for each session was calculated adding the recorded data and any repair data needed for missing session time. If the player did not register an HAE for a session, it was considered a non-contact session and these sessions were excluded when calculating the session median number of HAEs. Regardless of session type (game or practice), the median number of HAEs per contact session was determined for each player. For the total number of HAEs, a player's recorded number of HAEs and repair data were summed to produce an accurate HAE total.

$$TotalHAEs^{i} = \sum_{j=1}^{m} \sum_{k=1}^{n} (HAEs^{i}_{j_k} + RepairData^{i}_{j_k}) \tag{3.2}$$

3.3.7 Cumulative PLA and PRA

To calculate the cumulative PLA for a season, a player's recorded HAE PLAs were summed. The repair HAEs were sorted by session type. The total number of

repair HAEs for each session type was then multiplied by the average event PLA for that specific session type.

$$RepairPLA^i = \sum_{j=1}^{m}(\sum_{k=1}^{n}(RepairData^i_{j_k}) \times AveragePLA^i_j \tag{3.3}$$

The repair HAE magnitude was added to the recorded HAE cumulative PLA. An equivalent process was conducted for PRA.

3.3.8 Contact Sessions

A contact session is a session that had at least one HAE in the session. The percent of contact sessions is the number of contact sessions divided by the total number of monitored sessions.

3.3.9 Linear Regressions

A player's cumulative PLA and PRA for the season were plotted against the total number of HAEs per season. The players were then grouped by level of play and a linear regression was performed for each group. The intercepts for these plots were fixed at the origin because it is not possible for a player to accumulate any PLA or PRA without registering an HAE in a season. Players who accumulated more than 40% of their HAEs for the season in a single session (noted by the filled-in marker) were removed from the session-season regression, but the data points were still plotted.

3.4 Results

Over the course of a season, the 95 full-season male high school FB players collectively accounted for 29,978 HAEs (15,948 practice; 14,030 game) and the 16 MS players collectively accounted for 4,118 HAEs (2,702 practice; 1,416 game). The number of HAEs in a season for a single FB player ranged from 23 to 1,352. Of the

29,978 HAEs, V, JV-V, JV, and FR players accounted for 17,704 (9,516 practice; 8,188 game), 3,100 (1,570 practice; 1,530 game), 6,437 (3,438 practice; 2,999 game), and 2,737 (1,424 practice; 1,313 game) HAEs, respectively.

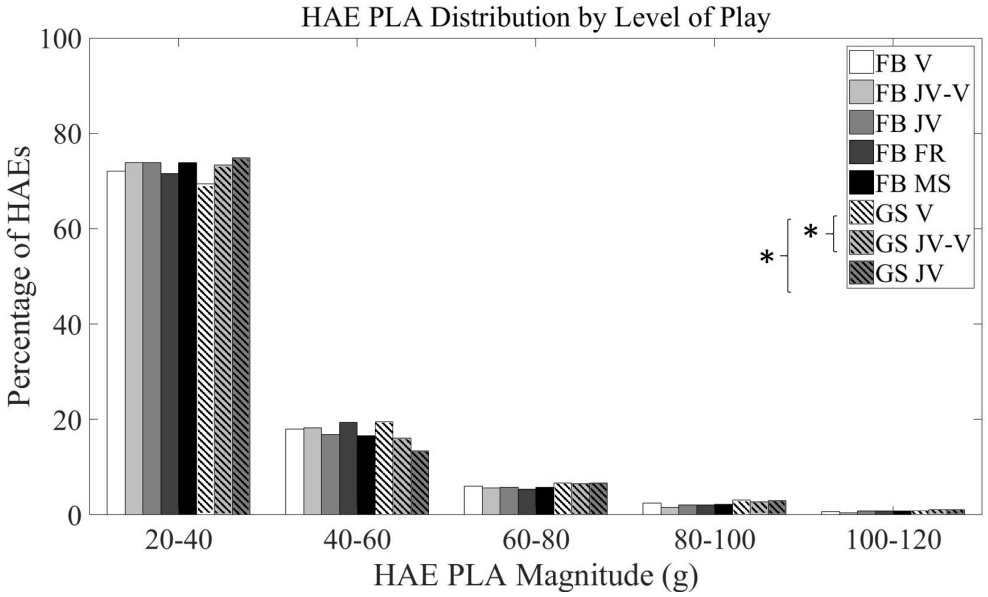

Fig. 3.1. Normalized distribution of HAE PLA magnitudes by level of play. There was no statistical difference between FB levels of play (p=.170), and GS V differed from both GS JV (p=.001) and GS JV-V (.006) distributions. High school FB and GS distributions were significantly different from each other (p=.001). Less than 1% of HAEs occurred above 120 g for each level.

The 61 full-season GS players sustained 8,414 HAEs (5,192 practice; 3,222 game) with V players accounting for 4,991 HAEs (2,925 practice; 2,066 game), JV-V taking 2,502 of the HAEs (1,662 practice; 840 game), and JV players accounting for 921 HAEs (605 practice; 316 game). The number of HAEs in a season for a single GS player ranged from 22 to 411. The HAE PLA magnitude distribution was examined for each sport and level of play. For FB, there was no significant difference between the levels (p=.190). For GS, V was significantly different JV (p=.001) and JV-V (p=.006). There was a significant difference between the high school FB distribution and the GS distribution (p=.001; Figure 3.1). There was a statistical difference

Table 3.2.
Sport and level of play medians of total HAEs, cumulative PLA, and cumulative PRA per season with the statistical difference noted in the column to the right of the metric of interest.

Group	n	Total Number of HAEs†	SG‡	Cumulative PLA($\times 10^3$g)†	SG‡	Cumulative PRA($\times 10^5 \frac{rad}{sec^2}$)†	SG‡
FB MS	16	230 (140, 321)	A	7.42 (4.90, 11.8)	A	13.7 (7.94, 19.6)	A
FB FR	11	198 (141.5, 334.25)	A	7.89 (5.31, 11.8)	A	12.7 (8.17, 19.5)	A
FB JV	31	236 (161.5, 327.75)	A	8.54 (5.53, 10.7)	A	15.0 (8.32, 18.4)	A
FB JV-V	4	412.5 (214, 653)	A	13.5 (7.59, 22.5)	A	21.7 (12.1, 40.6)	A
FB V	50	295.5 (150, 516)	A	11.3 (5.47, 19.2)	A	18.9 (7.19, 33.8)	A
S JV	12	64.5 (52.5, 99)	D	2.32 (1.94, 3.95)	D	4.27 (3.41, 7.10)	D
S JV-V	15	188 (80.25, 248)	E	7.59 (2.93, 8.18)	E	11.6 (6.20, 16.2)	E
S V	35	104 (74.5, 201.5)	D,E	4.24 (2.63, 7.28)	D,E	7.64 (5.11, 13.8)	D,E

† Each cell contains the median (1st quartile, 3rd quartile) for the metric.

‡ Significance grouping (SG) rows with the same letter denote levels within the sport that are not significantly different (p>0.05). A-C denote differences for football and D-E denote different levels in soccer.

between the median number of HAEs per contact session between the MS and JV levels for FB (p= .018; KW; Table 3.2), but no statistical difference between the levels of play for GS (p= .675; KW; Table 3.2). However, there was a statistical difference in the median number of HAEs per contact session based on sport (p<.001; KW), with GS recording fewer HAEs per contact session than high school FB, regardless of the level of play.

There was no difference between the levels of play for total HAEs (p=.133; KW), cumulative PLA (p=.104; KW), or cumulative PRA (p=.193; KW) for FB (Table 3.2). For GS, the JV-V level exhibited significantly greater total HAEs (p=.041; KW) and cumulative PRA (p=.031; KW) than the JV level (Table 3.2). High school FB players

Table 3.3.
Number of players in each group with full seasons of data (FSD) and partial seasons of data (PSD).

Group	Average (standard deviation) Number of CS	SG‡	Average (standard deviation) Percent of Sessions Involving Contact	SG‡
FB MS	26.8 (2.67)	A	87.6 (6.88)	A
FB FR	27.5 (6.76)	A,B	75.9 (17.6)	A,B
FB JV	37.0 (9.38)	C,D	75.0 (16.3)	B
FB JV-V	45.4 (6.63)	C	87.1 (8.43)	A,B
FB V	34.2 (8.15)	B,D	77.4 (15.0)	A,B
GS JV	21.2 (6.06)	E	47.4 (13.4)	E
GS JV-V	36.1 (11.0)	F	62.7 (17.9)	E
GS V	32.8 (10.2)	F	56.5 (15.7)	E

‡ Significance grouping (SG) rows with the same letter denote levels within the sport that are not significantly different (p>0.05). A-D denote differences for football and E-F denote different levels in soccer.

registered significantly greater season totals for number of HAEs (median: 262), cumulative PLA (median: 10.0103 g), and cumulative PRA (median: 16.8105 rad/s2) than GS players (respective medians: 107, 4.05103 g, 7.55105 rad/s2; p<0.001; KW).

The number of contact sessions in a season were compared for each of the different levels in each sport (Table 3.3). For FB, MS had fewer total contact sessions than JV (p<.001; KW), JV-V (p<.001; KW), and V (p=.009; KW), FR had less than JV (p=.019; KW) and JV-V (p<.001; KW), and JV-V had more than V (p=.033; KW). When the number of contact sessions was normalized by the total number of sessions in a season, there was only a significant difference between MS and JV, with MS having a higher percentage of contact sessions in a season (p=.032; KW). For GS, JV differed from JV-V and V in the number of contact sessions (p=.001 and

p=.003, respectively; ANOVA), but no levels differed regarding percent of contact sessions (p=.062; ANOVA). High school FB had statistically more contact sessions in a season (35.2; p=.039, KW) and a higher percentage of contact sessions (77.4%; p<.001, KW) than GS (31.5 and 56.4%, respectively).

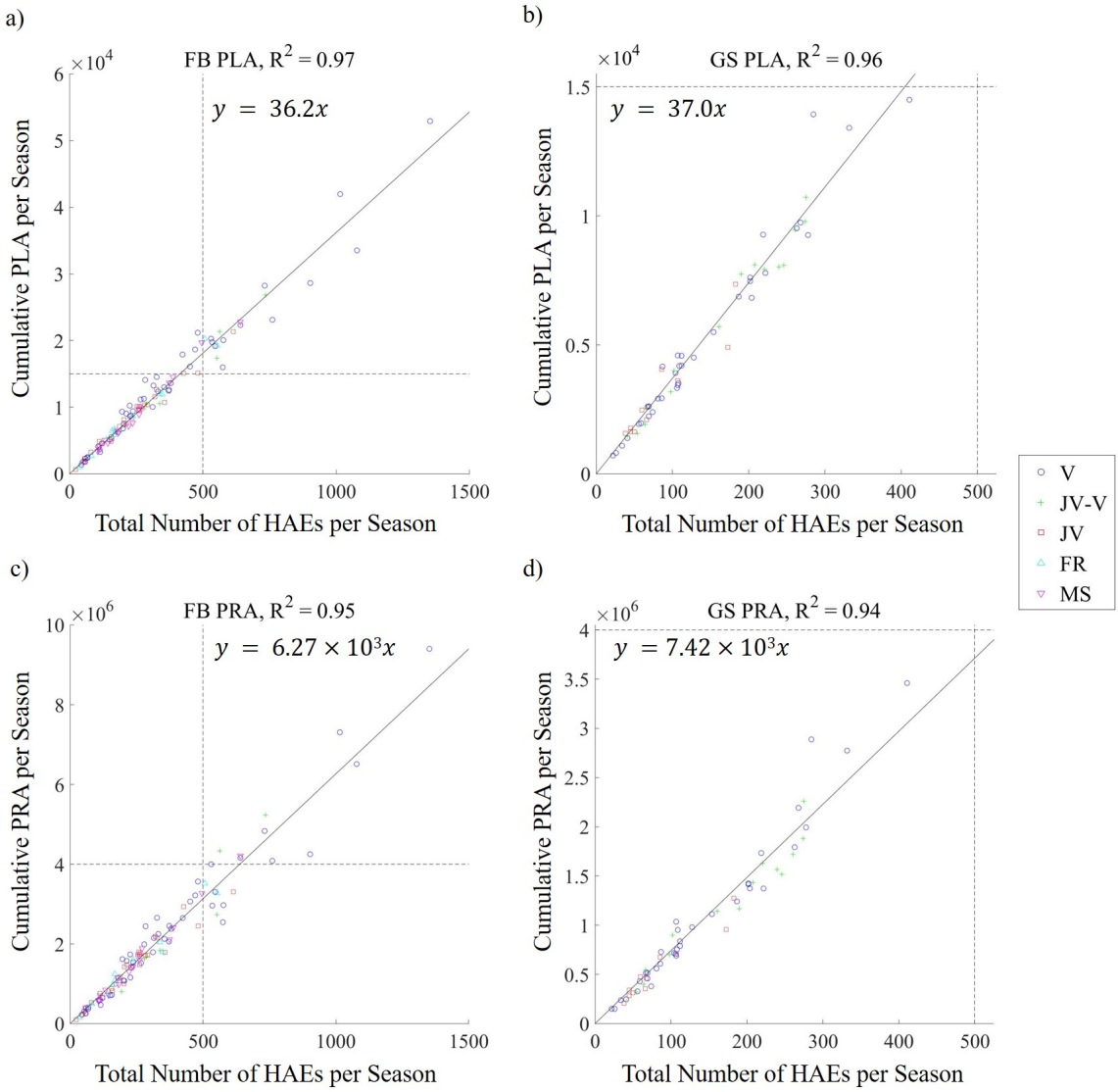

Fig. 3.2. Cumulative PLA (g) for the season versus the total number of HAEs per player per season for (a) FB and (b) GS, and cumulative PRA (radsec^{-2}) for the season versus the total number of HAEs per player per season for (c) FB and (d) GS. For cumulative PLA, there was no statistical difference across of the levels of play in terms of the slope (FB: p=.340, ANOVA; GS: p=.572; ANOVA), or between high school FB and GS (p=.702; KW). For cumulative PRA, there was no statistical difference between any of the slopes among the different levels of play (FB: p=.881, ANOVA; GS: p=.146, ANOVA). There was a significant difference between PRA regressions between high school FB and GS (p<.001, ANOVA). To demonstrate the difference in scale, the dashed lines in (a) are the same as in (b), and the dashed lines in (c) are the same as in (d).

There was no statistical difference between any of the regression lines for the different levels of play (Figure 3.2a,b) when examining the cumulative PLA for a season versus the total number of HAEs in a season for FB (p=.367; ANOVA) or GS (p=.615; KW), nor was there a difference between high school FB and GS (p=.702; KW). When the levels are combined for each sport, the total number of HAEs in a season is a good predictor (FB R2 = 0.97; GS R2 = 0.96) for the cumulative PLA. Similarly, for PRA, there was not a statistical difference between any of the levels of play in terms of the regression lines for either sport (FB p=.933, KW; GS p=.146, ANOVA; Figure 3.2c,d). The slope of the regression line for GS is significantly steeper than the one for high school FB (p<.001; ANOVA).

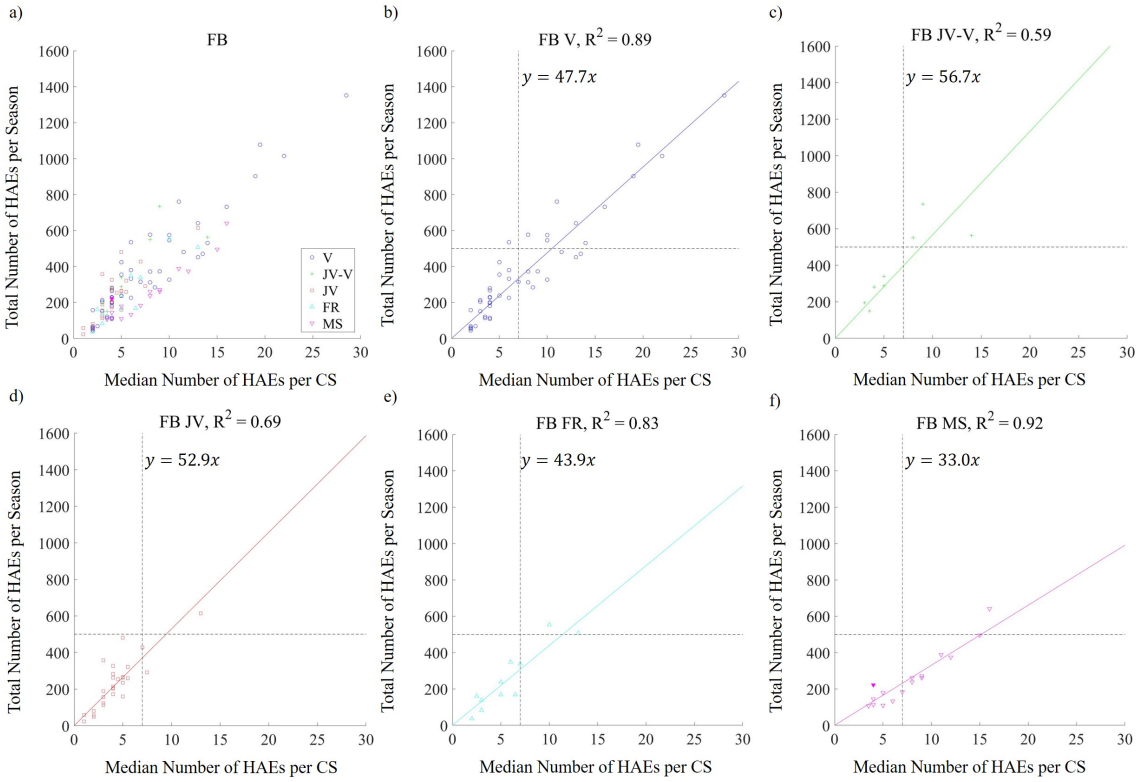

Fig. 3.3. Total number of HAEs per season per FB player versus the median number of HAEs per contact session (CS). The plots have the players grouped by level of play as follows: (a) all players (b) V (c) JV-V (d) JV (e) FR (f) MS. The dashed lines on these plots are the same as those used in Fig. 4 to demonstrate the differences in scale. There is a significant difference in the slopes between V and MS (p=.001; KW), JV-V and MS (p=.003; KW), and JV and MS (p<.001; KW). The filled data point in (a) and (f) indicates a player who accumulated 40% or more of the HAEs for the season in a single session and was not included in the regression analysis.

In comparing the median number of HAEs in a session to the total number of HAEs sustained during an entire FB season, some slopes differed between levels (Figure 3.3). Middle school was different from JV (p<.001; KW), JV-V (p<.001; KW) and V (p=.001; KW) levels. The JV-V players played in both JV and V events, so they participated in the greatest number of contact sessions (45.4 6.63) and this level has the steepest slope (Figure 3.3c). For GS, JV compared to JV-V and V

had significantly different regressions for the total HAEs in a season versus median HAEs in a session (p=.014 and p=.048, respectively; ANOVA; Figure 3.4). Similar to FB, the JV-V level in GS exhibited the steepest slope (Figure 3.4c) as this level participated in the greatest number of contact events (36.1 11.0).

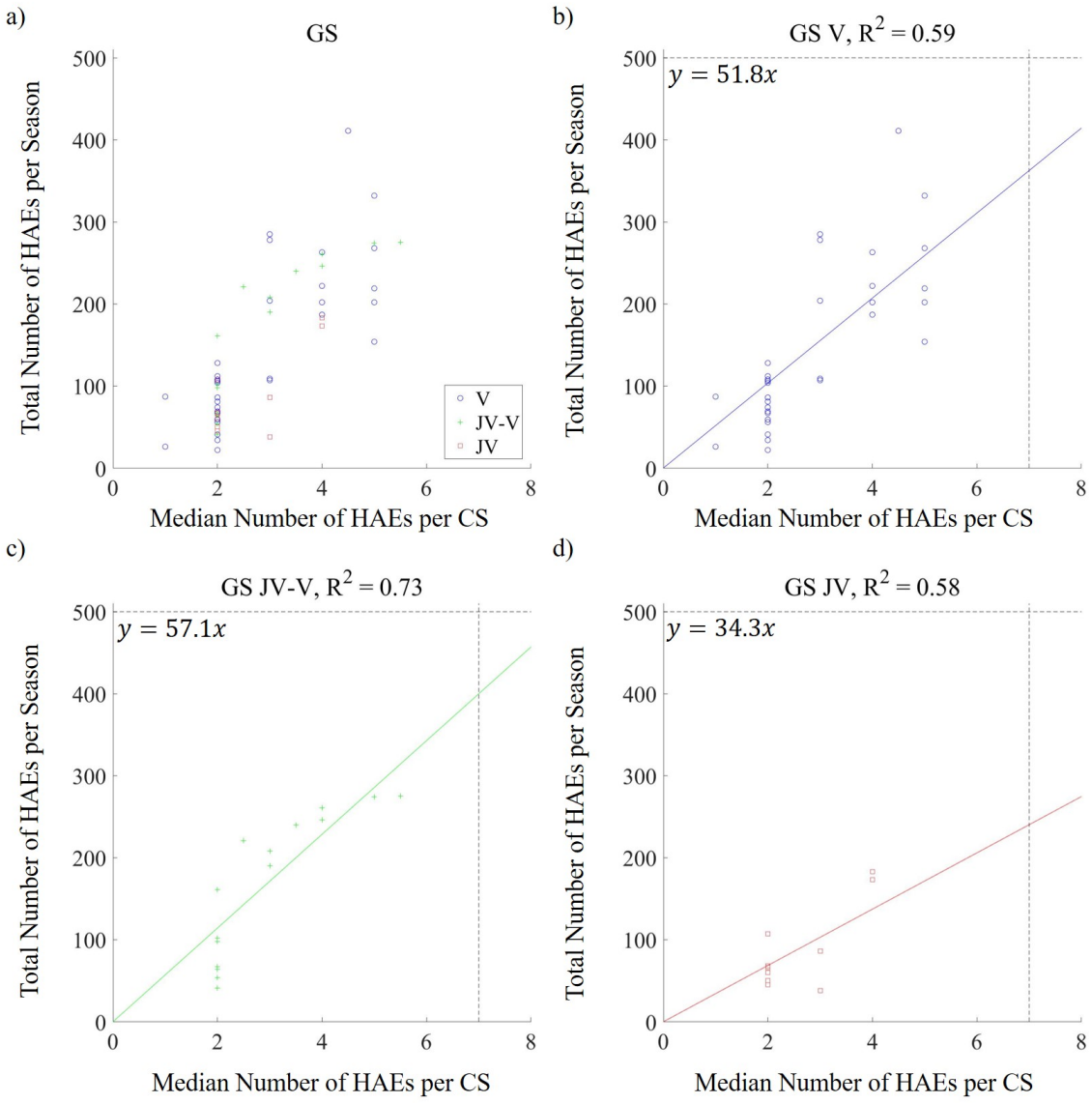

Fig. 3.4. Total number of HAEs per season per GS player versus the median number of HAEs per contact session (CS). The plots have the players grouped by level as follows: (a) all players (b) V (c) JV-V (d) JV. The dashed lines on the plots are the same as the lines shown in Fig. 3 to demonstrate the differences in scale. There was a statistical difference between JV and JV-V (p=.014; ANOVA) and JV and V (p=.048; ANOVA).

3.5 Discussion

The purpose of this study was to determine whether HAE metrics are dependent on the level of play and/or sport/sex. Since FB and GS players usually exhibit the highest rates of diagnosed concussions, characterizing all HAEs is an important step in understanding how the HAE characteristics contribute to TBI in athletes [12,154,156]. While differences observed between sports could reflect contributions from both sport and sex, the findings regarding the level of play within a given sport have important implications for potential interventions. The hypothesis that HAE characteristics are dependent upon sport was found false for certain metrics. Although football and soccer are vastly different in terms of rules, gameplay, and equipment, high school FB and GS players exhibit similar PLA characteristics for individual HAEs (Figure 3.2a,b). Since this is the only aspect in which these two groups of athletes are similar, the player average PLA per HAE may be an important factor contributing to the high rates of concussion experienced in both groups. The mechanisms by which HAEs arise differ in football and soccer, but a more thorough analysis of the biomechanics of the head and neck during these HAEs may lead to a better understanding of the factors responsible for the player average PLA per HAE to be similar between the two sports. Differences in the way FB and GS players acquire HAEs result in differences for certain HAE metrics. In football, contact with another player, either through blocking or tackling, is a fundamental component of the game and is almost guaranteed to happen once per play for multiple players. Even though heading is an important aspect of the game of soccer, it generally occurs less frequently than contact in football. This increased frequency is what leads to higher season totals (total number of HAEs, cumulative PLA/PRA) for FB players and the possibility of greater neurological alterations (Table 3.2). Interestingly, the observation that GS players have a higher player average PRA per HAE than high school FB players (Figure 3.2c,d) suggests that HAEs from heading a ball in soccer, how a majority of HAEs in soccer occur, are fundamentally different in mechanics than HAEs from

the tackling experienced in football. It has been observed in the literature that total HAEs, cumulative PLA, and cumulative PRA can represent the mechanical load on the brain and is indicated that cumulative exposure is important when determining whether neurological changes occur [5, 7, 15, 16, 18, 150, 164, 179, 181, 191, 192]. The cumulative PLA and PRA correlate strongly with the total HAEs (R20.94), making total HAEs an accurate measure for predicting cumulative PLA and PRA for a season and only necessitate tracking the number of HAEs with a PLA over the threshold instead of having to record the PLA and PRA for each individual HAE. Therefore, a players HAEs per contact session can serve as a fluid metric to predict total HAEs (and by extension cumulative PLA and PRA), such that monitoring HAEs on a session basis could allow for adjustment of a players technique or participation in contact sessions during a season to proactively limit cumulative exposure. This relationship is valid for FB (0.68R20.92), as long as the level of play is known, but is not as reliable for GS (0.58R20.73). This trend appears to reflect the difference in how FB and GS players accumulate HAEs.

Girls soccer demonstrated differences between levels of play among different HAE metrics. Junior varsity players may be at less risk of experiencing neurological changes than JV-V or V players. Players at the JV level, due to their lower skill level relative to JV-V and V players, are less likely to utilize headers to control the ball as noted by observations during data collection and trends reported by McCuen et al., resulting in substantially, but not always significantly, lower season totals (total number of HAEs, cumulative PLA/PRA), number of contact sessions, and percent of contact sessions [181]. Reducing the number of heading sessions in a season would help to reduce the season totals for the JV-V and V players.

Relative to GS, FB was internally more consistent between levels of play for HAE metrics. Examining FB levels indicates MS players may be at the same or greater risk of developing neurological deficits compared to high school players. Even though MS players have a shorter season than the high school players, they still accumulated comparable season totals. Middle school teams typically have fewer players than high

school teams, requiring players to play both offense and defense and likely leading to a greater accumulation of HAEs. This is especially concerning since it has been observed that the age at which a brain injury occurs can be a factor for the type and severity of short-term neurological problems and ones that develop later in life, with younger participants possibly developing more serious complications [8, 9, 193–197]. Teaching proper tackling technique to players should reduce the PLA and PRA for individual HAEs, overall HAE accumulation, and provide better protection from long-term consequences. While increased playing time can explain the similarities between HAE totals for MS and high school FB players, the lack of significant difference between their individual HAE magnitudes may be due to physical differences, primarily neck strength, between the groups [198]. It has been hypothesized that players under the age of 14 should not play tackle football because they are exposed to greater risk relative to older, more physically developed players who possess greater neck strength to better protect and brace themselves for tackles [199]. While MS players are physically smaller and unlikely to generate the same forces as high school players while tackling, their HAE data were comparable to the high school players, suggesting other biomechanical factors contribute to HAE characteristics. More MS teams should also be studied to determine if the trends extend to schools in different leagues.

Another FB player level of interest found in this study is the JV-V level and the increased risk these players are at for asymptomatic neurological changes. These players participated in the greatest number of contact sessions per season (Table 3.3) and although not statistically significant, these players also had higher HAE season totals than other levels. The most concerning metric from the JV-V level was that they had the steepest slope ($y = 73.1x$) for correlating the season HAEs to the session HAEs (Figure 3.3c). These players are essentially playing on two teams and participate in more contact sessions than a player that is only active on a single level. Just like the MS players, the JV-V players are at a greater risk of overexposure due to increased playing time. Previously, neuroimaging (primarily magnetic resonance imaging) has been used to quantify and monitor chemical,

structural, and hemodynamic neurological changes in contact sport athletes due to repetitive HAEs [5, 15–18, 150, 166, 167, 179, 191, 200–203]. Such investigations have strongly suggested an increased risk of neurological changes for overexposed players. If it is known a player is going to be playing in two games during a certain week, coaches and athletic trainers may consider making a practice session a non-contact session for the player to reduce the total number of HAEs the player will sustain that week. To confirm that the results of this study are applicable to high school FB players in general, the teams in this study were compared to other teams analyzed in similar studies (Table 3.4) [5, 44, 150, 191, 204–206]. This comparison demonstrates the MS team is experiencing HAEs similar to high school teams in general. If teams are registering more HAEs than the teams examined here at the comparable level of play, it can be inferred those teams will experience increased asymptomatic changes in neurological function [5, 150]. This also provides evidence that sensors and data analysis in this study are consistent with other sensor systems.

Table 3.4.
Comparison of the teams in this study to similar data that has been collected by others. All values below are calculated or estimated means.

Study		Number of HAEs per Session[†]	HAE PLA in g's[†]	Number of HAEs per Season[†]	Cumulative PLA per Season in g's[†]
Broglio et al. 2009, Eckner et al. 2011, Broglio et al. 2012		16 (8)	25.5 (35.6)	549 (284)	14,009.1 (10,102.5)
Schnebel et al. 2007		22 (10)	24.6 (37.8)	520 (250)	12,822.0 (9,439.6)
Breedlove et al. 2012, Breedlove et al. 2014, Talavage et al. 2014		15 (8)	27.5 (38.8)	672 (365)	18,494.8 (14,163.1)
Current Study	FB MS	(8)	(35.9)	(257)	(9,227.4)
	FB FR	(7)	(36.5)	(249)	(9,089.8)
	FB JV	(5)	(35.4)	(237)	(8,396.8)
	FB JV-V	(8)	(34.6)	(429)	(14,851.3)
	FB V	(8)	(37.0)	(371)	(13,715.7)
	High School FB	(7)	(36.4)	(316)	(11,492.2)
	GS JV	(2)	(36.6)	(84)	(3,065.7)
	GS JV-V	(3)	(36.1)	(167)	(6,014.9)
	GS V	(2)	(37.2)	(143)	(5,304.5)
	High School GS	(2)	(36.8)	(138)	(5,075.5)

[‡] Data in cell are from the publication and the number in parenthesis is estimated when HAEs with a PLA below 20 g are removed to allow for a more accurate comparison with the data from this study.

Use of the xPatch to monitor HAEs is a limitation of the study since it has been shown that this sensor typically exhibits errors on the order of 20%, but this accuracy is sufficient for comparing distributions and cumulative exposures [182]. The objective of this study, however, was not to determine the HAEs that would induce a brain injury but to measure all HAEs sustained. Another limitation of this study is the inability to determine if the difference between FB and GS is due to sport or sex since they are confounding factors. Collecting HAE data on boys soccer will help to distinguish how sport and sex individually contribute to the differences. Players were also only designated by level of play, and although football HAE characteristics are

also dependent upon position, some players in this study played multiple positions and would not have allowed for analysis by position [4, 5, 11, 44, 206–209].

3.6 Conclusion

This study was designed to examine the differences in HAE characteristics between different sports/sex (GS and FB) and levels of play to obtain a better understanding for how repetitive head traumas contribute to neurological deficits. The differences in rules and gameplay readily account for FB players accumulating more HAEs than GS players, but the mechanisms by which the HAEs occur in the two groups of athletes likely explain the differences in player average PRA per HAE for each group. Sport and sex are confounding factors in this study that are both likely to significantly contribute to the HAE metrics. Analyzing the HAEs by the level of play within each sport has revealed some concerning trends. For GS, JV-V players tend to have greater HAE metrics than JV players, presumably due to the relative difference in skill level and increased playing time. Therefore, these players are potentially at greater risk for developing neurological changes. For FB, the younger players at the MS level have the potential for developing more severe neurological alterations since they exhibit similar HAE characteristics to high school players but are not as developed, physically or neurologically. Reducing the number of HAEs athletes sustain during the season, be that by implementing additional rules and regulations or continuing to improve technique, will help ensure and protect the neurological health of contact sport athletes.

4. AUTOMATED HEAD SEGMENTATION AND QUANTIFICATION

Material found in this chapter will appear in a journal publication

4.1 Abstract

4.2 Introduction

In contact sports, concussion, a type of mild traumatic brain injury (TBI), is of great concern for athletes short- and long-term neurological health [6,13,165,193,210–215]. There are approximately 1.8-3.6 million diagnosed TBIs due to sports-related activities every year in the United States [151]. The actual number of concussions is most likely higher due to the dramatic under-reporting of symptoms [11, 153]. More than 4 million athletes ages 6-12 [13] and 2 million high school athletes [14] participate in contact sports (football, soccer, lacrosse, wrestling, ice hockey) in the United States.

Previous studies have used sensor systems to characterize the head accelerations of contact sport athletes to better understand how head accelerations may lead to concussions and asymptomatic neurological changes [15–19, 150, 166, 167, 179, 181, 191, 200, 202, 216, 217]. Most of the current sensor systems report the peak linear and angular accelerations (PLA and PRA) of the heads center of mass (CoM) as these have been known to correlate with the mechanical load sustained by the brain [5,14,18,19,150,179,181,192,205–207,209,218,219]. However, laboratory testing has indicated that many of these systems have errors associated with individual head impact measurements [182,220].

Current sensor systems utilize sensors that are placed on the head (i.e. behind the ear, in the helmet, in the mouth, etc.) to measure the linear acceleration at the sensor location and the angular acceleration of the head. While this provides a measure of the head at the location of the sensor, the measurement of interest is the acceleration at the center of mass (CoM) of the head because it can be used to estimate the energy transmitted to the brain [164, 221]. The acceleration at the CoM can be calculated using rigid body kinematics.

$$\mathbf{a}_{CoM} = \mathbf{a}_{sensor} + \boldsymbol{\alpha} \times \mathbf{r}_{sensor->CoM} + \boldsymbol{\omega} \times \boldsymbol{\omega} \times \mathbf{r}_{sensor->CoM} \tag{4.1}$$

The linear acceleration at the sensor location ($\mathbf{a}_{sensor}$), angular acceleration ($\boldsymbol{\alpha}$), and angular velocity ($\boldsymbol{\omega}$) are all measured using the sensor, but the vector from the sensor to the ($\mathbf{r}_{sensor->CoM}$) may vary from player to player.

Many sensor systems have algorithms that transform the acceleration at the sensor location to the acceleration at the CoM of the head. This means these systems do not account for the individual center of mass vector of each athlete in the calculation, which may cause the reported acceleration at the CoM to be different from the true acceleration experienced. The ability to accurately measure the acceleration at the CoM is necessary to correctly estimate the forces on the brain and correlate the neurological changes with the head acceleration events (HAEs). Without accurate acceleration values, the design criteria for protective equipment and recommendations for player safety may be unreliable.

There is a need to determine the location of the CoM relative to different sensor locations for accurate acceleration measurements. A novel automated head segmentation program was developed to take T1 magnetic resonance images (MRIs) and segment the various tissue types of the head. In this paper the authors present a system designed to function autonomously, allowing for batch processing without the need for user input. The system is also capable of analyzing partial MRI scans and is able to construct an accurate estimation of the scanned and unscanned regions of the head segmenting the brain, cerebral spinal fluid (CSF), skull, and skin-muscle. This study examines the different head metrics between high school male football athletes

and female soccer athletes and the variability within each group. Various head metrics such as head circumference, length, width, height, and location of the CoM will also be calculated from the model. Each individual model is then used to calculate subject specific PLA measures for the same given set of test impacts. The variability in the different PLA measures can be attributed to the different radii generated from each player's MRI scan.

4.3 Methods

4.3.1 Subjects

Purdues Institutional Review Board approved all research methods involving human subjects prior to the beginning of the study. Written informed consent was obtained from the subject if over the age of 18 and written informed parental consent and subject assent were obtained if the subject was under the age of 18. A total of 113 male football athlete-observations over three seasons and 31 female soccer athlete-observations over two seasons were recorded.

4.3.2 MRI Head Scans

At the beginning of each football and soccer season, each player enrolled in the study underwent a T1 scan of his or her head as described in Bari et al. [18]. In brief, a 3T General Electric Signa HDx magnetic resonance scanner (Waukesha, WI) with a 16-channel brain array was used to perform a high-resolution T1-weighted anatomical MR scan using 3D spoiled gradient recalled echo (SPGR) sequence 9TV/TE = 5.7/1.976 ms, flip angle = 73 degrees, 1 mm isotropic resolution.

4.3.3 Head Segmentation

To quantify the head geometry for each player, the MRI scans from each player were segmented using a custom program developed in Matlab (Mathworks; Natic,

Massachusetts). The aim of this program is to perform autonomous segmentation of an entire or partial noise confounded T1 head scan identifying the brain tissue, white matter, grey matter, skull, CSF, and skin-muscle of the head. To quantify partial datasets where portions of the head scan are missing or lost due to signal drop off this program utilizes image correction, adaptive intensity thresholding, and fits a deformable skull model to achieve tissue segmentation.

The first step in the segmentation program after loading the source image stack is to normalize the intensity range of the image stack between 0 to 255 to permit standard processing across any intensity range (data is stored in an 8-byte variable type to maintain intensity resolution). This is followed by orienting the image stack so the head is facing in the same orientation as the model skull.

To compensate for inconsistencies in the original scans that may exist due to non-homogeneous noise in the image (ie. regions of bright or dark bias due to scanning defects or a loss of signal intensity as the scanned points become more distal to the scanning coils) the image stack undergoes intensity correction. To correct for regional intensity biases the T1 scan stack is processed with a local entropy minimization algorithm via a bicubic spline model as implemented via the intensity inhomogeneity correction tool developed by Salado et al. [222]. This is performed in all three dimensions to correct intensities throughout the volume of the scan rather than along one plane of the scan. This is followed by an anisotropic diffusion filter as implemented by Perona et al. [223] to remove salt & pepper noise and further enhance the image and in particular the edge contrasts used in segmentation. Finally, the contrast of the image is enhanced via Matlabs inbuilt adapthisteq function to further differentiate between different tissue in the head.

After intensity correction and noise removal, the head is segmented from the background via intensity thresholding and Chan-Vese model for level step contour fitting [224]. An intensity threshold of 4% was observed to provide a clear of the delineation for between the background and the head, though depending on source image stack intensity this value can be adjusted manually or the maximal background

intensity outside the head (averaged maximum taken from the 6 corner volumes of the scan space) can be used as the segmenting threshold. After initial thresholding, the largest masked region is identified as seed values for the head and other masked regions are discarded (i.e. false signals from the scan bed, padding, etc). The seed voxels are then used as the starting points for level step contour fitting which identifies the boundary between the head and background and establishes a mask for the entire head. An example of this processing stage is shown in Figure 4.1.

One of the requirements for this head segmentation system that innovates over existing head segmentation software its ability to process partial head data and develop a predictive fitted model. As a limitation of large population studies the player MRI scans obtained for this study are only partial head scans, focusing on the brain at the expense of contrast and signal intensity elsewhere in the scan volume. This results in a scan that either has little to no signal below the hard palate of the mouth or is not within the scanned volume. To remedy this an existing model of the skull is fitted to the partial data extracted from the

Direct extraction and analysis were attempted on these datasets, but due to the variation between player scans and the lack of high contrast data throughout the head an automated segmentation could not be performed. Hence the skull fitting performed in this program is required to quantify the whole head geometry.

Following head isolation, an initial raw skull is segmented from the head to use as a baseline for matching the deformable skull model to the initial skull segmentation. This segmentation begins by identifying high-intensity seed voxels for the brain and the non-brain regions of the head; respectively, voxels at least 3 cm internal from the surface of the head and within the upper 5 cm of the head are considered brain seed voxels and the exterior 2 mm of the head are non-brain seed voxels. These seed regions are starting points from where voxel maps of the brain and non-brain region are defined. The seed regions are expanded by sweeping a detection threshold for voxels in the image stack from high intensity to low. For each voxel above the threshold, a check is performed to check if the voxel is in contact with the brain

region or non-brain region voxels. When a voxel is in contact with one region and not the other, it is assigned to the tissue type of the contact region. When a voxel is in contact with both regions the voxel is assigned to the region with which it has more neighboring voxels. At locations with an equal number of neighbors with both regions, the voxel is assigned to the brain region. Alternatively, if neither region is in contact with the voxel, it was left unassigned and valid for future assignment. This analysis is performed for each voxel at a given intensity level until no voxels could be assigned. After sweeping the voxel intensity threshold from 100% to 25% of maximum and analyzing at each level a rough segmentation between the brain and skull is obtained. The raw skull segmentation is obtained by intensity thresholding the non-brain region within the head and selecting voxels below the mean intensity of voxels in the non-brain region of the head. An example of this processing stage is shown in Figure 2.B.

With a raw skull segmentation to use as a baseline, a principle component defined skull model can be fit to the image stack using techniques similar to those developed in Luthi et al. and a skull developed via principle component (PC) analysis [225]. In brief, skull fitting is performed by adjusting the scaling factors for each PCs which describes a model of the skull model, the model using in this study is comprised of 44 components, to maximize the overlapping regions between the raw skull segmentation and the deformable model while minimizing the non-overlapping regions. For the model skull fitting PCs were processed in order of those most sensitive to least sensitive in changing the volume in the skull model. This ordering was calculated by performing a Cotters sensitivity analysis on the PCs and ranking their sensitivity scores. The model is fitted 4 stages including model size scaling, initial PC sweep, PC binary search, and PC binary search with alignment. The processing performed at each stage to fit the model skull is described in Table 4.3.3. Between each stage, the skull model was realigned to the raw skull to maximize overlap between the raw and model skulls.

Skull Fitting	
Stage Title	Description
Model size scaling	In this initial stage of fitting the model the overall size of the model skull is matched to that of the raw skull. This is performed first by measuring with length and width for each transverse slice in the upper 15 cm both skulls and calculating the mismatch in size between the two summed across all slices. The scaling factor for the model skull is then swept from 0.5 to 2 and the optimal sizing factor is selected to minimizes mismatch between the model skull and the initial skull segmentation.
Initial PC sweep	In this stage a sweep of the scaling factors for the first 14 principle components is performed to improve skull size matching. Similar to fitting stage 1, optimal PC scaling factors were selected that minimized size mismatch between the model skull and initial skull segmentation.
PC binary search	In this stage all the PC scaling factors are examined, each optimized using a uniform binary search to find scaling factors that maximize the overlap of the skull model and the raw skull while minimizing the regions that do not overlap. $$matching = \Sigma(raw_skull \cap model_skull)/\Sigma(raw_skull \cup model_skull) \quad (4.2)$$ The uniform binary search is performed three times for each scaling factor before proceeding to the next PC scaling factor. Once all scaling factors have been examined, they are examined again in a second pass as this allows changes from each PC to effect matching of every other PC.
PC binary search with alignment	This final stage performs the same uniform binary search as in stage 3, but for each overlap analysis, the alignment between the model and raw skull is updated. At the end of the 4th stage, the deformed skull model is considered the skull for the image stack.

Once the principle component defined skull model is fitted to the initially segmented skull, the skull model is used to segment the head tissues into a skin-muscle region external to the skull and the brain internal to the skull. This segmentation is performed by applying three-dimensional closing operation on the skull to isolate the neurocranium and remove holes through the skull due to the foramen magnum, jugular foramen, orbital fissures, and optic canal. Voxel masks of the regions interior and exterior to the skull are then used to segment the tissue into the skull, skin/muscle, and neurocranium regions. Once isolated, the skin-muscle tissue region is considered a uniform tissue even though it contains several tissue types including skin, muscle, cartilage, eyes, vasculature, and adipose tissue. This was done to keep the segmentation of the head simplified for geometrically simple models for finite element analysis and to reduce the time required for segmentation of individual tissues such as the eyes that comprise less than a 0.2% of the entire heads volume [226, 227].

Following isolation of the neurocranial region, the tissues within the skull were segmented into white matter, grey matter, and cerebral spinal fluid (CSF). This was performed by applying an intensity threshold to obtain core regions for each tissue type followed by level step contour fitting [224] to find boundaries between tissues. First, the CSF was isolated using an intensity threshold equal to the neurocranial region mean - 1.5 standard deviations, selecting the lower 6.68% voxels in the neurocranial region, which is approximately the total volume of CSF (Wright, Lai, and Sinclair 2012). With the CSF voxels defined they were removed from the neurocranial region leaving only brain voxels. To segment the white matter and grey matter the brain is first thresholded at mean value + 0.1 standard deviations to select the upper 46% of tissue which corresponds to the white matter assuming a 1.2:1 grey matter to white matter ratio in humans [228]. With a rough mask defined for the white matter a Chan-Vese model level step contour fitting algorithm was applied to define the boundary between white and grey matter and segment white matter from grey matter.

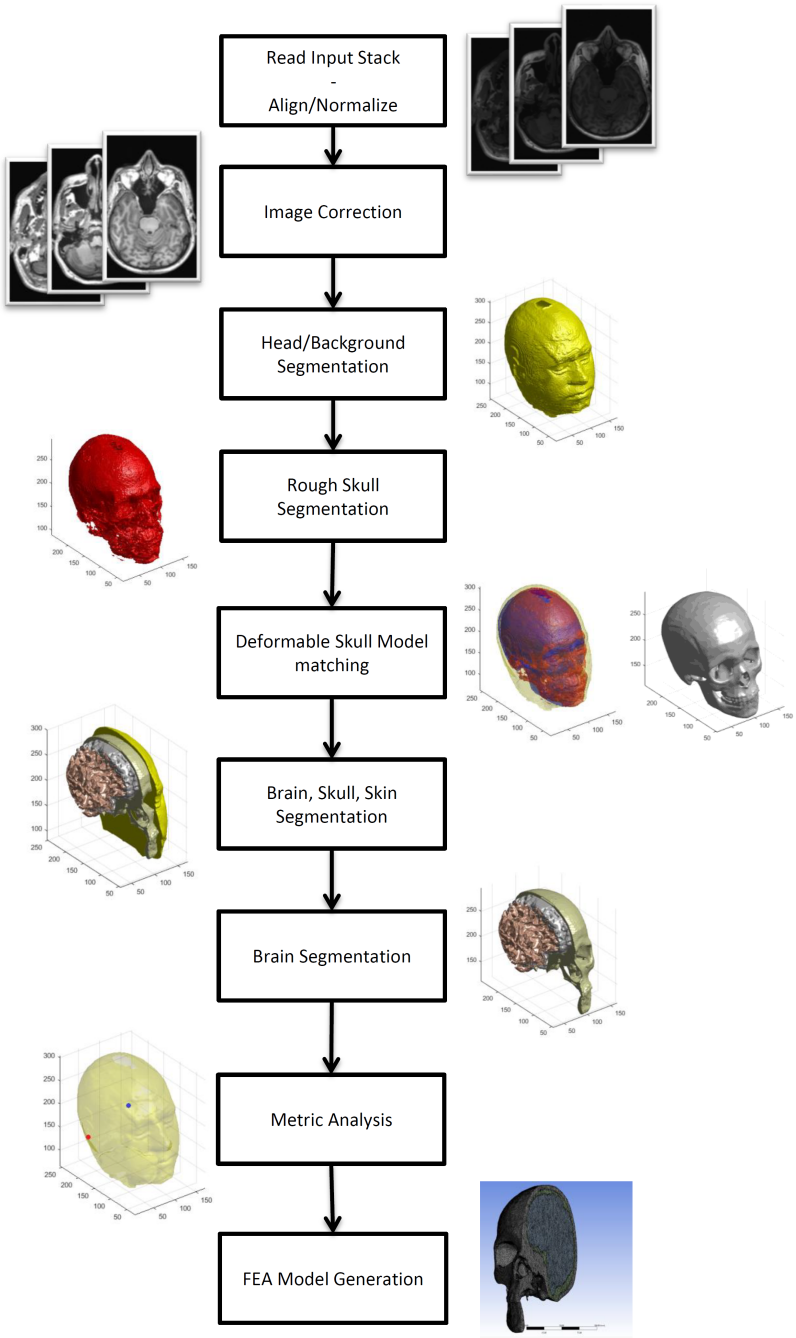

Fig. 4.1. Head segmentation stages with samples of the processing performed at each stage.

The overall process is illustrated in figure 4.1. In breif the images accompanying stages of processing are as follow: Align Input Stack) sample slices of raw T1 input stack; Image Correction) sample slices from corrected image stack; Head/Background Segmentation) 3D volume rendering of isolated head; Rough Skull Segmentation) 3D volume rendering of initial skull segmentation; Deformable Skull Model Matching) On the left is an overlay of the head volume (yellow), the initial skull segmentation (red), and the fitted skull model (blue) and on the right is the model head volume isolated; Brain, Skull, Skin Segmentation) Sliced segmented head [white matter tissue = pink, grey matter = grey, skull = tan, and skin-muscle = yellow); Brain Segmentation) Sliced segmented head [white matter tissue = pink, grey matter = grey, skull = tan); Metric Analysis) Volume rendering of head with points for the center of mass (blue) and mastoid process (red) labeled; Finite element analysis (FEA) Model Generation) Meshed volume of a head geometry generated by this program and imported into ANSYS 19.2.

With each head tissue segmented and defined, the voxelized masks and surface geometries for each tissue are exported for finite element models and post-processing. To prepare the segmented tissue maps for conversion to surface geometries small regions of disconnected tissue, less than 500 $\text{mm}\hat{3}$, were removed from the tissue masks and inversely small holes were filled in other masks. This is to prevent small geometric artifacts from complicating the FE model generation or creating singularities when simulating. Isosurfaces were extracted from the masks via Matlabs isosurface function and then smoothed using the smoothpatch function developed by Dirk-Jan Kroon [229]. The surface mesh is processed via the iso2mesh package to repair non-manifold surfaces, remove intersecting faces, patch holes, and reduce the number of faces prior to exporting the geometry as a finite element ready STL and SAT file [230–232].

4.3.4 Calculating Head Metrics

With the head tissues segmented into skull, white matter, grey matter, CSF and skin-muscle regions measures of the head geometry are taken, including: head width, head length, head circumference, skull width, skull length, ellipse fit of skull, ellipse fit of head, head mass moments, top of head (superior-most point of the head) coordinates, back of head (posterior-most point of the head) coordinates, head centroid coordinates, and right mastoid process coordinates.

Head and skull sizes were measured by voxel analysis at the transverse volume slice which contains the largest area masked by the head or skull respectively which corresponds with the location of the brow. At this transverse volume slice, the outer perimeter of the head or skull was isolated and used to calculate: length, distance between most anterior point to most posterior point; width, distance between furthest points perpendicular to length; and elliptical measures of circumference, length, and width by fitting an ellipse to the target tissue. The top of the head was measured as the most superior voxel in the head scan if there were multiple points that are most superior their position is averaged. Similarly, the back of the head is the most posterior point in the scan or the average of the most posterior points. For these analyses volumetric measure of maximal head thickness rather than fixed points on the head was used to define the region for measurement, this was selected as persons with different head geometries may have thickest regions of their heads associated with different regions of their skulls and by extension the deformable skull model.

The heads center of mass (CoM) was calculated by assigning each voxel (1 mm3) segmented in the head a mass associated with voxels assigned tissue type, then calculating the weighted centroid of the head. In this analysis, the head was defined as the tissues internal or within 5 cm of the skull. The tissues densities used in this study were 1026 kg/m3 for brain matter, 1007 kg/m3 for CSF, 2100 kg/m3 for skull, and 909 kg/m3 for skin-muscle. This produces a center of mass for the head that can be used with either a simplified for complex neck model to simulate impacts and their

associated forces on the brain. To caluclate the mass of the head and any individual tissue is simply the sum of all the weighted voxels comprising the tissue.

The mass moments of inertia, I, for the head were calculated using the distributed masses method.

$$I = \sum imiri2 = m1r12 + m2r22 + ... + mnrn2 \tag{4.3}$$

where I = inertia, mi=voxel masses, and ri=voxel distances to CoM or axis. For this calculation, the same tissue densities per voxel as in the CoM calculation and the individual Euclidean distances were measured between each voxel and the CoM or axes running through the CoM.

Finally, the coordinate of the mastoid process was obtained by selecting a constant point to represent the of the mastoid process on the adapted skull geometry and finding the surface of the skin directly above the mastoid process point. The mastoid process was examined as it is a common site for head accelerometers to be attached to the head and the distance/orientation between that point and the head centroid is crucial for accurately transforming the measures at the sensor to accelerations of the head at its centroid 4.1.

4.3.5 Simulation Geometry Generation

To make full use of the player specific geometry generated by the segmentation program ANSYS ready simulation geometry files were generated. To generate ANSYS compatible geometries from the existing tissue masks the masks were first simplified to allow for finite element model (FEM) simulation. This involved removing small isolated regions of tissues (less than 1000 mm^3) switching it over to the largest neighboring tissue type, thickening regions less than 3 mm thick to 5 mm, smoothing contact interfaces and removing sharp geometry. While this does alter the geometry slightly it is necessary to generate geometry that will solve in ANSYS without generating errors. With changes to the masks performed a surface mesh is extracted from the masks for each tissue type (skull, white matter, grey matter, CSF, ventricles,

skin/muscle. Due to the need to provide perfect contact faces between the different tissue types as recognized by ANSYS, the tissue surfaces are generated as solid volumes with no holes. This requires that tissues internal to other tissues be subtracted from one another in ANSYS before simulation, but through this method, a perfect contact surface between every pair of tissues is can be assured. The surface meshes are then down-sampled to 10% of the original density to allow for faster simulations and reduce the complexity of the generated FEM. Generated meshes are then checked from errors or non-manifold faces via ISO2Mesh's mesh checking utility before being saved as a faceted STL body.

4.3.6 Segmentation Validation

To validate the segmentation performed by the algorithm described in this paper, a pre-segmented data-set from the McConnell Brain Imaging Center was used as a validation input (Aubert-Broche, Evans, and Collins 2006). The validation data set contained a T1 weighted MRI scan of the head and a validated segmented map of the different tissues in the head. Using the T1 as an input to the segmentation program, a processed segmentation map was generated and compared against the validation segmentation map.

In addition to validating the head segmentation system by segmenting a test data-set, the segmentation system was tested on its ability to accurately measure head sizes in athletes of different ages and genders. The head metric analyzed in this analysis was the circumference of the head collected from the high school athletes scanned. The metrics from these segmentations were compared to CDC metrics of adolescent head sizes [22, 233](Schmidt et al. 2014).

4.3.7 Acceleration Data Collection

To examine the accelerations of a standard head model in situ data was collected using the Hybrid III Headform (H3H) for the 50th Percentile Male (Humanetics; Ply-

mouth, MI). The H3H houses a nine-accelerometer National Instruments Accelerometer (NI; Austin, TX) array in a 3-2-2-2 setup on the inside of the headform that sits at the CoM [182, 234, 235]. The H3H was struck a total of 280 times (20 times each across 7 different locations (Figure 4.2), at 2 different angles of impact (normal and oblique)), with a Model 086D20 Impact Hammer (PCB Piezotronics; Depew, NY). These 20 hits were subdivided into four hits each at five distinct impulse ranges found to cover a majority of the acceleration experienced by helmeted football players (2-4Ns, 5-7Ns, 8-10Ns, 11-13Ns, and 14+Ns) [234]. The accelerometers inside the H3H are used to directly calculate the translational acceleration at the center of mass (CoM) and derive the angular acceleration [235]. The angular velocity was derived by numerically integrating the angular acceleration and any linear drift in the signal was removed.

4.3.8 Subject Specific PLA Calculations

The linear accelerations at the center of mass of the H3H were transformed to solve for the linear accelerations at the right mastoid process. Rigid body dynamics was used to perform different transformations.

$$a_A = a_B + \alpha \times r_{B->A} + \omega \times \omega \times r_{B->A} \tag{4.4}$$

Where a_A is the linear acceleration at point A, a_B is the linear acceleration at some other point B, α is the angular acceleration of the system, $r_{B\rightarrow A}$ is the vector from point B to point A, and ω is the angular velocity of the system. In this case, A is the mastoid process and B is the CoM of the H3H.

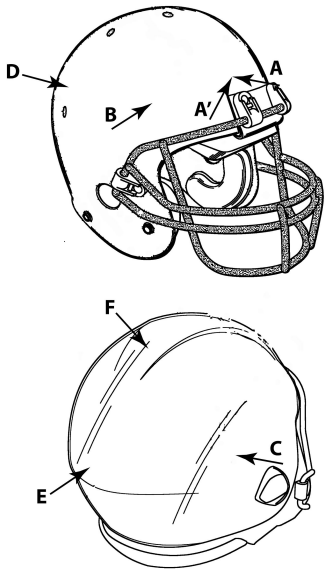

Fig. 4.2. H3H impact testing locations A through F. Figure retrieved from [235].

After the linear accelerations were transformed to the mastoid process, the PLA for each impact was calculated using each players individual radius vector from the mastoid process to the players CoM (point A is the CoM of the player and B is the mastoid process). For each location and angle, the PLAs were separated by the impulse of the administered hit. At each impulse level, the player average PLA was calculated to a single data point existed for each player at a given impulse level. The H3H PLA output was also averaged for each location, angle, and impulse level combination. Histograms for the distribution of the player specific PLAs with the respective H3H PLA measure were generated to examine how using player specific radii affects the PLA.

4.3.9 Statistics

Statistical analysis was performed using SAS 9.4 (SAS Institute; Cary, NC). Head geometry metrics of the male and female athletes were compared using a t-test or the

Wilcoxon Rank-Sum test (if normality and constant variance assumptions were not satisfied).

4.4 Results

As can be observed in figure 4.3 the head segmentation program provides an accurate reconstruction of the head without the need of manual tissue labeling, even when only partial or noisy scans of the head are available. Segmentations with this program took an average of 36.1 minutes$\pm$2.7 minutes on a computer with AMD Ryzen Threadripper 1920X CPU with all cores at 3.85 GHz. The skull model fitting can be accelerated by performing the analysis at half resolution. In these cases then an additional fitting stage 4 is performed at full resolution to improve final model alignment and improve model skull matching for details lost when scaled down.

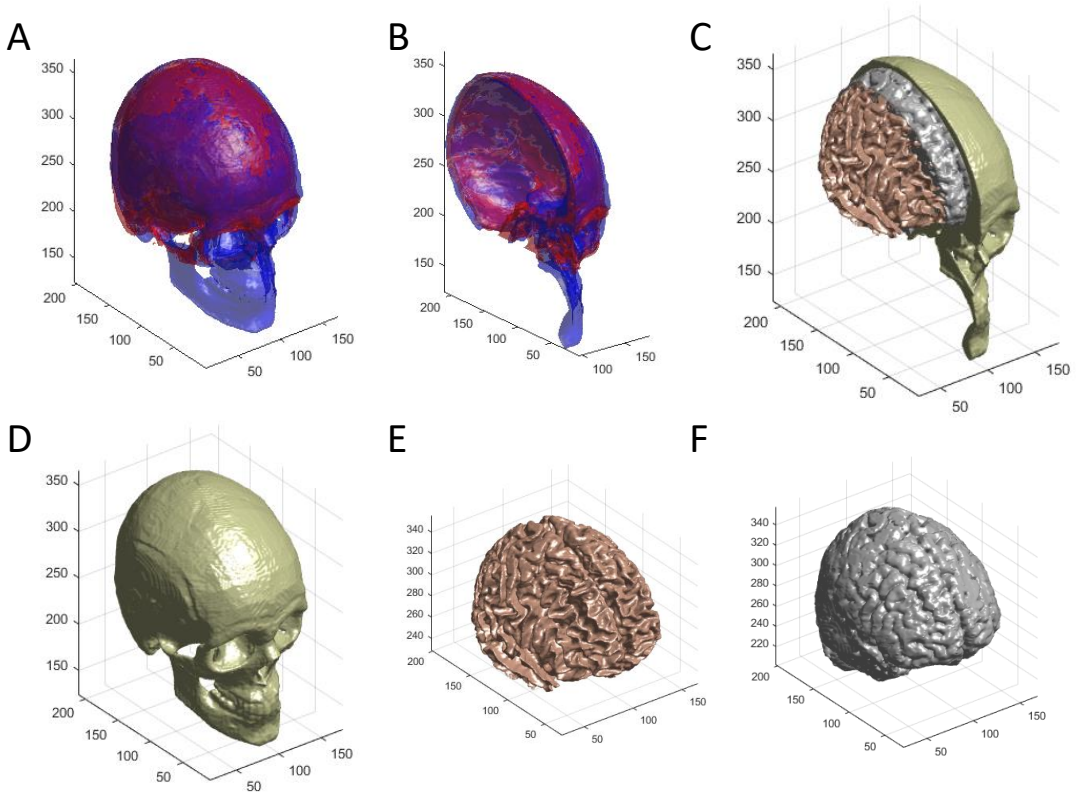

Fig. 4.3. Segmentation of Validation Dataset. A) Overlap of validation skull (red) and segmented skull (blue), B) cross section of overlap between validation and segmented skulls, C) volume rendering of white matter (tan), grey matter (grey), and skull (off white), D) volume rendering of skull, E) volume rendering of white matter, F) volume rendering of grey matter.

4.4.1 Validation Results

The first set of validation analysis was performed on a complete MRI scan of a head with minimal noise. Processing the image stack was compared to the pre-segmented regions and the different tissues had the following accuracies: whole head exterior = 99.31%, skull = 82.87%, skin-muscle = 88.343%, white matter = 94.82%, grey matter =75.32%, and overall brain = 93.77%.

The second validation method compared the metrics obtained from processing the head scans of high school athletes of different ages and genders to metrics of those groups previously published in literature [21, 22](Schmidt et al. 2014). Segmenting the MRI scans from male football players and female soccer players we observed the following trends. Overall, males typically had larger head metrics than their female counterparts (Table 4.1). The measures extracted from the head scans are comparable to the results reported in other studies from field measurements [21, 22].

Table 4.1.
Extracted head metrics for males and females in cm (*indicates p-value<0.05 for the measurement between males and females). The median (1st, 3rd quartiles) and mean (standard deviation) were calculated for each group.

Metric	Lycke et al.				Roche et al. 1987		Schmidt et al. 2014	Cordeiro et al. 2015 (Skull measurements)
	Male (n=167)		Female (n=53)		Male (n=717)	Female (n=544)	Male (n=34)	(n=23)
	Median	Mean	Median	Mean	Mean	Mean	Mean	Mean
Length*	20.6 (19.8, 21.3)	20.6 (1.12)	19.6 (18.9, 20.2)	19.7 (0.92)	N/A	N/A	N/A	17.7
Width*	16.6 (16.3, 16.7)	16.5 (0.27)	16.1 (15.7, 16.3)	16.0 (0.46)	N/A	N/A	N/A	11.2
Circumference*	56.1 (54.5, 61.7)	58.0 (5.32)	53.1 (51.8, 54.4)	54.0 (3.69)	55.6	54.38	58.4	N/A

4.4.2 Head Geometry Generation

In addition to head metrics and voxel masks generated by the head segmentation program, a player specific ANSYS compatible geometry is produced for simulations. This player specific geometry has only previously been achieved with multi-level systems using commercial segmentation suites followed by geometry generation code,

and even then only accurate geometry for the brain and CSF was generated [236]. The geometry generation performed by this program is completely automated and allows for direct importing of the geometry to ANSYS without any post-processing (Figure 4.4).

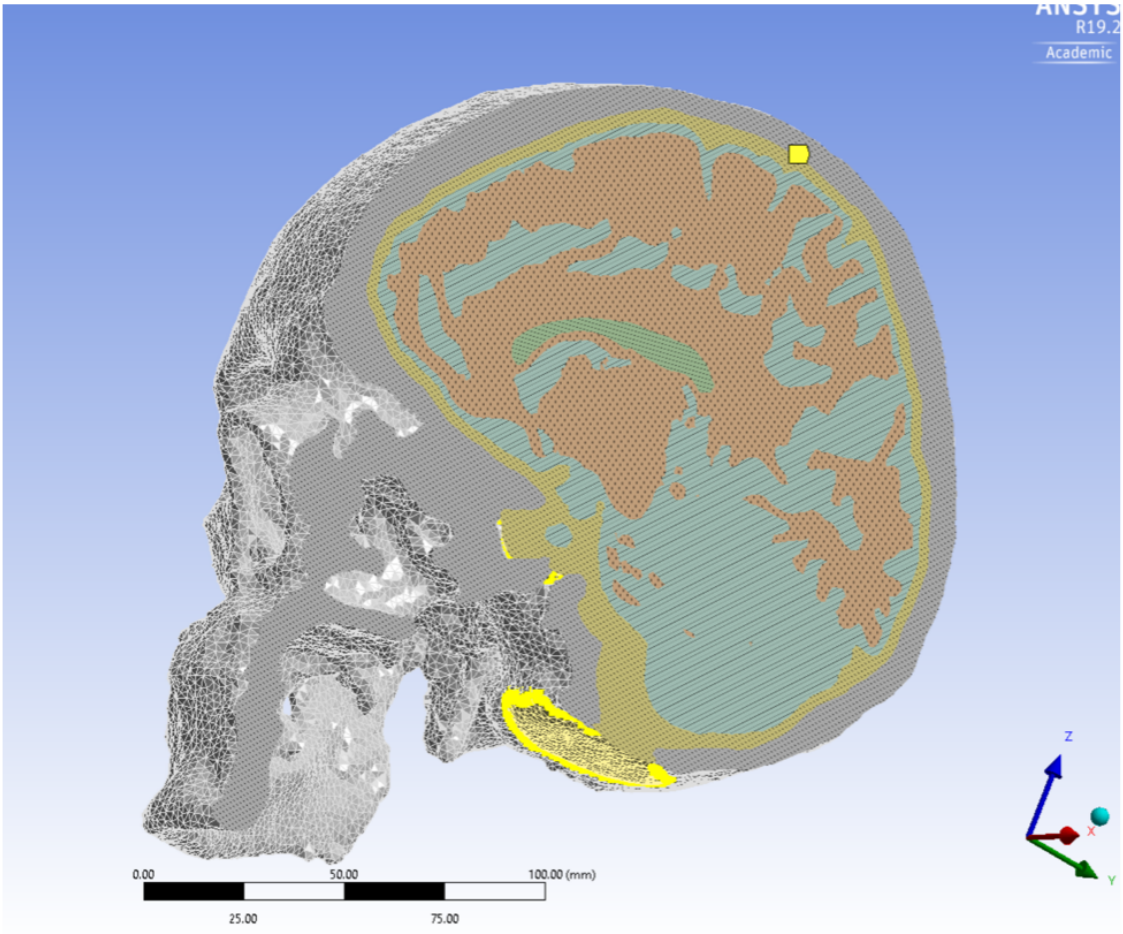

Fig. 4.4. Player specific meshed volume of a head geometry generated by the head segmentation program imported into ANSYS 19.2. Tissues types denoted with the following colors: Skull = White, CSF/Menegies Yellow, Grey matter = Teal, White matter = Orange, Ventricles = Green.

4.4.3 Subject-Specific PLA Calculations

The variability in the PLA calculation due to the subject-specific radii used in the rigid body dynamics calculation causes a substantial difference in the measurement when compared to the H3H vector which is based on the 50th percentile male 4.5. For the different locations and impulse ranges, the H3H PLA typically lies on the left tail of the histogram created by the subjects, sometimes entirely below the 95th percentile of the distribution (Fig. 4.5). The difference between the players and the H3H is more substation when oblique hits are administered (Fig. 4.5).

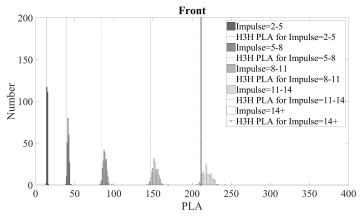

(a) Front

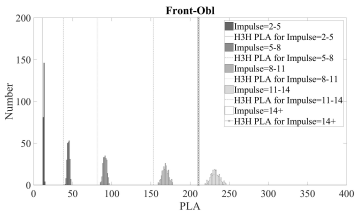

(b) Front Obique

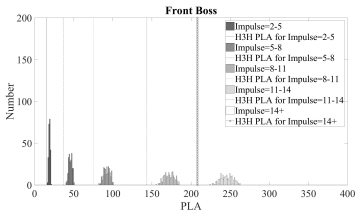

(c) Front Boss

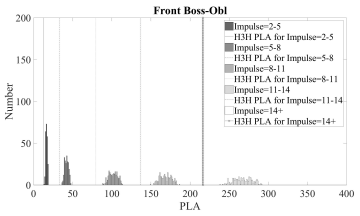

(d) Front Boss Oblique

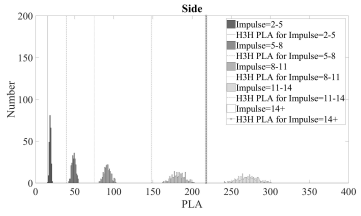

(e) Side

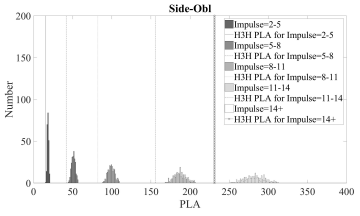

(f) Side Oblique

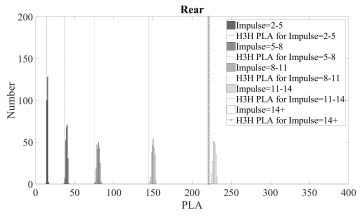

(g) Rear

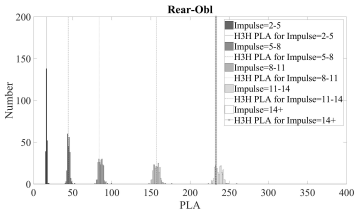

(h) Rear Obique

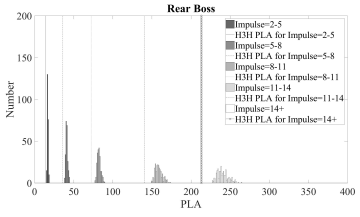

(i) Rear Boss

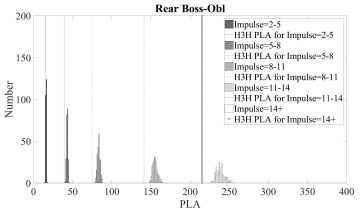

(j) Rear Boss Oblique

Fig. 4.5. The H3H PLA calculations tend to underestimate the PLA compared to the PLA calculated when a subject-specific radius vector is used for the transformation of the acceleration data, especially when examining the high impulse groups.

4.5 Discussion

In this paper, we have demonstrated the functionality of a novel head segmenter, an autonomous program for segmenting T1 MRI scans, a scanning paradigm well suited for analyzing large groups of individuals as they provide anatomical details and take only minutes to run, and quantifying the whole head. While many existing head segmentation programs can perform quality segmentation of the brain, they focus solely on analyzing the brain (CITE), whereas the segmenter presented here can segment the entire head identifying white matter, grey matter, CSF, skull tissue, and skin-musculature; a necessary task if holistic modeling of the head is to be performed. In addition to segmenting the tissues of the head, this program has demonstrated its ability to quantify a variety geometric metrics of the head including mass, volume, size, mass moment, and feature locations (mastoid process) useful for developing complex models of the head and calculating how forces are applied to the brain.

The segmenter was also designed to handle noisy and partial MRI datasets a scenario common in studies examining larger populations. This capability was first tested with a validation dataset only consisted of the upper 15 cm of the head yet demonstrating high segmentation accuracy and further validated when analyzing several seasons of high school athletes whose scans were focused on the neurocranial region and producing segmentations and metrics that matched existing published measures. This is a valuable feature that adds robustness to the analysis and allows the head segmenter to function as an automated tool in the analysis of large batches of scan data from athletes providing metrics useful for modeling their individual responses to head impacts or other forces applied to the head.

As previously mentioned, current sensor systems do not account for the unique vector of each athletes head from the sensor location to the CoM which may lead to inaccurate measures of the acceleration at the CoM. This segmentation tool is able to extract the location of the CoM the head which allows for a personalized PLA calculation for each player. It was seen that the H3H PLA calculation typically

underestimated the PLA relative to the player specific PLA calculations. This means that even if an acceleration monitoring system is validated on the H3H and uses only a single algorithm to perform the transformation of acceleration from the sensor to the CoM, it is likely the actual accelerations in vivo will be drastically underestimated by the monitoring system. This can lead to inaccurate field measurements, threshold guidelines, and design criteria for preventing neurological changes.

The increased angular acceleration and velocity of oblique impacts results in more variation in the PLA measures when using individual radii in the transformation. The angular acceleration and velocity measures contribute to the transformed PLA by multiplying them with the radii for the player, so the more rotational the impact, the greater the contribution those components will have to the PLA. And since the radii vary from player to player, the more the rotational components contribute to the PLA, the greater the degree of variability in regards to the PLA spread. Although it has been speculated that rotational acceleration measures cause concussions and other soft tissue related brain injuries, this analysis demonstrates that this conclusion may be the result of inaccurate or incomplete incorporation of the angular measures into the PLA calculation and that there may exist a linear acceleration threshold above which symptoms become present.

Segmentation of the head into FEA compatible geometries is a unique challenge due to the conformation and properties of the various component materials. Generating and separating the regions of the skull, CSF, white matter, grey matter, skin, and muscle is performed by this segmentation program such that meshing valid geometries are produced that can be assigned their unique properties in ANSYS or other FEA software programs. After accurate mathematical models for single impacts are created and validated, the ideal role of this segmentation program is to generate the player-specific geometries with player-specific input conditions from the unique HAE series collected by on-head sensors to predict localized regions of damage that can be compared to MRI measurements at the pre-, in-, and post-season time points in any collision or contact sport.

4.6 Conclusion

This study has discussed and demonstrated the ability of the presented segmentation to accurately and autonomously analyze T1 MRIs of contact sport players, providing a valuable tool to process for investigating the mechanics and health of players in contact sports. The primary advantages of presented segmentation system are its ability to autonomously segment noisy MRI scans with a focus primarily on the brain and still provide accurate measures of the head, skull, and brain as demonstrated against validation datasets and measures of youth athletes. Additionally, since the program was written entirely in Matlab and designed to process batches of MRI scans autonomous it has the ability to analyze large collections of scans any system supporting Matlab and equipped with modest hardware making it a tool available to researcher and athletic physicians alike for quantifying applicable metrics of the head and developing personalized simulation models.

Without appropriate head size measures, athletes will have underestimated linear accelerations at their respective CoM measurements. A single approach to assuming a large, small, or average head would be insufficient for an accurate model that aims to quantify the amount of acceleration a player has been exposed to and we must use individualized measures to improve safety and research into TBI. Systems for quantifying the head and its individual geometries, as demonstrated in this chapter, are ways that researchers and athletic trainers/physicians can accurately monitor head accelerations and, if need be, intervene for a players health.

5. EVALUATION OF A MICRO ECOG ARRAY

Material found in this chapter has appeared journal publication

5.1 Abstract

In an effort to develop a more stable neural interface, the Williams et al. developed a micro ECoG array designed for subdural and epidural stimulation rather than an implant that penetrated the cortical surface. After examining the device's electrical performance on test benches and in-vitro environments researchers examined its chronic performance in an in-vivo study. The aims of this study were to quantify the histological, electrophysical, and behavioral response to the probe. In this study, the researchers examined the ability to stimulate the temporal lobe via subdural μECoG electrode array. These novels (at the time) devices were miniaturized versions of ECoG arrays that many brain researchers are familiar with, but by implanting the electrodes subdurally researchers were able to obtain improved measures of the brain activity and directly stimulate the cortex.

5.2 Introduction

In recent years the advances in neural electrode design and stimulation parameters have shown promise for treating many neural diseases and disorders. Regrettably, many of these advances are still limited by the inability of neural interfaces to function chronically in vivo. In order to develop clinically-relevant neural interfaces that can treat disorders such as sensory loss or limb loss, chronically functional high channel density devices are needed to record neural activity and stimulate the brain. Many of the highest channel density neural implants are penetrating devices such as microwire

arrays, 2-dimensional silicon penetrating arrays, and linear silicon arrays. The current hypotheses suggest that these penetrating devices become non-functional after implantation due to the brains chronic immune response [43, 49, 79]. The immune response is characterized by an acute stage, where there is cell response to the initial brain trauma, and a chronic stage, where the brain enters a state of device rejection producing the signature glial sheaths believed to be the primary cause behind device failure [61]. But, there is a type of neural interface that can avoid this chronic immune response and provides sufficient channel density to effectively interface with the brain: electrocorticography (ECoG) arrays. Placed on the surface of the brain, ECoG arrays avoid evoking the same immune response as seen with penetrating electrodes while still offering high channel density. ECoG arrays have also been shown to work well in human subjects as they are used in the treatment of seizures, control of remote prostheses, and have been used to successfully evoke somatosensory sensations in human patients [125–128]. In this study we evaluated a μECoG array, an ECoG scaled down to increase site density and sensitivity along with a control penetrating electrode. We monitored the degree which these devices were affected by the immune response and gauge their ability to evoke behavioral responses over time.

5.3 Methods

5.3.1 Animals

For this study, 3 male Sprague-Dawley rats (350-400 g) approximately 5 months of age were implanted with μECoGs arrays (2 rats) and penetrating electrodes (1 rat). The laboratory animal protocol for this work was approved through the Institutional Animal Care and Use Committee of Purdue University (West Lafayette, IN, USA), and conforms to the guidelines of the US National Institutes of Health.

5.3.2 Electrodes

The micro ECoG electrode arrays in this study were fabricated by layering parylene-c and photolithography patterned iridium leads bringing the overall thickness of 5 um with an inter-site distance of 750 um between contact sites. Two types of electrodes were used for this study, a μECoG array and a penetrating Michigan array. The μECoG arrays in this study were developed by the NITRO Lab of the University of Wisconsin and are similar to a previous rat ECoG arrays developed by the same lab [132]. The electrode consisted of 16 contact sites coated with a layering of 10 nm of Cr, 200 nm Au, and 20 nm of Pt measuring 200 m in diameter and arranged in a 4 by 4 array with rows spaced on a 750 m pitch on a flexible Paralyne substrate. The penetrating electrode used in this study was a 16 channel four shank silicon microelectrode array with iridium oxide sites of 1250 m2 spaced on a 200 m pitch (NeuroNexus Technologies, Ann Arbor, MI). All sites on the penetrating array were located at a depth between 800 m and 1600 m.

5.3.3 Surgery

The devices were implanted epidurally over the temporal lobe of the rats under a bone flap made in the skull (as to reduce the loss of skull and improve the local. The implantation surgeries performed in this study were similar to procedures performed in previous publications by our lab with the modification made for the implantation of the μECoG arrays [237]. In brief, animals were anesthetized using 1% to 5% isoflurane/oxygen mix at a flow of 1.5 to 2 liters/minute and monitored throughout the surgery to maintain a reflexive state as monitored by toe pinch tests. The μECoG craniotomies in this study were made by drilling away the skull over the primary auditory cortex of the right hemisphere so that a square 3 mm by 3 mm flap of bone remained. This was accomplished by drilling through the bone on 3 sides of the square and thinning the last side (lower edge of craniotomy). Once a bone-flap was made, the μECoG was placed epidurally onto the auditory cortex by hand and

secured by pushing the skull back into position and then applying dental acrylic over the bone-flap. To secure the implant and connector, 4 titanium bone screws (size 2-56, United Titanium, Ohio, US) were inserted into the skull, 2 anterior and 2 posterior to craniotomy and additional dental acrylic applied. A small wire was connected to one of these bone screws prior to dental acrylic application to serve as the electrical ground.

5.3.4 Electrical Monitoring

Complex impedance spectra and cyclic voltammograms were taken every day for the first two months of implantation and then twice a week after until the animal was sacrificed. The impedance magnitude and charge carrying capacity were measured using an Autolab potentiostat/galvanostat (Metrohm Autolab, Netherlands) with techniques previously published by our lab [238]. In brief, impedance spectra were taken with frequency sweeps from 100 Hz to 10 kHz logarithmically spaced, repeated 3 times and averaged to calculate site impedance magnitude. Charge carrying capacity was recorded by performing cyclic voltammetry sweeps on each of the electrodes sites, using 3 sweeps and averaging for each site.

5.3.5 Behavioral Task

The behavioral task performed in this study was a conditioned avoidance task previously performed by our lab in studies examining signal detection and discrimination [237, 239]. In brief, the animals were placed on a water-deprived regime and then presented a water spout during testing. Trials began once rat licking was detected. Two types of randomly ordered trials were presented to the animals: safe, where no stimulus was presented, and warning, where a 650 ms warning tone (acoustic training) or pulse train (implanted electrode) was presented. A hit, or successful detection of the stimuli, was recorded for warning trials when animals did not lick the spout during the last 200 ms of the trial. A miss, or unsuccessful detection of

the stimuli, was recorded for warning trials when animals continued to lick the spout during the last 200 ms of the trial and the animal was given a 1.6 mA shock via the spout. Animals were trained on auditory stimuli before surgery then tested using electrical stimulation after device implantation. Stimulation to the electrodes was delivered via an MS16 stimulus isolator (Tucker-Davis Technologies, Alachua, FL) and consisted of a 650 ms cathode leading pulse train of symmetric biphasic pulses with 205 s pulse duration and variable current level (approximately 20-300 μA). To determine the behavioral detection threshold to a stimulus an adaptive paradigm was used where the stimulus amplitude was modulated based on the detection performance of the animal. When the animal successfully detected a warning stimulus the stimulus amplitude was lowered and when a warning stimulus was not detected the stimulus amplitude was raised. After 5 reversals the trial was concluded and the average level of the last 5 reversal stimuli was taken to give a 50% detection threshold.

5.4 Results

5.4.1 Chronic Impedance and Charge Carrying Capacity

One method of evaluating the performance of a device in vivo is to measure the impedance over time. This impedance measure indicated whether the device is functioning normally, partially isolated from the brain, or broken. The higher the impedance, the more isolated from the brain the device is by glial cells [76]. A chronic analysis of the μECoGs impedance compared to a representative penetrating electrode [42] (Figure 5.1). From this figure we can see the impedance for the μECoGs rises shortly after implantation, indicating immune response acting upon the electrode, but returns to approximate baseline after 3 weeks indicating a cessation of the initial immune response. After 1 month, the μECoG devices maintain stable impedance with a smaller increase over time relative to the penetrating electrode. Comparing the average μECoG impedances against those of the penetrating electrode we saw a significantly lower impedance over time with μECoG (Students t, $p < 0.0001$).

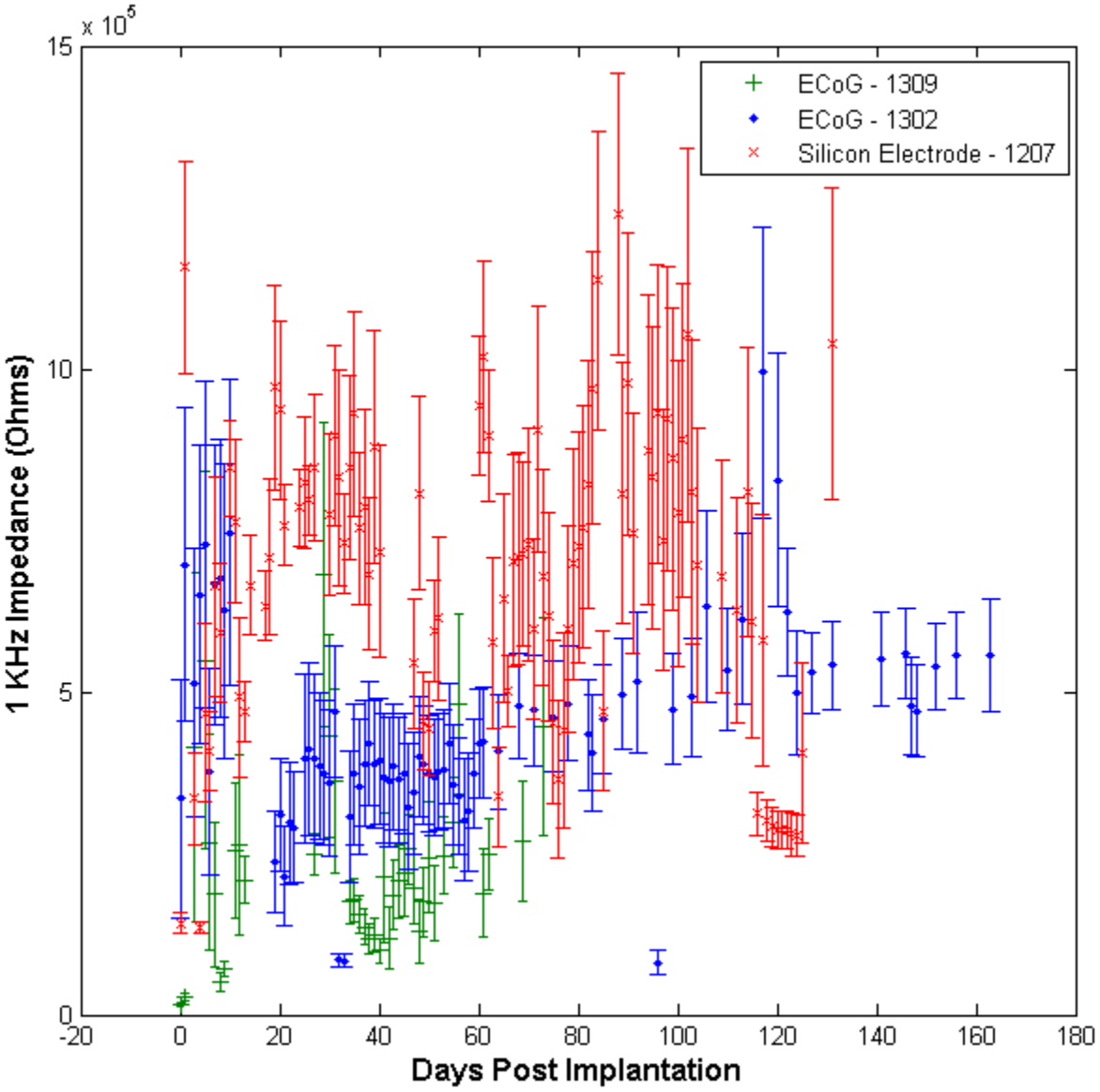

Fig. 5.1. Chronic Impedance Magnitude. The 1 kHz impedance of contact sites for μECoGs (Blue, Green) and a penetrating electrode (Red) over time post implantation. Error bars show standard error.

Another method of evaluating the performance of the device is by measuring the charge carrying capacity of the electrode sites. The charge carrying capacity

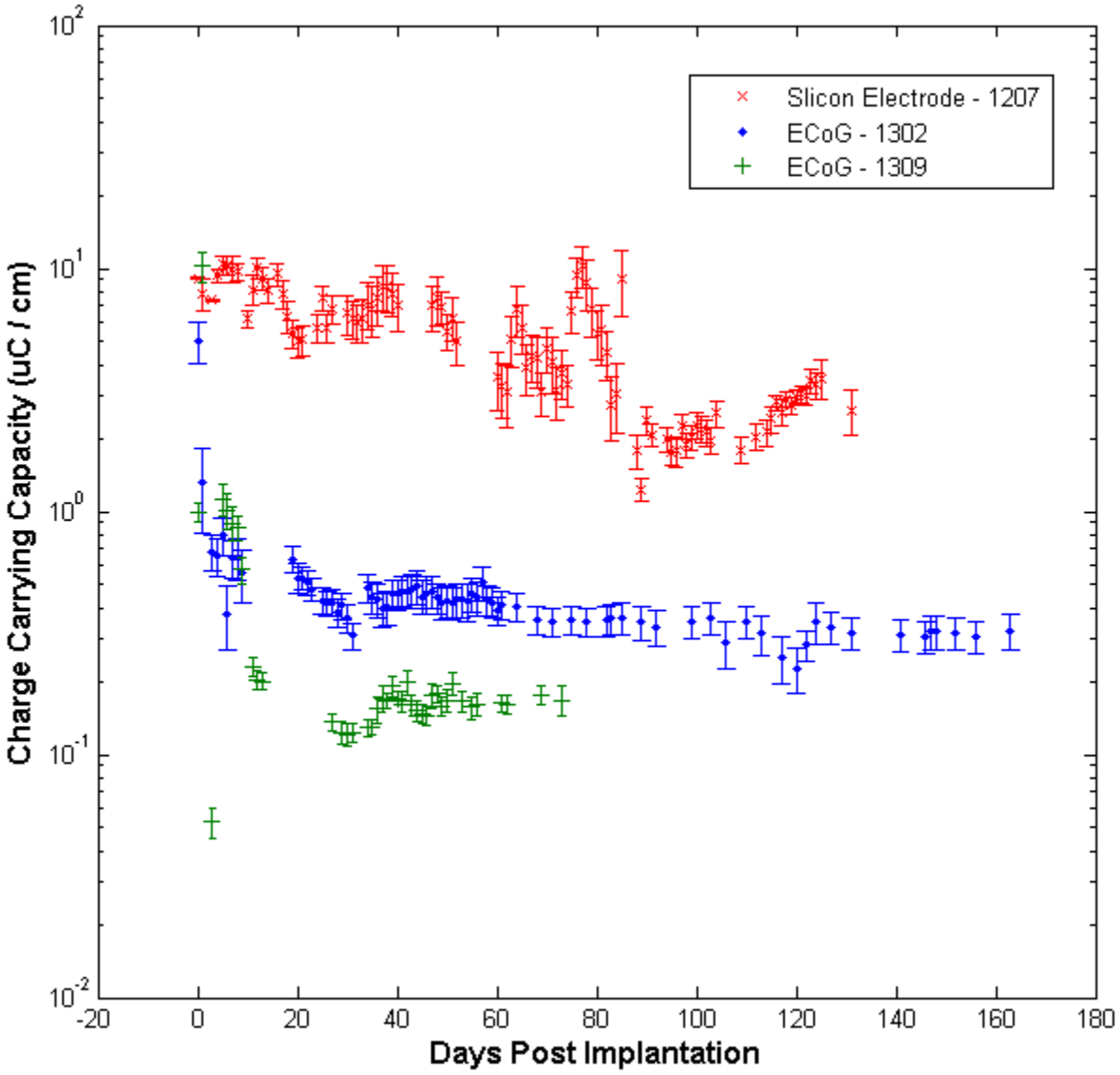

Fig. 5.2. Figure 2. Chronic charge carrying capacity of μECoG arrays (Blue, Green) and a penetrating electrode (Red) over time post implantation. Error bars show standard error.

describes the amount of charge that an electrode can store which is important for performing stimulation as it is the charge on the electrode that stimulates neurons

rather than just the current passing through the electrode [240]. Thus the lower the charge carrying capacity the less effective the device is at stimulating the local environment. The chronic charge carrying capacity of the devices is shown in (Figure 5.2). A sharp and significant decrease in charge carrying capacity of the electrodes is observed immediately post-implantation. This decrease, though substantial, appears only once and the charge carrying capacity does not decrease further after extended time implanted. Statistically analyzing the data-set we find that the ECoG rats have a significantly lower charge carrying capacity compared to the penetrating electrode (Tukey HSD, $p < 0.0001$)

5.4.2 Behavioral Detection Thresholds

A third measure used to evaluate the functionality of the devices was the animals performance on a behavioral task. The behavioral thresholds obtained from this task describe the lowest stimulation threshold the animal was able to detect 50% of the time. Fig. 3 shows the trend of behavioral thresholds over time. Initially, the μECoG detection thresholds are similar to those for penetrating electrodes, but over time we observe that the thresholds decrease indicating increased sensitivity to the stimuli. The detection thresholds also appear to be stable at extended time points post-implantation with no significant increase in detection threshold observed after 2 months implanted (Tukey HSD, $p>0.05$). Additionally, μECoGs show significantly lower in detection threshold over time than penetrating electrode ($p<0.0001$), and no significant changes in detection thresholds post 2 weeks implanted ($p>0.05$), suggesting chronic stimulation stability.

5.5 Discussion

Our analysis of the impedance, charge carrying capacity, and behavioral detection thresholds over time indicate that the μECoG developed by the NITRO Lab is a stable platform for stimulating the cortex of a behaving rat. The impedance of the μECoGs

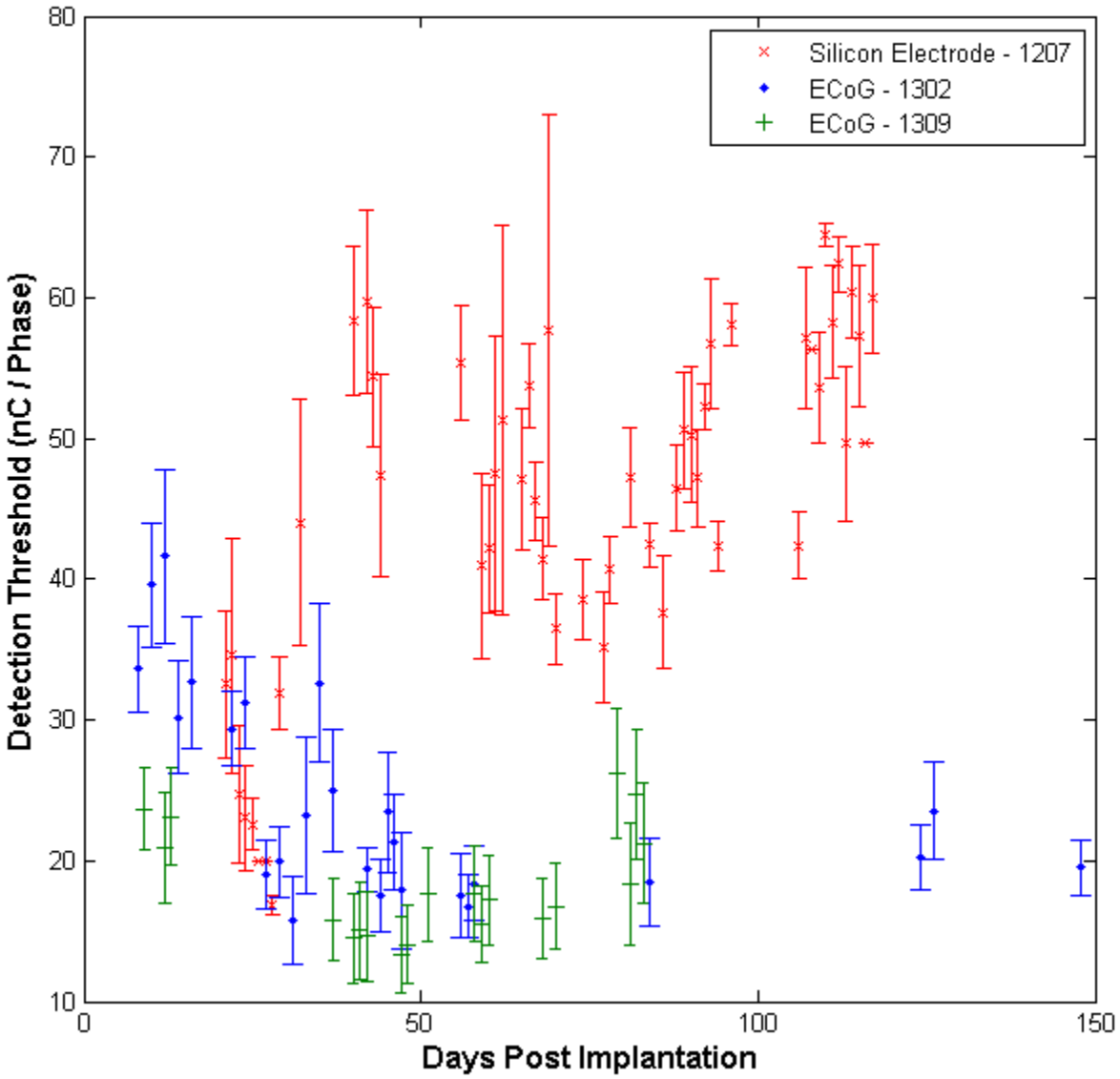

Fig. 5.3. Chronic behavioral detection thresholds Behavioral thresholds measured in nC/phase over implantation period for two μECoGs (Blue, Green) and a representative penetrating electrode (red). Error bars show standard error.

was significantly lower than our representative penetrating electrode and showed little

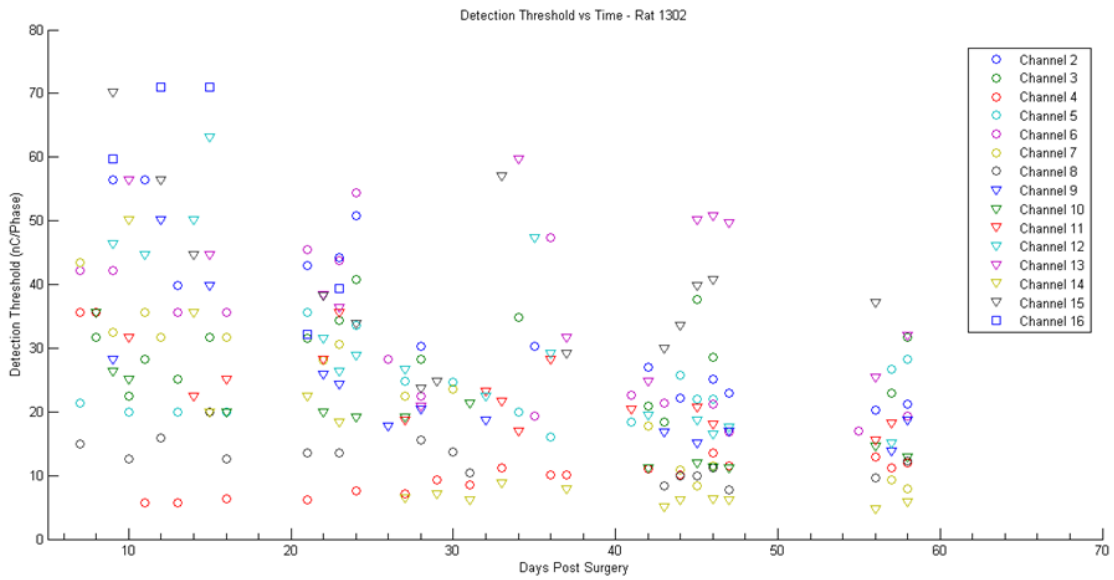

Fig. 5.4. Chronic behavioral detection thresholds for a single animal. Measures of the stimulation threshold required for implanted animal to respond to neural stimulation in behavioral task.

variation over time. Though the charge carrying capacity did decrease faster and significantly more than our penetrating electrodes, the μECoGs were able to still effectively stimulate the animals chronically with a detection threshold comparable or lower than that of penetrating devices [237]. Overall, the μECoG devices showed functionality and high stability over time. This stability is likely due to the ability of the μECoG array to avoid evoking the same immune response as penetrating electrodes. Since, for this study, the dura was never compromised the most probable cause for device impairment comes from sources outside the brains immune system [69, 146]. This is supported by the timeline of the changes observed in the electrical properties which suggest that the implant is not affected by a chronic inflammatory response, but rather the acute immune response. First, the spike in 1 kHz impedance occurs shortly after surgery and returns to approximate baseline 2-3 weeks later; this mirrors the acute immune responses timeline for wound healing and restoration

of the dura. This suggests that the spike in impedance is due to transient effects related to the surgical injury rather than an effect of chronic device rejection/chronic inflammation as we would expect to see a progressive decrease in implant function over time if the chronic immune response was active. The drop in charge carrying capacity also supports this view as it is likely, not due to device failure or glial coatings, but likely due to a quick buildup of collagen fibers on the surface of the μECoG device. If the change was due to the chronic immune response we would expect to see a continual degradation of function as we saw with the penetrating electrode, but rather the changes occur immediately and do not worsen after approximately a week in vivo. Even though the electrical data is promising, the clinical efficacy of the device is best evaluated in the ability to chronically evoke behavioral responses. We see that over time post-implantation the device continues to evoke behavioral responses from stimulation and does not appear to have any significant increases in the threshold current, contrasting what is usually observed with many penetrating electrodes. One aspect of this study which surprised the authors was the generally low stimulation threshold required to evoke behavioral responses. Based on the theoretical volume-conductor hypothesis, the empirical results of the stimulation reported here are in conflict with studies indicating lower thresholds for deep stimulation targets compared to shallow targets [237]. However, this may be due to the larger electrode contact sites being able to affect a large colony of neurons thus obtain similar absolute numbers of responding neurons from that pool or other effects based on the dynamics of the stimulation field. Future research with this device will focus on quantifying and understanding the mechanisms by which these low thresholds are obtained and how stimulation can be improved.

5.6 Conclusions

The goal of this study was to characterize the performance of a μECoG implanted for chronic stimulation. Our study shows that the μECoG maintains low impedance

over chronic implantation with lower variability than penetrating devices, though the charge carrying capacity of the contact sites drop significantly more than penetrating devices. But this does not negatively affect the ability to stimulate as the ability to evoke behavioral responses is stable after the first month and can produce these responses with stimulation levels comparable to penetrating devices.

6. NEURAL ELECTRODE MATERIAL PROPERTIES AND GEOMETRY AFFECT BRAIN DEFORMATION IN RESPONSE TO MICROMOTION : A COMPUTATIONAL STUDY

Material found in this chapter is currently in preparation for publication in a journal publication

6.1 Introduction

Neural implants have demonstrated their potential in treating a wide variety of diseases and disorders including paralysis [241, 242], limb loss [46], deafness [243], Parkinson's [26], and depression [30, 244], but the chronic implementation of these high resolution devices has been limited [42, 52]. This is in large part due to a complex immune response to the implanted electrode resulting in poor performance of microscale neural electrodes implanted chronically and their inability to establish a stable interface with local neural populations [49,61,62,79]. For the most part, only large electrodes such as deep brain stimulators have been able to function chronically stimulating large populations and electrode arrays such as the Utah array which has been shown to work for long periods in humans only have a small subset of functional sites recording neural activity.

The failure of chronically implanted is linked to the immune response. There is a migration of immune cells to the implantation site, dead zone of local neural cells, degradation of the electrode, and formation of a glial sheath, that isolates the implant from the rest of the brain both physically and electrically. Researchers have investigated a variety of factors that contribute to the chronic immune response from ranging including implantation technique, the local neuro-chemical environment, elec-

trical stimulation parameters, protein coatings and the mechanical properties of the electrode. But unlike factors resulting from the initial injury related to the implantation, the mechanical mismatch between the implant and the brain tissue chronically perturbs the local neural environment after other factors have healed or stabilized [59].

The electrodes Youngs modulus is 200 GPa compared to 15 KPa for the silicon electrodes and brain respectively [245]. This large mismatch in material properties has been proposed as a significant source of long-term irritation to the brain tissue due to brain motion and subsequently induced strain in the tissues. In efforts to reduce this irritation and the subsequent immune response researchers have tested a variety of electrodes designs to reduce mechanical strain in the brain. In general smaller and more flexible electrodes performed best [82, 138, 246]. This has been highlighted by recent advances in electrode designs that exhibit ultrasmall cross-sections and high flexibility which demonstrated chronic functionality with little to no observable immune response and allow for a stable connection to local neural populations [139, 247, 248].

While these recent studies demonstrate electrode designs that may function chronically once implanted, the design space of electrodes that could function chronically and mechanisms underlying precisely why these implants perform so well are unknown due to current designs changing numerous variables simultaneously with the development of a new electrode (confounding the aspects changed leading to improved performance) or only examining two levels per factor; such that no relationship between the levels can be determined, only that one performs better than the other.

Computational modeling has the potential to elucidate the effects of design parameters such as electrode size, stiffness, adhesion to the brain, material type, and shape. While performing entire parameter sweeps varying electrode designs parameters through implantation studies with fabricated electrodes is not feasible due to time and cost, performing simulation studies that explore the mechanical design space are not. Past computational studies have observed that reducing electrode size [143], increasing adhesion to the brain / [249], and decreasing device stiffness [82, 83] all

reduced strain produced in the brain and by extension the severity of the immune chronic response. These results agree with observations in the literature that smaller, softer electrodes produce significantly decreased immune response relative to larger and stiffer implants [142] and further confirmed by studies pairing simulations and in vivo analysis [82, 250].

Regrettably, many of the existing simulation studies only evaluate design parameters individually and generally neglect their interactions. While examining individual parameter provide insights on the how they can be adjusted to reduce electrode induced strain in the brain, they do not describe how changes to that single parameter affect others and which combination of parameters are the most significant at reducing the strain. Thus one goal of the current study is to quantify the relationship of the different design factors, how they all contribute to the strain produced in the brain, and determine which are the most sensitive factors in reducing strain.

In addition to the limited analysis of electrode design factors, prior simulation studies have restricted their investigations to micromotion parallel to the length of many neural implants (i.e. the neural implant pushing into the brain). This is likely due to two reasons, the first being a seminal study by Gilletti and Muthuswamy which measured rat brain motion but did so only at the surface of the brain and perpendicular to the cortical surface [80]. As of publication there we were unable to find any similar research studies in the literature that quantify the micromotion of the rat brain at rest, resulting in a limitation of observed micromotion values to implement. The second reason was by simulating the electrode moving into the brain researchers were able to quantify the maximum strain produced by motion and by extension the possible maximal damage that electrodes might induce in the brain. As noted in studies that performed cursory examinations of micromotion loading in multiple axes loading along the length of the probe produced the most strain but if this extends to a variety of material and electrode design combinations are unknown [86, 143, 249]. To examine the brain electrode interface more completely, motion from multiple directions, the effect of different loading directions on the strain,

and how motion interacts with other electrode design parameters will be explored in this study. This study aims to elucidate which design parameters interact to produce the most strain in the brain and techniques that might reduce said strain.

6.2 Methods

6.2.1 Simulations

To examine the mechanical loading that implanted electrodes impart on the brain due to micromotion simulations of implanted electrodes were performed utilizing finite element analysis in ANSYS 19.2 (ANSYS, Inc., Canonsburg, PA). The simulations were performed as static structural simulations quantifying the Von-Mises strain in the brain and the electrode to permit comparison to studies [83, 141, 143, 171, 245, 249, 251] and to determine the local strain field that strain activated calcium channels would react to [84, 86]. These simulations were composed of a brain tissue block with a width of 1 mm x depth of 1 mm x and height of 5 mm, and an implanted electrode embedded at the center of the brain block (Figure 6.1). All electrodes in this study were modeled to a length of 3 mm [83, 141, 249, 251].

Simulations were performed with half symmetry models of the electrode and brain block. Two perpendicular symmetric volumes were used to simulate micromotion for Michigan style probes for motion in the X axis and Y axis whereas only one symmetric volume was required for microwires due to their innate radial symmetry. A mesh convergence study was performed to converge the average strain in the brain block to a sub 2% change with the addition of a minimum of 20,000 elements. The elements chosen for this study were 2nd-order tetrahedral elements due to the fine shape conformations required to capture the geometry accurately. Converged meshes utilized in this study had a total element count ranging from 219,118 elements to 1,777,212 elements.

6.2.2 Electrode Geometry

Two general electrode designs were employed in this simulated study, microwire and Michigan style electrodes. Microwire electrodes were simulated as a simple cylinder with a diameter between 8 μm and 88 μm. Michigan-style electrode in contrast were 123 μm wide at the base tapering to a point, and had a thickness between 15 and 100 μm [252] with the exception of the smallest Michigan-style electrode which was modeled as 25μm wide by 2 μm thick of the NanoElectronic Thread (NET) probes [253].

6.2.3 Simulated Motion

To stimulate the micromotion of the brain relative to the fixed electrode in the model a displacement boundary condition was applied such that the to the base of the brain block was fixed while the top of the electrode was displaced (Figure 6.1). For all simulations, a 20μm displacement was applied in either the X, Y, or Z axes. The displacement was selected to be 20μm as it represents an average of the pulsatile brain motion quantified in rats [254] and has been used in prior simulation studies [82].

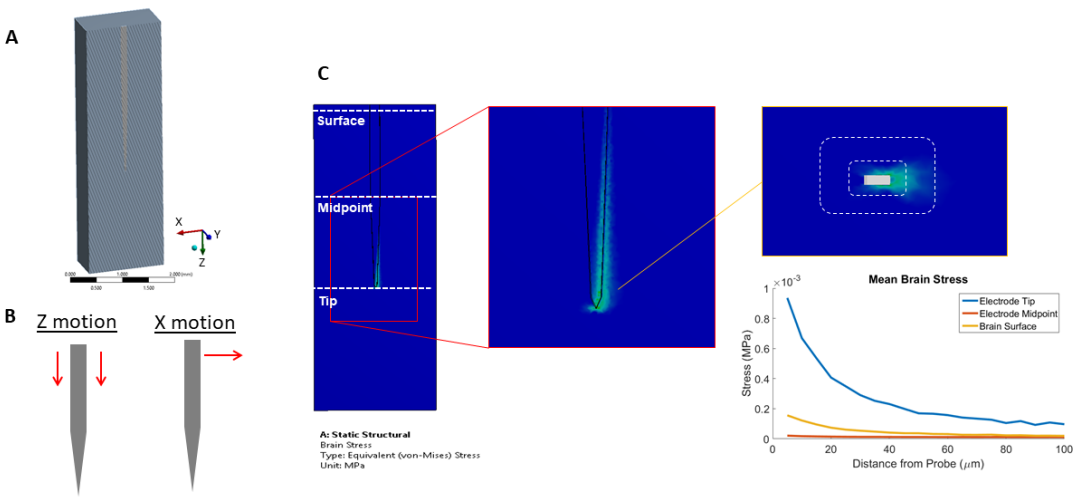

Fig. 6.1. Simulation and Quantification. A) Sample simulation volume (15μm thick Michigan-style probe) with motion boundary conditions, B) Diagrams of the motion applied to the implanted electrodes, C) workflow of data extraction and quantification (Layer selection, volume extraction, concentric binning of values) with example strain curve.

6.2.4 Stress and Strain Quantification

To more accurately quantify the Von-Mises stress and strain states of the brain block from the variety of implanted electrodes, the simulation results were first extracted from the simulated volumes with a custom javascript then analyzed by a custom Matlab script. Due to the non-uniform density of the mesh around the probe, extracted data from the brain and electrode regions was first interpolated into a matrix of data points with uniform density via the scatteredInterpolant function in MATLAB. These data points were then segmented into 100μm bins along the length of the probe followed by radially segmenting the brain into 5μm concentric bins extending 100μm from the surface of the electrode, an observe limit of dendritic damage to neurons [44]. Within each of these regions the mean and maximum stress and strain values for the binned region. The mean and maximal values for the electrode were simply collected for each 100μm segment along the length of the probe. Due to the

large volume data only three layers along the length of the probe are reported in this study, those layers are: the surface of the brain (0 mm deep), midpoint of along the electrodes length (1.5 mm deep), and the tip of the electrode (3 mm deep).

6.2.5 Radial Volume Weighted Means

To calculate a singular mean value for comparisons between brain regions in different simulations a weighted average of the mean strain and stress values for each concentric bin is calculated using the volume of each bin for weighting.

6.2.6 Volumetric Measures

To quantify the extent of the strain on the overall brain block the volume of the brain under strain was measured at different thresholds. To calculate these volumes the mean values for each concentric binned region for each layer of the brain analyzed is compared to a threshold of interest, for bins with a mean strain over the threshold its volume is added to the total volume affected at that threshold. For this study strain thresholds of 3% and 5% have been investigated as researchers have previously observed neurological damage and death can occur at strains of 3-5% [85,86,255,256].

6.2.7 Cotters Analysis

To analyze the contribution of each neural implant design parameter on the total stress and strain induced by electrode motion in the brain sensitivity analyses were performed. For this study the Cotters method for sensitivity analysis [257] was employed due to the low number of trials required to quantify sensitivity (2n+2 for n factors), its adaptive sensitivity threshold based on number of factors, and accuracy relative to other sensitivity analyses (Sobol method, perturbation method, and Latin Hypercubes). The method to this calculation is defined in Cotter, 1979, but in brief the Cotters method calculates the the sensitivity of parameters by evaluating the

upper and lower bounds of the parameters at the limits of the design space. This is accomplished by performing 2n+2 trials for an analysis of n factors generating observations for each (y_1 through y_n). The first trial has all n factors (x_1 through x_n) set low with the following n trials setting one factor high for a trial. The next n trials all factors are set high with a single factor in turn set low, with the last trail having all factors set high (Table 6.1). These observations are then used to define the contrasts C_o and C_e for each factor which describe the effect of varying an individual parameter and the interactions with other parameters respectively.

$$Co(j) = \frac{1}{4}[(y_{(2n+2)} - y_{(j+n+1)}) + (y_{(j+1)} - y_{(1)}))] \tag{6.1}$$

$$Ce(j) = \frac{1}{4}[(y_{(2n+2)} - y_{(j+n+1)}) - (y_{(j+1)} - y_{(1)})] \tag{6.2}$$

The measure M(j) then orders the factors before finally calculating the sensitivity S(j)for each factor.

$$M(j) = |C_o(j)| + |C_e(j)| \tag{6.3}$$

$$S(j) = \frac{M(j)}{\sum_{j=1}^{n} M(j)} \tag{6.4}$$

6.2.8 Analyzed Design Parameters

To perform a Cotter's sensitivity analysis, design parameters for neural implants had to have upper and lower limits as defined from previous studies and implemented devices. For this study, only parameters that have been measured *in vivo* or implemented in a physical neural implant were considered to limit the analysis to currently feasible implants. This study examines several design factors and their interactions including electrodes Youngs modulus, brain's Young's modulus, brain/electrode adhesion [258], and electrode cross-sectional area (Table 6.2). Additionally, this study examines several factors not analyzed in isolation but contribute to the mechanics of electrode stress and strain in the brain including the brain Youngs modulus, electrode shape, and direction of brain motion. The lower and upper bounds for these parameters used in simulations are defined in Table 6.2.

Table 6.1.
Cotters method trial design for analysis of n factors

Trials										
	1	2	3	...	$n+1$	$n+2$	$n+3$	...	$2n+1$	$2n+2$
x_1	Low	High	Low	...	Low	Low	...	...	High	High
x_2	Low	Low	High	...	Low	High	Low	...	High	High
x_3	Low	Low	Low	...	Low	High	High	...	High	High
$\vdots$	$\vdots$	$\vdots$	$\vdots$	$\ddots$	$\vdots$	$\vdots$	$\vdots$	$\ddots$	$\vdots$	$\vdots$
x_n	Low	Low	Low	...	High	High	High	...	Low	High
	y_3	y_3	y_3	$\cdots$	y_{n+1}	y_{n+2}	y_{n+3}	$\cdots$	y_{2n+1}	y_{2n+2}
Observations										

Table 6.2.
Neural implant design parameters investigated in the current study, with lower and upper bounds for each defined.

Property	Lower Bound	Upper Bound	Citations
Brain Young's Modulus	5 kPa	15 kPa	[81, 83]
Electrode Young's Modulus	2.5 GPa (SU-8)	535 GPa (Tungsten)	[144, 259, 260]
Brain to Electrode Attachment	Frictionless	Bonded	[249]
Electrode Cross Sectional Area	$50\mu m^2$	$6150\mu m^2$	[45, 139, 250]
Electrode Shape	Microwire	Michigan Style	
Brain Motion Orientation	X,Y displacement	Z displacement	[143, 171, 249]

6.3 Results

The initial sensitivity analysis examining all factors showed that the most consistently sensitive, and in a majority of cases most sensitive, design parameter influencing the generation of strain in the brain was the relative direction of implanted electrodes micromotion (Figure 6.2). For motion, Z axis loading produces the most strain in the brain in all scenarios with Y motion producing the least. Bonded contact between the brain and electrode produced the most strain as bonded contacts resulted in the larger volume of brain tissue to moving with the electrode, though in contrast, it is frictionless contact scenarios that produced the highest amount of strain in the small volume of brain tissue that was moved. The style of probe produced a moderate effect with Michigan-style probes producing a slight reduction in strain, either due to the non-uniform shape of the probe shank or the sharper electrode tip. Reducing the electrode cross-sectional area caused a reduction in strain. Similarly, Reducing the electrodes young modulus produced less strain in the modeled brain. Finally, Increasing brains stiffness modulus produced a small decrease in strain.

Table 6.3.
Cotters analyses examining parameters combinations for all design factors for the weighted radial mean and volumes of strained tissue above 3% and 5%. Green highlighted cells indicate factors that are sensitive for a given measurement type an region.

Measure	Motion Contrast	Region	Electrode Type	Brain Electrode Attachment	Cross Sectional Area	Brain Stiffness	Electrode Stiffness	Motion
Weighted Radial Mean	Y vs Z	Surface	0.0462	0.154	0.009	0.017	0.161	0.612
		Middle	0.1335	0.172	0.000	0.000	0.018	0.675
		Tip	0.1872	0.236	0.000	0.000	0.007	0.570
	X vs Z	Surface	0.0225	0.158	0.009	0.017	0.165	0.628
		Middle	0.1335	0.172	0.000	0.000	0.018	0.675
		Tip	0.1872	0.236	0.000	0.000	0.007	0.570
Volume at 3% Strain	Y vs Z	Surface	0.0049	0.005	0.000	0.008	0.094	0.888
		Middle	0.0555	0.522	0.000	0.000	0.000	0.422
		Tip	0.3950	0.307	0.000	0.000	0.000	0.298
	X vs Z	Surface	0.0049	0.005	0.000	0.008	0.094	0.888
		Middle	0.0555	0.522	0.000	0.000	0.000	0.422
		Tip	0.3950	0.307	0.000	0.000	0.000	0.298
Volume at 5% Strain	Y vs Z	Surface	0.0000	0.000	0.014	0.000	0.087	0.899
		Middle	0.0000	0.226	0.000	0.000	0.000	0.774
		Tip	0.4098	0.197	0.000	0.000	0.000	0.393
	X vs Z	Surface	0.0000	0.000	0.014	0.000	0.087	0.899
		Middle	0.0000	0.226	0.000	0.000	0.000	0.774
		Tip	0.4098	0.197	0.000	0.000	0.000	0.393

A notable observation aside from the design parameters themselves is their distribution of induced strain. In all cases, the highest amount of strain produced occurs near the tip of the electrode (Appendix Figure 1). Due to the low response from the surface and middle of the probe regions relative to the tip, parameter sweeps and plots focus on just the tip values, though cotter sensitivity analyses are were performed for all regions of the probe.

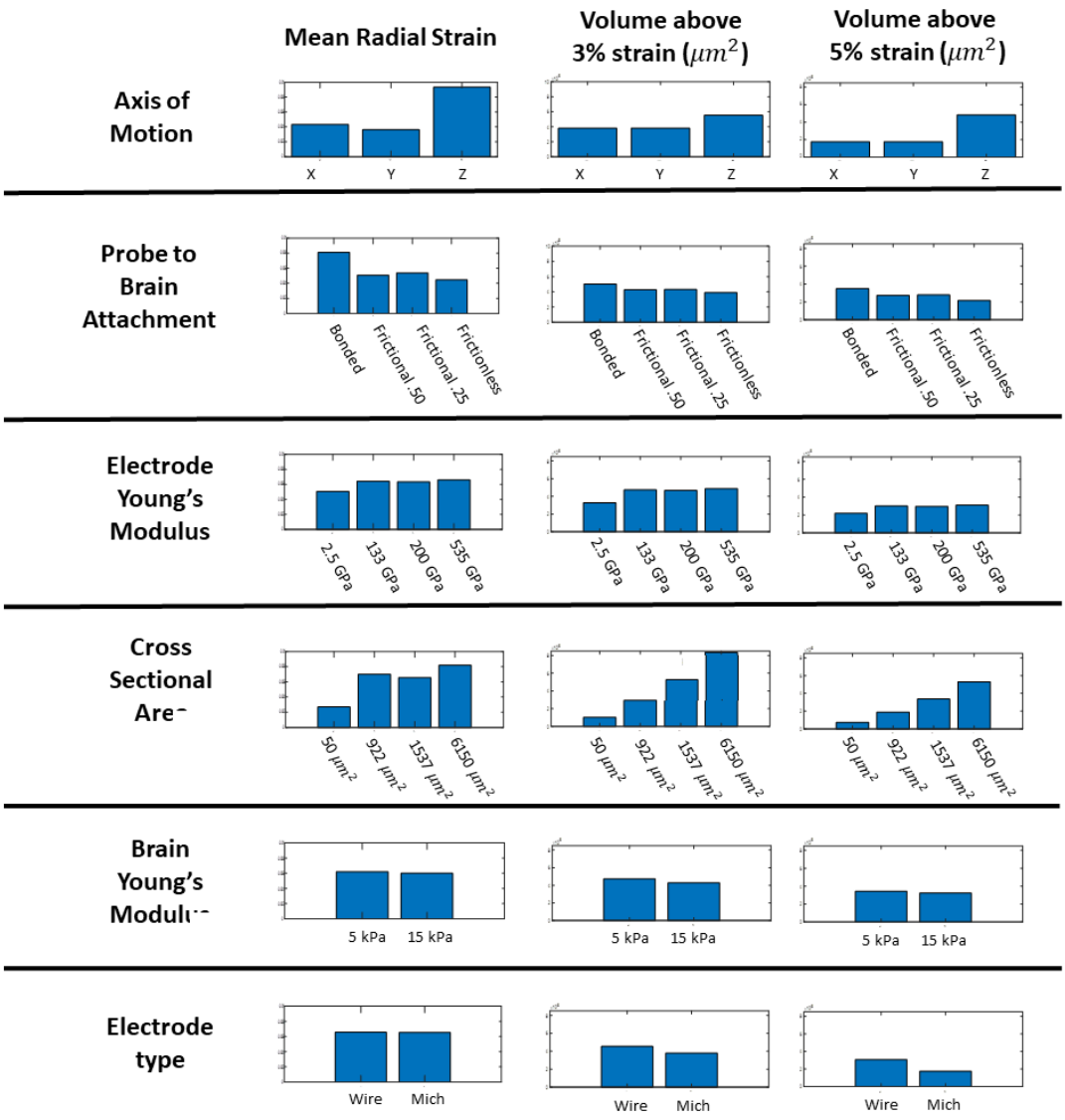

Fig. 6.2. Grouped measures for each design factor examined in this study. Each factor is examined for the weighted radial mean strain, maximum strain, the volume of the brain above 3% strain, the volume of the brain above 5% strain that they produce in the brain and for each region of the electrode (surface, middle, tip). All measures displayed are taken from around the tip of the neural implant. Mean strains displayed range 0 to 0.1 and volumes measured range from 0 of 0.0085 mm3(units in μm^3).

Table 6.4.
Motion Isolated Cotters Analysis. This table displays the sensitivity results for an analysis of the electrode parameters without the axis of motion. Motion instead is being used as a restriction criteria for all analyses. Cases where no parameters were sensitive (all factors 0) are a result of no measure of strain present for regions investigated.

Measure	Axis of Motion	Region	Electrode Type	Cross Sectional Area	Brain Electrode Attachment	Brain Stiffness	Electrode Stiffness
Weighted Radial Mean	Z Axis	Surface	0.339	0.243	0.347	0.044	0.027
		Middle	0.376	0.199	0.403	0.014	0.009
		Tip	0.275	0.184	0.492	0.030	0.019
	Y Axis	Surface	0.171	0.121	0.048	0.061	0.598
		Middle	0.060	0.556	0.165	0.002	0.217
		Tip	0.008	0.693	0.099	0.001	0.200
	X Axis	Surface	0.267	0.203	0.289	0.023	0.218
		Middle	0.284	0.142	0.287	0.006	0.281
		Tip	0.321	0.069	0.281	0.011	0.318
Volume at 3% Strain	Z Axis	Surface	0.308	0.294	0.308	0.032	0.059
		Middle	0.383	0.143	0.474	0.000	0.000
		Tip	0.040	0.604	0.356	0.000	0.000
	Y Axis	Surface	0.044	0.044	0.000	0.075	0.838
		Middle	0.000	0.000	0.000	0.000	0.000
		Tip	0.000	0.707	0.000	0.000	0.293
	X Axis	Surface	0.244	0.233	0.244	0.047	0.231
		Middle	0.297	0.110	0.297	0.000	0.297
		Tip	0.222	0.383	0.173	0.000	0.222
Volume at 5% Strain	Z Axis	Surface	0.299	0.299	0.299	0.053	0.050
		Middle	0.375	0.207	0.375	0.043	0.000
		Tip	0.203	0.422	0.375	0.000	0.000
	Y Axis	Surface	0.000	0.000	0.139	0.000	0.861
		Middle	0.000	0.000	0.000	0.000	0.000
		Tip	0.697	0.101	0.095	0.000	0.107
	X Axis	Surface	0.243	0.243	0.243	0.040	0.232
		Middle	0.282	0.155	0.282	0.000	0.282
		Tip	0.265	0.200	0.245	0.025	0.265

With the direction of motion being the most consistently sensitive parameter secondary sensitivity analysis was performed with motion fixed in different axes to examine how loading the electrode differently would affect the sensitivity of other parameters. From this analysis, several trends regarding which factors are sensitive

under different motion conditions can be observed. Primary to note is that the pattern of sensitivity is not consistent between different loading directions and in general the sensitivity trends are consistent among the different measures of the strain in the brain (radial mean, volume of strained tissue). Those trends show that for moving into the brain (z-axis motion) the style of the probe, cross-sectional area, and attachment of the probe are sensitive. For motion perpendicular to the flat a probe in Michigan style probes (y-axis motion), the cross-sectional area and electrodes Young's modulus are sensitive. Finally for motion along the short edge of the probe (x-axis motion) the electrode type, attachment, young modulus and to a lesser extent cross-sectional area are sensitive.

This sensitivity analysis highlights the impact that loading direction has upon the behavior of strain induced by a probe in the brain. Performing a sweep of electrode stiffness versus cross-sectional in different loading directions this can be seen again. In the Z loading cases changing the electrode stiffness has little impact on the strain, but in the X and Y loaded cases the electrodes young modulus has a considerable influence on the strain.

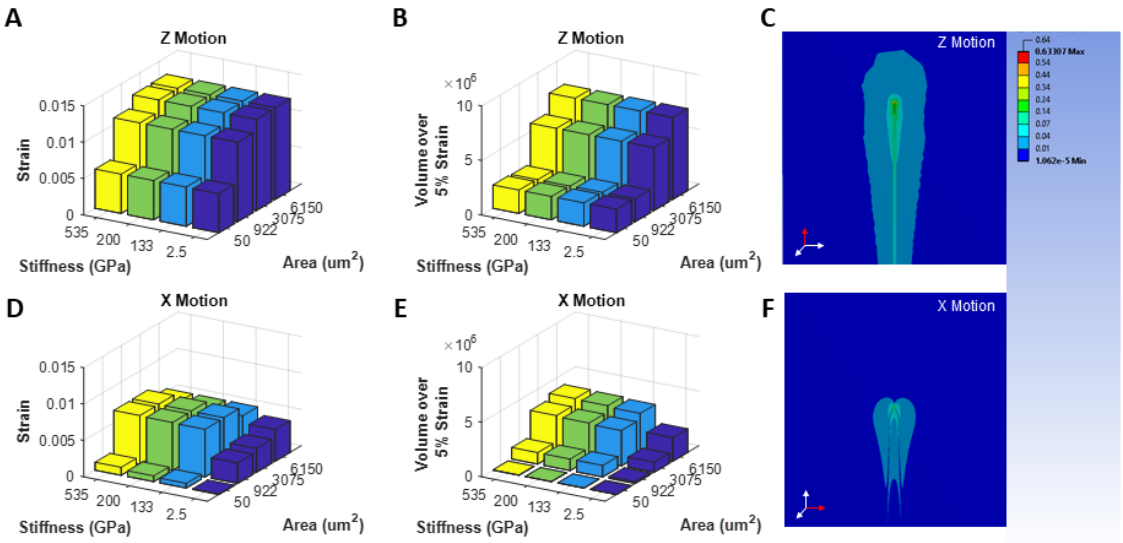

Fig. 6.3. Bonded Michigan-style probe displaced along the Z-axis (A thru C) and X-axis (D thru F). 3D bar plots of average Michigan-style probes, comparing A) the mean weighted radial strain and B) volume of the brain over 5% strain produced by various electrode size and stiffness with motion restricted to the Z-axis(A,B) or X-axis (D,E) . Strain volumes produced by the implanted probe and C) Z-axis and F) X-axis displacement.

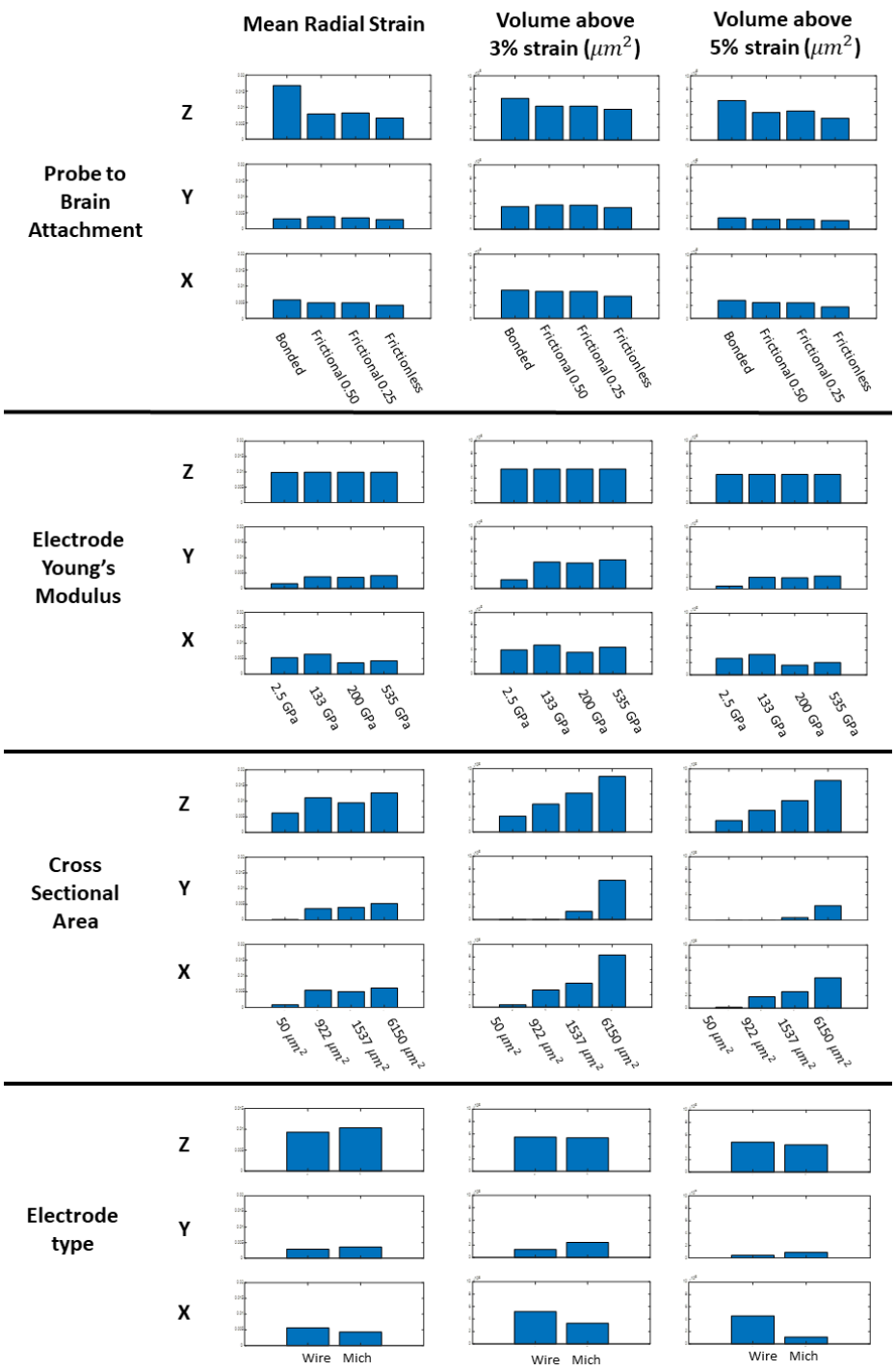

Fig. 6.4. Analysis for each design parameter examined in motion fixed sensitivity analysis. Each parameter is examined for the weighted radial mean strain, volume of the brain above 3% strain, & volume of the brain above 5% strain that they produce in the brain at different loading directions. Mean strains displayed range 0 to 0.2 and volumes measured range from 0 of 0.01 mm^3 (units in μm^3).

Table 6.5.
Attachment Isolated Sensitivity analysis. This table displays the sensitivity results for an analysis of the electrode parameters sans the brain electrode attachment. The attachment between the brain and electrode instead is being used as a restriction criteria for all analyses.

Measure	Brain Electrode Attachment	Region	Type	Area	Brain Stiffness	Electrode Stiffness	Motion
Radial Mean	Bonded	Surface	0.051	0.151	0.017	0.163	0.618
		Middle	0.040	0.263	0.000	0.019	0.678
		Tip	0.009	0.285	0.000	0.008	0.698
	Frictional 0.50	Surface	0.188	0.046	0.093	0.395	0.277
		Middle	0.363	0.383	0.001	0.070	0.184
		Tip	0.033	0.551	0.001	0.018	0.397
	Frictional 0.25	Surface	0.182	0.087	0.090	0.372	0.268
		Middle	0.358	0.379	0.001	0.064	0.198
		Tip	0.039	0.539	0.000	0.016	0.405
	Frictionless	Surface	0.183	0.062	0.091	0.395	0.269
		Middle	0.351	0.387	0.001	0.065	0.197
		Tip	0.058	0.541	0.000	0.018	0.384
Volume at 3% Strain	Bonded	Surface	0.039	0.005	0.008	0.091	0.857
		Middle	0.002	0.499	0.000	0.000	0.499
		Tip	0.000	0.508	0.000	0.000	0.492
	Frictional 0.50	Surface	0.076	0.076	0.131	0.642	0.076
		Middle	0.329	0.329	0.000	0.012	0.329
		Tip	0.000	0.859	0.000	0.000	0.141
	Frictional 0.25	Surface	0.076	0.076	0.131	0.642	0.076
		Middle	0.329	0.329	0.000	0.012	0.329
		Tip	0.000	0.859	0.000	0.000	0.141
	Frictionless	Surface	0.076	0.076	0.131	0.642	0.076
		Middle	0.329	0.329	0.000	0.012	0.329
		Tip	0.000	0.859	0.000	0.000	0.141
Volume at 5% Strain	Bonded	Surface	0.000	0.000	0.000	0.088	0.912
		Middle	0.108	0.201	0.000	0.000	0.691
		Tip	0.000	0.400	0.000	0.000	0.600
	Frictional 0.50	Surface	0.212	0.212	0.000	0.365	0.212
		Middle	0.000	0.000	0.000	0.000	0.000
		Tip	0.175	0.532	0.000	0.000	0.293
	Frictional 0.25	Surface	0.212	0.212	0.000	0.365	0.212
		Middle	0.000	1.000	0.000	0.000	0.000
		Tip	0.054	0.580	0.000	0.000	0.366
	Frictionless	Surface	0.212	0.212	0.000	0.365	0.212
		Middle	0.000	0.000	0.000	0.000	0.000
		Tip	0.243	0.505	0.000	0.000	0.252

The second factor that was most consistently sensitive in the initial sensitivity analysis was the bonding between the brain and electrode. Similar to the secondary analysis performed on the direction of loading a secondary sensitivity analysis is performed with the electrode attachment being isolated. In contrast to the marked patterns of sensitivity related to different loading directions, the different bonding conditions produced consistent sensitivity relationships among examined attachment conditions. Namely, the motion of the probe and the cross-sectional area are the most consistently sensitive, though electrode type and electrode youngs modulus are sensitive at the electrodes middle and surface respectively.

6.4 Discussion

The goal of the current study was to quantify the relationship between the design factors of implanted neural electrodes the degree to which they contribute to the von-Mises strain in the brain, a reported source of neural apoptosis and contributor to the immune response [84, 86], both individually and in relative to other design factors. To this end, this study aimed to examine which design factors contribute to the mechanical strain of neural implants in the brain and how that strain, and by extension, the immune response caused by it, be reduced by better electrode design. In a manner similar to optimizing the execution time of a program where one function could be improved by 90% means very little if it's overall contribution to the problem is only 5% relative to a function that could be improved by 30% but comprises 70% of the problem space. That is why it's crucial to determine which features of electrode design can be optimized and in which order to improve device performance, or what features can be changed without negatively affecting overall performance.

For this study researches quantified the strain of the brain tissue, as prior research found increased strain neuronal tissue has been correlated with an increase in the immune response of around the site of strain and a decrease in the viability and function of neurons in the same area. These responses have been hypothesized to be

due to deformations in cell membranes and activating stretch gated of ion channels [84] causing increased flow of calcium ions through the membrane. This, in turn, causes irregular membrane polarization siphoning ATP from other cellular function to re-stabilize the membrane potential and triggers the up-regulation of endothelin-1 (ET-1) production, a vasoconstrictor [85]. Additionally, Interleukin (IL-36Ra) production increases as does the presence of metalloproteinases MMP-9 both of which result in increased neuron apoptosis further aggravating the damage to local neural networks and propagating the overall immune reaction [86–88]. The continuous mechanical perturbation of the local neuronal tissue in this manner would also lead to the chronic immune response that is observed in most implanted electrodes and explains why after several months implanted the immune response around the electrode does not abate. Studies examining stab wound controls of neural implants, where the implant is implanted and then removed, found that the injured brain tissue returns to prior densities of neurons, astrocytes, and microglia after 1 to 2 months indicating that the active indwelling of the electrode and not the mere injury caused by the electrode is responsible for the chronic immune response [78]. And after the first 2 months, the only elements of the electrode that has not reached homeostasis with the rest of the brain is the mechanical presence of the probe, continually causing strain in the surrounding brain tissue and in all likelihood significantly contributing the chronic immune response. Hence to determine the impact that a neural implant design might have on the brain the strain that said electrode imparts on the tissue was examined in this study both the average strain within a 100 μm radius of the electrode and the volume of the brain tissue above strains of 3% and 5% where neuronal damage occurs [85, 86, 255, 256].

To investigate the strain caused by electrode designs a series of simulations were conducting varying parameters such as electrode cross-sectional area, electrode stiffness, electrode shape, brain stiffness, brain to electrode attachment, and direction of motion. These simulations were performed with electrodes implanted in a brain block and the electrode induced strain in the brain quantified then analyzed via Cotters

sensitivity analyses to determine which factors were most sensitive in reducing. After analyzing the results of this analysis it was observed that the direction of motion was the most consistently sensitive factor for reducing strain in the brain followed by the bonding between the brain and electrode. Performing secondary sensitivity analyses with motion and attachment fixed allowed for the examination of varying electrode design under differing design constraints and showed trends of sensitivity for different design factors. In brief, it was found that the electrode shape, cross-sectional area, and electrode stiffness were sensitive, though to different degrees depending on the orientation of displacement.

In the sensitivity analysis performed all design factors were examined at the same time to determine which if any design factors were sensitive in generating brain strain and from this, the direction of the electrode motion was the most consistently sensitive factor across all measures cases (Figure 6.3). Examining the measures of strain for the axis of motion it is clear that the highest strain is produced when the electrode is moved in the Z-axis, essentially pushing the probe into the brain akin to a needle which agrees with other observations [143, 171, 249]. In the follow up motion fixed sensitivity analysis strain produced by motion in the Z-axis was most consistently sensitive to changes in the type of probe, cross-sectional area, and attachment of the probe to the brain, suggesting that the tip shape of the probe, large contact surface incident to motion, and size of the surface pushing into the brain are the primary factors responsible for strain induced in Z motion. Notably, neither the electrodes or brains Youngs modulus were sensitive, but this too is reasonable considering the electrode even at its softest is orders of magnitude stiffer than the brain and effectively incompressible for the small distance of the micromotion. Motion in the X-axis produced the second highest strain in the brain where the electrode is loaded upon its short edge, in the case of Michigan-style probes, effectively cutting into the brain tissue. In this loading direction, the strain was sensitive to electrode type, attachment, and electrode Youngs modulus. Again this indicates the tip shape or presence of sharp corners has a considerable influence on strain and a large amount of surface

area still exist on the sliding edge between the brain and electrode rationalizes attachments sensitivity, but there is less area on the sliding contact faces than before which is borne out with a reduced sensitivity compared to Z motion. The Young's modulus is sensitive in all instances of loading along the X-axis, unlike the Z axis, suggesting that the electrode is bending but as it is never more sensitive than any other factor it does not dominate any scenario. Finally, the lowest strain is observed when loading along the flat of the probe and shows sensitivity for mainly the size and stiffness of the electrode. This likely arises from the reduced moment of inertia for the electrode along the Y axis relative to the X axis and the lower force required to bend the probe in this orientation.

These findings highlight the significance of loading direction in regards to simulations of electrodes in the brain and to possible in vivo implants that aim to reduce the strain they produce in the brain. Either by design [135], by motion, adaptive features [141], or orientation of implantation implant can be designed to minimize the strain produced by the micromotion in the area of implantation. This raises a concerning limitation with the current state of the literature though, the lack of measured micromotion data in three dimensions for different implantation sites throughout the brain, in particular, the rat brain. At the time of writing only one group has quantified the brain micromotion in rats and then it only quantifies the motion if one axis perpendicular to the surface of the brain and only above the somatosensory cortex [80]. For the generation of more accurate models and to quantify the impact of motion id different regions of the brain micromotion must be measured for each neural implant target sites.

Additionally, when analyzing level sweeps for each parameter in the sensitivity analysis with motion constrained (Figure 6.3) it was observed across all measures that peak strain occurred at the tip of the implanted electrode regardless of loading direction due in part to the direct loading of the tissue right at the tip for all Z loading cases agreeing with prior studies [65]. It is possible that softer probes than examined in this study, with stiffness at the same order of magnitude of the brain,

highly bonded with the brain would result in strain more distributed along the length of the probe due to bucking or if there is another combination of parameters that would result in strain distributed along the length of the probe.

The second most consistently sensitive design factor was the bonding between the brain and the electrode. Initial measures of the brain to electrode bonding showed that increasing bonding yielded increased mean strain and strain brain volume, agreeing with prior research [171]. To investigate if this factor interacts with other factors, similar to the directionality of motion, a sensitivity analysis fixing the bonding condition was performed. This yielded a consistent pattern of sensitivity from the other factors across all bonding conditions, those being high sensitivity to motion, electrode cross-sectional area, and to a lesser extent sensitivity to electrode stiffness and type at the surface and mid-point of the probe respectively. The consistent trends in sensitivity across different bonding conditions indicate that the different degrees of bonding simply affect the magnitude of the strain and there exist no unique interactions for any given level of bonding. It was observed that higher levels of bonding between the electrode and the brain produce lower peak strain (Supplemental Materials) but increases average radial strain and volumes of the brain strained above 3% & 5% agreeing with prior studies investigation electrode bonding [143, 249]. The increases in average strain and brain volume strained as friction/bonding increase is due to the increasing volume of the brain adhering to the probe as it moves. Inversely increasing bonding will lower the peak strain due to the force of the probe in the brain is distributed over a large volume. These findings suggest that to reduce strain electrodes should be designed to exhibit low friction with the brain. But aside from materials that would inhibit glial attachment or protein coatings that modulate the bonding of neuronal cells, the bonding is a boundary condition that should be better defined.

6.4.1 Undefined Boundary Conditions

While the direction of micromotion and degree of bonding between the brain and electrode have been found to be highly sensitive factors in modulating the strain they are boundary conditions for implanted electrodes and not features of the probe that can be changed but rather features of the implanted brain environment. At the time of publication, there exists only one study by Gilletti & Muthuswamy investigating the micromotion at the surface of the brain [80]. While this study does provide insight to the brains motion at rest and correlate brain motion with other physiological events (breathing & heart rate) it only investigated motion perpendicular to the surface of the brain at the surface of the brain in one spot of the cortex (Figure 6.5). This regretfully limits the applicability of the measured micromotion in several critical ways, the first of which is the dimensionality of the motion measured. Gilletti & Muthuswamy measured brain motion via a linear variable displacement transducer (LVDT) which can only measure along on dimension and while this may be suitable for quantifying the dilation of the brain it is unable to quantify the brain motion in three dimensions. Due to the possible sources of brain motion, vascular dilation, ventricle flow, and gross brain motion relative to the skull it is unlikely that the motion of the brain will be perpendicular to the cortical surface all over the brain and throughout the volume of the brain. Additionally, the motion was only defined at 3 mm ML, -1.5 mm AP a the cortical surface over the somatosensory region of the brain. While this is a prime implantation site for a wide range of neural implants that targeting sensation in the rat model it limits the application of observed micromotion to other implantation sites throughout the brain or deep regions of the brain. Finally, measures were taken from an open craniotomy during surgery which may have confounded measures due to brain swelling. The limitations of the existing literature coupled with the sensitivity of the strain to changes in micromotion direction highlight the need to accurately define brain micromotion in three dimensions throughout the brain to produce a valid simulation of electrode-induced strain.

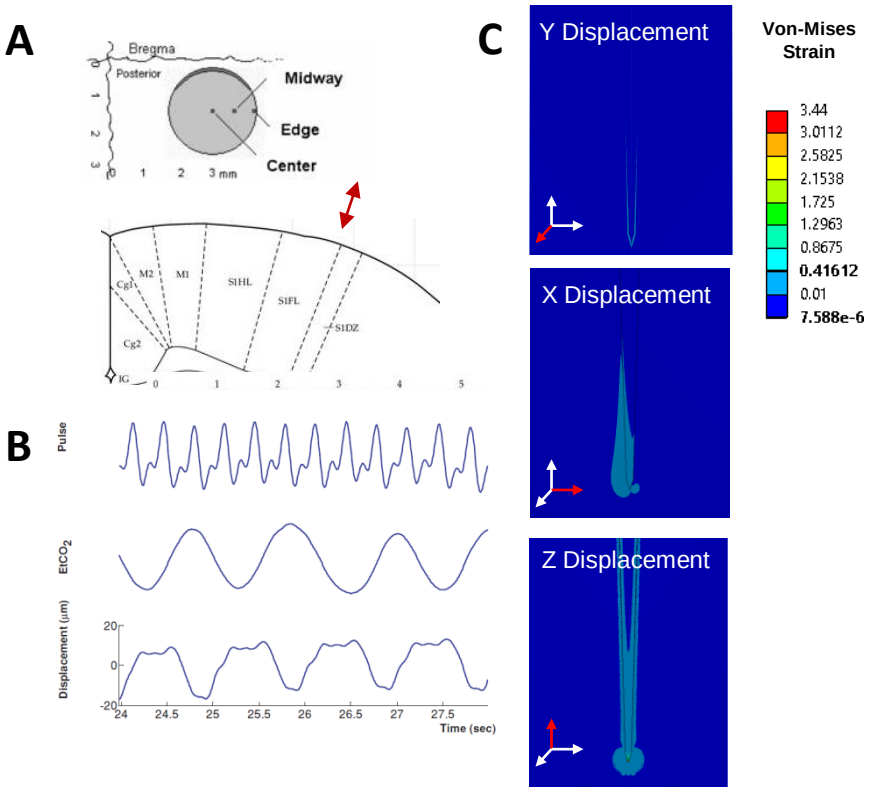

Fig. 6.5. Review of previously obtained micromotion measures. A) Location of brain motion measurement adapted from Gilletti & Muthuswamy [254], B) Coronal view of motion previously measured with red arrow indicating general location and orientation, C) Measures of brain motion over time adapted from Gilletti & Muthuswamy [254], D) Sample strain measurement from an implanted Frictionless Michigan-style probe loaded in three directions displaying the different strain profiles produced for each loading direction.

Similarly, there is a lack of well defined in vivo measures of bonding strength between the rat brain and electrode. Existing simulation studies have used bonding conditions from ranging from frictionless to fully bonded and varied levels of frictional contact in between but all bonding conditions were selected arbitrarily to explore the possible impact of varying bonding rather than correlated with in vivo measures [261]. From numerous implantation studies though that explant electrodes for imaging

or studies that quantified neuronal cells adhering to explanted electrodes [61, 64] demonstrate that there is a strong bonding between the brain and the neural implant. This suggests the brain may be fully bonded to the brain, but because implants are not completely coated when explanted and some probes remove little to no cells when removed it is likely the bonding between the brain and the electrode more nuanced than a simple bonded or frictional attachment. This highlights the importance of accurately defining the bonding between electrodes of different materials and designs with and the brain.

6.4.2 Size vs. Stiffness

One of the aims of this study was to determine which electrode design factors could be modified to reduce strain in the brain. Previous research has focused heavily on the mechanical stiffness of neural implants to reduce strain in the brain and while this is true the materials have to be softened by order of magnitude to obtain a 40% reduction is strain [83]. This begs the question, is this the most effective method of altering the electrode design to improve mechanical biocompatibility, reducing electrode size or stiffness?

Analyzing sensitive factors other than loading direction and brain electrode bonding, it is apparent from parameter sweeps that softer smaller probes reduced strain in the brain, agreeing with previous research [262]. But with unlike prior studies that just described the trends for each factor on in isolation, we are able to compare the relative impact each factor would have in reducing strain. Averaging over all fixed directions of motion and measures electrode size has a slightly average sensitivity than stiffness 0.234 vs 0.208 (Table 6.4) and averaging over different bonding levels again size was consistently more sensitive than electrode stiffness, 0.342 vs 0.134 (Table 6.5). Though it should be noted that this is an extreme simplification of the sensitives for each case which describe how each factor for a given set of boundaries conditions would influence brain strain but does give a general trend. Examining

individual cases, such as the one illustrated in Figure 6.3 where the different loading directions are being investigated for a bonded Michigan-style probe, it's can be seen the decreasing the size of the electrode has a more substantial reduction in strain earlier than electrode stiffness. These results show that size plays a larger role in reducing strain in the brain compared to stiffness, which agrees with prior in vivo studies that found reducing electrode stiffness resulted in little to no significant decrease in immune response [263]. In contrast in vivo studies with testing electrode size been showed that decreased electrode size produced significant improvements in chronic device function [138]. This is further supported by recently developed ultra-small neural implants with cross-sectional areas below 50 μm^2 that have produced little to no immune response from the surrounding tissue and demonstrate chronic stability [45, 139], whereas larger probes made of increasingly softer and mechanically compliant materials invoke a chronic immune response [264].

6.4.3 Design Space Exploration

With relationships between design factors defined, at least initially by this study, optimizations on their properties individually or collectively can be performed to optimize designs and reduce the strain produced by these electrodes. This approach to optimization, unlike previous approaches, leverages the sensitivity of a given design factor against others so that when optimizing a factor the relative reduction of strain is known. This allows researchers to understand where a bottleneck in a current design exists and where improvement for a single design factor would produce the greatest reduction of strain. Additionally, the relative sensitivities for boundary conditions such as micromotion direction, brain to electrode bonding, and position along the electrode shaft allow researchers to investigate scenarios where those boundary conditions are changed and leveraged for improved electrode design. For example, the sinusoidal neural implant developed by Sohal et al. [265] demonstrates low mechanical strain likely due in large part to its ability to utilize more loading in the X and Y

axis rather than just the Z axis of the probe shank when loading in the Z direction. Utilizing the findings made by this study a design that would possibly reduce strain even further would be a helical probe so the compressive forces would be minimized in all three axes rather than just two.

Basic understanding of designs factors that contribute to strain reduction in given scenario electrodes can be designed to optimize those factors and we can explore optimized designs and better explore the design space that produces reduced responses. Though these results are only initial they indicate that large implants can be designed as long as they are created with softer materials, thus allowing larger contact sites for electrical recording or stimulation. Though this highlights the need for further simulation analysis of various electrode designs to optimize charge parameters while creating a device that will function long term implanted.

By understanding the mechanical limits of an electrode design that function chronically researchers can explore ramifications and design space available in other regards of the electrode, such as electrical stimulation, recording, fiber optic compatibility, microfluidic channels, and so on [140]. For example the size of the electrode may dictate how large the contact site for an electrode can be and by extension the electrical stimulation, best performance when stimulating over a large contact area, or recording, local field is best with large contact sites but individual recordings are better with small sites, capabilities available within the current design. Similar to other studies which aimed to optimize the mechanical resilience of deep brain stimulator design through simulation and fabrication studies performed [266].

6.4.4 Limitations

Due to the complexity of electrode design and possible confounds of different factors, not all design variations could be examined, one such aspect was that of the electrode shape. Since the probe designs change multiple aspects at once, i.e. tip shape, edges, tapering, cross section, aspect ratio, a more granular investigation

could inform more about the features of the design that reduce strain in simulations. For this reason, a discussion regarding electrode shape was avoided in this current study and g This is highlighted by the direction of motion and region where the greatest difference between microwire probes and Michigan-style probes occurred, at the electrode tip in Z motion displacements, the scenario where tip shape would have the largest impact on results. Thus examinations focusing on tip shape (pointed vs rounded/beveled vs flat) be done separately from analyzes of edge effects (rounded vs squared), aspect ratio (low vs high), and electrode tapering (tapered vs straight).

A limit of the current study due in part to lack of three-dimensional micromotion data and in an effort to analyses simple, the motion was only applied to electrodes on orthogonal axes. While this allows for investigation on how each axis contributes to the strain produced in the brain it doesn't give much insight into how these individual axes add together in motions beyond one dimension, such as would be expected in vivo. In general, motion needs to be better defined and investigated in combinations of directions rather than just along orthogonal axes.

6.5 Conclusions

In this study, we were able to demonstrate a methodology to examine multiple electrode design factors at once and quantify their ability to reduce strain in the brain they are relative to each other factor. This allows for the investigation and optimization of electrode design through simulations in a methodical approach that efficiently explores the design space. This is an improvement over previous approaches to electrode design that focused on individual parameters optimization and comparative analyses prone to confound.

In analyzing the design factors that contribute to the electrode induced strain, the most sensitive feature is the motion of the probe, which direction the probe moves in relation to the brain and by extension the orientation that probe was inserted into the brain. The maximal strain is observed when the probe pierces into the brain

(Z motion), in contrast, the lowest strain occurs when loading along the flat of the probe (Y motion). Regretfully the brain micromotion is currently ill-defined for three dimensions and different regions of the brain highlighting the need for further investigation to quantify micromotion of the brain. Bonding between the electrode and the brain was the second most sensitive design factor with frictionless contact producing lower strain in the brain relative to fully bonded contact. Though higher peak strains were observed immediately vicinity of frictionless bonded probes. Bonding like micromotion also lacks in vivo metrics that define the bonding between the two again highlighting the need for boundary conditions of the brain electrode environment to be defined. Following bonding, the next most sensitive factor is the size of the electrode for a majority of scenarios, with reduced electrode size causing decreased strain.

Here we have shown relationships between electrode design factors and their contribution to strain generation. This shows that electrode designs can be explored through simulation and sensitivity analysis enhancing how the design space for electrodes for optimization for chronic function.

7. QUANTIFICATION OF BRAIN MICROMOTION IN RATS

Material found in this chapter is currently in preparation for publication in a journal publication

7.1 Abstract

At current, the motion of the brain relative to the skull for a wide variety of animals is unknown. This limits the research investigating the mechanical forces of the brain and surrounding tissues on implanted devices and the accuracy of finite element models investigate the resting brain. This study investigates the micromotion of the rat brain, using a novel microCT based imaging method where implanted radiopaque microbeads are imaged via microCT providing high-resolution three-dimensional measures of brain motion at various locations within the brain both at the surface and deep brain regions. This initial study has observed micromotion ranging from 20 μm to 50 μm with increased motion along the medial/lateral axis.

7.2 Introduction

Neural implants are a novel interface bridging the nervous system with computers with the aim of treating a wide variety of otherwise difficult to treat or untreatable disorder. While researchers have demonstrated the viability of treating disorders with neural stimulation, they are regretfully limited due to a chronic immune response which causes implanted devices to fail over time [52, 68]. While a number of approaches to reduce the severity of the immune response have been examined recent research in ultrasmall neural implants, devices with cross-sectional areas less than

50 μm^2 have shown stable performance in vivo [45, 139]. This demonstrated that electrode design plays a significant contribution to the chronic immune response yet the precise mechanisms underlying the success of these devices and the design space available for chronically functioning devices is unknown.

It has been observed that reducing electrode size and stiffness result in a smaller immune response [133, 138, 267–269]. Based on results like this it has been proposed that a reduction on the stain produced by micromotion of the implanted electrode relative to the brain tissue can result in a reduction in the chronic immune response and improve device performance, by reducing device size and stiffness. This is further supported by the time course of the immune response where the initial injury is likely responsible for the initial period post-implantation which shares a time course with stab wounds but augmented by a chronic component after a month [42, 59, 62, 78]. This, in addition, to stretch-activated ion Ca^{2+} channels that result in neural apoptosis and inflammation support the hypothesis that mechanical perturbations from neural electrodes contribute to the chronic immune response.

To investigate the variety of electrode design properties and how they contribute to strain several research groups have performed simulation studies of electrodes implanted electrodes. Simulating varied conditions such as electrode size [141], electrode stiffness [81–83, 270], bonding to the brain [171, 258, 271], and shape [143] researchers have been able to investigate the relationships between electrode design and function, even validating results in vivo [82]. While these studies have offered insights on how to reduce the immune response they have all relied upon a single study performed by Gilletti & Muthuswamy to define micromotion they all utilize as a boundary condition in their simulations [80]. In their study, they measured the cyclic micromotion of the brain with a linear variable differential transformer finding a micromotion of approximately 10-30 μm at a frequency of 1-2 Hz matching measured respiratory rate and 2-4 μm at a frequency of 4-7 Hz matching the observed heart rate.

Recent research into this relative influence of design factors on the strain produced in the brain found that the motion of the electrode relative to the brain was the most

influential factor in determining stain produced (Chapter 6). For example, loading along the length of the electrode produced this highest strain in the brain by an order of magnitude. It was also observed that the direction of loading had a large effect on the relative sensitivity of how other design factors such as device size and stiffness contributed to strain. This highlights the need for accurate measures of micromotion in the brain.

Regretfully, the work by Gilletti & Muthuswamy while seminal only defines brain micromotion in a single location and in a single direction [80]. While the brain location selected in their study the primary somatosensory cortex is a prime target for neural implants it's unknown if the brain motion recorded in that location extends to other regions of the brain or not. Additionally, the brain motion from Gilletti & Muthuswamy was only measured at the surface of the brain with the dura mater intact and removed limiting the motion measures to the surface of the brain and not the underlying cortical tissue limiting the accuracy of models outside of the surface region of the somatosensory cortex.

A second limitation of the original study was the use of a linear variable differential transformer (LVDT) to measure the brain motion, while it provided highly accurate measures of the brain it only quantified the brain motion in one direction, perpendicular to the brain surface. As was observed previously, the direction of motion is a significant factor in determining the strain produced in the brain and knowing only one axis of motion greatly limits the simulations other than those examining motion perpendicular to the cortical surface. Finally, the micromotion measurements were performed during a surgical procedure with the skull and dura removed, rather than a resting state for the animal. Due to the craniectomy performed the measures obtained may be confounded with the injury response due to brain swell and a lack of cranial pressure leading to increased motion in the direction of least resistance, in this case, perpendicular to the brain surface and reduced motion in axis limited by tissue catching on edges of the craniectomy.

To investigate the observations originally made by Gilletti & Murthuswamy and determine if the extend to different regions of the brain and in different axis of motion this study aims to develop a novel imaging methodology in which radiopaque microbeads are implanted into the brain and then imaged post-implantation to measure the brain micromotion in rats at rest in three dimensions. To avoid possible confounds associated with measuring the brain during surgery or in an irregular state the micromotion will be quantified without any open wounds, trans-cranial devices, or structural changes aside from those experienced during implantation of the microbeads, a similar surgery to that of a common microwire neural electrode implantation. Finally, different locations of the brain will be examined and brain micromotion compared across regions to determine trends in motion and possible physical phenomenon responsible for the observed motion. In developing a methodology to measure brain micromotion and quantifying the motion in resting rat brain this study will establish a technique for measuring brain micromotion in a variety of animals thus provide a valuable method of measuring soft tissue motion in vivo and define necessary boundary conditions for accurate simulations of the brain.

7.3 Methods

7.3.1 Animals

Sprague Dawley rats (Envigro, New Jersey) were selected for this study as they are a common animal subject for current neural implantation studies, hence quantifying the brain micromotion in Sprague Dawley would apply to a great number of studies already performed and likely future studies aiming to simulate the brain electrode interface. Additionally, female rats were selected for this study to maintain low body weight and small size necessary for the imaging performed in this study.

7.3.2 Motion Quantification

To quantify the amount of micromotion in the resting rat brain a novel technique to quantify 3-dimensional motion was implemented. In brief, radiopaque microbeads were implanted in the brains of rats along tracks that traversed several brain regions relevant to neural stimulation studies. At time points of 1, 2, and 4 weeks post-implantation the animals brains were imaged via microCT scanner at high spatial resolution (4.5 μm). This approach bears some similarity to previous studies that have imaged 800μm tantalum beads glued into the bone at static time points but rather than quantifying the displacement between two strain loads the motion of the brain is quantified while it is in constant motion.

The motion of the microbeads in this study is obtained by measuring the volume of the microbeads imaged during in vivo sessions and after sacrificing the animal subject. By imaging, the microbeads during live imaging sessions distorted volumes of the microbeads in motion can be obtained and these distorted volumes can be used to calculate the motion of the sample [272]. Radiologists have sought shorter 'fast' exposure times for spiral scanned slices to obtain more accurate geometry for imaged objects in motion such as tumors [273, 274],

but by imaging slowly a distorted volume that only captures the volume scanning field constantly occupied by the microbead can be obtained (Figure 7.1). This paired with knowledge of the bead's true diameter, d_{True}, either from pre-implantation measured bead geometry or stationary images (sacrificed animal with no motion) subtracted by the bead's diameter in a given axis during motion, d_{Scan}, describes the volume and diameter of the microbead that was not observed during live imaging and by extension, the amount the bead moved (Equations 7.1-7.3). Through this method the micromotion of the microbead, and by extension the brain tissue the bead is embedded in can be quantified in three dimensions with an upper limit equal to the diameter of the radiopaque bead.

$$M_X = d_{True_X} - d_{Scan_X} \tag{7.1}$$

$$M_Y = d_{True_Y} - d_{Scan_Y} \tag{7.2}$$

$$M_Z = d_{True_Z} - d_{Scan_Z} \tag{7.3}$$

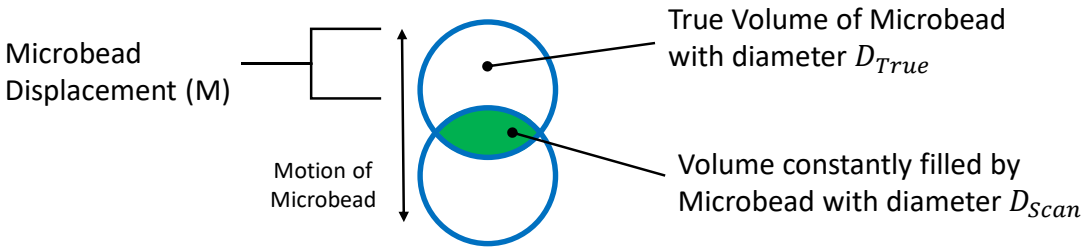

Fig. 7.1. Overview of methodology to measure micromotion from a time lapsed volumetric reconstruction of microCT scan.

7.3.3 Radiopaque Beads

LUMI radiopaque beads designed for angiographic procedures and embolism procedures in the circulatory system were chosen for this study due to their tested biocompatibility, ease of implantation, and stable radiopaque nature [275]. LUMI radiopaque beads are comprised of polyvinyl alcohol 2-acrylamido-2-methylpropanesulfonate sodium salt (PVA-AMPS) microbeads embedded with iodine which provides stable radiopacity. Micro-CT analysis of DC Bead LUMI shows them to possess an inherent radiopacity due to the triiodobenzyl moieties attached to the bead structure [276–278], giving rise to a baseline radiopacity of 4454 225 Hounsfield units (HU) [279]. At the time of publishing, LUMI microbeads were the only commercially available, uniformly sized, radiopaque microbeads that have been tested in live animal models for tracking non-vascular targets [280]. Other radiopaque materials & beads were tested, such as stainless steel microbeads, but did not suspend well enough to permit controlled injection into the brain. Silver coated poly(methyl methacrylate) (PMMA) microbeads

(Cospheric LLC. Goleta, California) were also examined as a possible candidate as a radiopaque marker due to their similar density to LUMI microbeads (1.44 g/ml vs 1.45 g/ml), the biocompatibility of silver [281], and the high Hounsfield value of 17,000 for silver [231]. They were discarded after tests in cadaver animals when it was observed they provided poor radiopaque contrast, either due to the composition of the microbeads or the thinness of the silver (only 250 nm thick).

7.3.4 Injection Vehicle

Due to the density of the LUMI microbeads used in this study (1.45 g/ml) an injection vehicle denser than saline had to be selected to allow the microbeads to exist as a suspension during injection for controlled deposition at target sites. Several options were considered including agarose, high-density x-ray contrast agents, and fructose. To evaluate each injection vehicle 200 μl Eppendorf tubes were filled with 100 μL of the solution to be tested and 20 μL of LUMI microbeads. The Eppendorf tubes were then agitated until the microbeads were completely suspended in the solution, after which the tubes were positioned vertical and monitored. Suspension time was considered the time from agitation to when no microbeads were observed in the upper 110 μL of the Eppendorf tube. At this point, the microbeads have fallen out of suspension to a degree that injections performed cannot have a predicted density of microbeads.

Agarose gel produced inconsistent density at a concentration ranging from 0.05% to 1% to producing short suspension times less than 5 minutes. At concentrations higher than 1% the gel solidified making unsuitable as an injection vehicle. X-ray contrast agents were also considered but discarded as they would produce a non-uniform response from the implanted microbeads over time as the contrast agent would bind the microbeads during injection and either broke down or wash off during the month-long implantation window causing a shifting intensity response over time. Finally, fructose was examined as an injection vehicle. After examining several fructose and

phosphate buffer solution (PBS) solutions ranging from 20% Fructose and 80% PBS up to 100% fructose, it was found that a solution of 80% fructose and 20% PBS solution with a density of 1.54 g/ml created a microbead suspension lasting over 10 minutes, suitable for surgical application. While fructose is not a traditional injection vehicle it is a safe substance for use in the brain as sugars in high concentration have been previously found as effective insertion materials [282] and the brain has been found to metabolize fructose directly via GLUT15 channels [283].

7.3.5 Microbead Concentration

To provide a suitable contrast between microbead implanted in the brain a small but fixed number of microbeads need to be implanted at each site along the implantation tracks. To determine the correct ratio of microbeads to injection vehicle several tests of varying microbead concentrations in the 80% fructose insertion vehicle were tested add different injection volumes. After preliminary testing, it was found that a concentration of 5 μL of LUMI microbead suspension in 200 μL of 80% fructose solution injected with a volume of 10-15 μL resulting in the injection of 1 to 5 microbeads per site.

7.3.6 Micromotion Measure Validation

To measure the accuracy of the reconstructed volume measure of microbead measure, a microbead drop test was performed. Initial video recordings of the microbeads descending in a suspension of 80% fructose were taken to quantify the beads motion over time. It was observed the beads moved at a rate of approximately 1.22 μm/s. The rate of descent along with the fixed scan times of the microCT (18 seconds, 2 minutes, and 4 minutes) was used to quantify the motion of microbeads during decent in one dimension. To quantify the accuracy of the 3D reconstruction method of micromotion measurement, 5 μl of microbeads were suspended in an Eppendorf tube with 400 μL of 80% fructose. The tube containing the microbeads was agitated until

the suspension was achieved then loaded into the Quantum GX microCT scanner. Two lengths of scans were taken 18 seconds and 2 minutes at a field of reconstructions of 5 mm x 5 mm x 5 mm and 10 mm x 10 mm x 10 mm. Micromotion was measured as per the methodology described previously and compared to the

7.3.7 Surgery

For surgeries animals were anesthetized using inhaled isoflurane or injected ketamine/dexdomitor as the anesthetic. Following anesthesia, a midline incision was made on the head to expose the skull and the periosteum was removed. After locating Bregma two craniectomies, each 1 mm in diameter, were made, one over the visual cortex at A/P -6 mm, M/L -3.5 mm and one over motor cortex at A/P -3.12 mm, M/L +2.2 mm. These sites were selected due to their use in cortical neural implantation research and because vertical tracks from them can be made down to the auditory thalamus 6 mm deep and the ventral lateral nucleus 7 mm respectively providing measures of micromotion at the surface and deep sites that pass near branching vascular structures and ventricles.

A suspension of 5 μL of LUMI microbead in 400 μL of 80% fructose suspension prepared prior to the the surgery and sterilized by filtration through a 0.22 micrometer filter for the fructose solution and steam sterilized for the LUMI microbeads was agitated in Eppendorf tube to ensure proper bead suspension in injection vehicle before loading into a 1 mL syringe with a 25 gauge needle. The loaded syringe was then mounted to a Micro4 controlled injection system (World Precision Instruments, Sarasota, FL) and primed by pumping the system until a droplet was observed at the needle tip. Needles were inserted into the brain to a depth of 6 and 7 mm at the visual cortex and motor cortex sites respectively. While withdrawing the needle, 10-20 μL volumes of microbead/fructose mixture were injected into the brain every 500 μm along the insertion track to provide a clear delineation between microbeads along the length of the track. Once the microbeads were injected and the needle

removed, the craniectomies were covered with kwik-sil (World Precision Instruments, Sarasota, FL) and the original incision sutured. Post surgery antibiotic ointment was applied to the suture and mL/Kg of Meloxicam was injected for pain mitigation.

7.3.8 MicroCT Scanning

To observe the resting brain motion of the rat post microbead implantation and quantify the amount of motion of the resting rat brain, animals were imaged via microCT. For this study, a high-resolution Quantum GX microCT scanner (Perkin Elmer, Waltham, MA) was used to perform in vivo animal scans. The scanner was selected for due to the high-resolution volume reconstructions it was capable of (4.5 μm^3 voxels), short scanning duration (18 seconds to 4 minutes for standard resolution and high resolution scans respectively), and low radiation exposure levels suitable for longitudinal studies.

To observe if any changes in brain micromotion correlated with the post-implantation wound healing process, the implanted microbeads were imaged at three-time points post-surgery: 1-week post surgery, 2 weeks post surgery and 4 weeks post surgery. The first imaging session at 1 week aimed to capture the micromotion of the brain during the early wound healing process, but after the bead has had an opportunity to embed into the cerebral tissue. Scanning was delayed a week to allow microbeads to settle into the brain tissue as if scans were taken immediately post-implantation observed microbead motion could be confounded by motion caused by bleeding, swelling of the brain, and sliding along the insertion track, in short forces could be acting directly on the microbeads rather than the tissue that the microbeads are adhering to. While there is value in quantifying this motion without a strong attachment to the nervous tissue any motion or lack thereof would be confounded by the beads still settling into the tissue rather than the motion of the tissue. The second time point, 2 weeks post-implantation was selected to observe the micromotion after a majority of the initial assault had healed but before the immune response enters the chronic stage. It is dur-

ing this period where most electrodes exhibit strong performance and any variations in micromotion relative to the other time points might insights to the biomechanics underlying device function and failure. The final time point is 4 weeks post surgery, at which point the initial injury from the microbead implantation will be healed and the remaining response will be primarily from the chronic immune response [42, 59]. Quantifying this micromotion will be instrumental in developing models that analyze the tissue mechanics and stresses imparted by chronically implanted electrodes on surrounding neural tissue.

Each scanning session began with anesthetizing the rat to be imaged via isoflurane (knockdown at 4% and maintained at 1.8%) and once the animal displayed no self-righting response it was loaded into a custom rat head holder/bed for insertion into the microCT scanner. Two imaging sequences were performed: the first a pair of 2D orthogonal scans taken at 30 frames per second for 60 seconds and the second a 3D volumetric scan with a field of reconstruction of 10 or 5 mm. For both scans, the microCT used a voltage of 90 kV and a current of 88 μA to provide maximal signal intensity and contrast available for the Quantum GX scanner.

7.3.9 Custom microCT Rat Head Holder

In order to stabilize the rats head during scanning and reduce gross motion artifact from the head, motion rats were stabilized in a microCT compatible head holder. Taking inspiration from other CT compatible rat holders such as the device developed by Sharma et al. for housing the animals body, and the Narishge SGP-3 head holder for rats a custom 3D printable rat holder was designed and fabricated for this study [278]. The material selected for printing the head holder was PLA due to its low radiopacity, approximately 260 HU [284], adequate strength for stabilizing an anesthetized rat and ease to prototype designs with. For this application every component of the head holder had to be constructed from low radiodensity materials even the ear bars and the entire device had to fit within a 60 mm diameter cylinder, the

size of the scanning bore of the Quantum GX microCT scanner. The rat head holder was designed in Creo Parametric version 2.0 (Figure 7.2), prepared for printing using CURA 3.6 (Ultimaker, Cambridge, MA) and printed on a Monoprice Delta Mini 3D printer (Monoprice, Rancho Cucamonga, CA). After initial testing with cadaver animals the rat head holder was revised to better accommodate rats with longer and wider heads, ear bars were rounded for ease of use with multiple lengths fabricated to allow for fixing a range of rat head sizes while still fitting within the 60 mm diameter volume, and air channels were added to the nose cone to permit isoflurane to be administered during imaging.

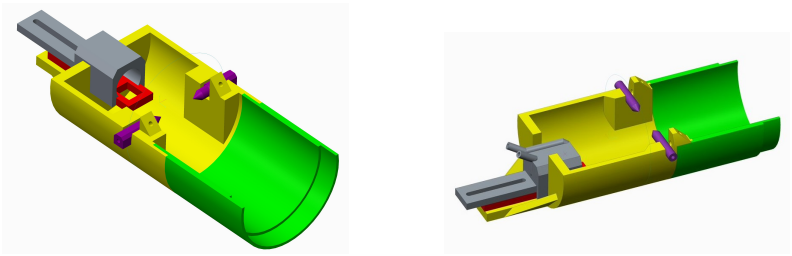

(a) Prototype Head Holder (b) Finalized Head Holder

Fig. 7.2. 3D CAD design of custom microCT rat head holder. a) initial design of head holder, b) final design of head holder. Parts are color coded as follows: bite bar (red), nose cone (grey), head holder body (yellow), ear bars (purple), bed extensions (green).

7.4 Results

7.4.1 Injection Vehicle Testing

In order to image radiopaque LUMI microbeads in the brain a set concentration had to injected throughout the brain, to achieve this a suspension of microbeads (density of 1.45 g/mL) had to be stable for at least 10 minutes, the approximate duration of the injection procedure for each 6 - 7 mm long track. Several different injection vehicles were evaluated including saline, PBS, Agarose (0.05% to 1%) and

a fructose/PBS solution (20/80 ratio to 100/0 ratio). Saline and PBS only provided a suspension for a few seconds, which permitted for transferring of microbeads while suspended but was unsuitable for injections. Agarose, in contrast, created solid gels at concentrations above 0.25% and inhomogeneous solutions below that concentration with local pockets of gelling agarose and fluid regions of saline which did not permit for a uniform suspension of microbeads. Fructose and PBS solutions demonstrated uniform suspensions with increasing suspension duration with increasing fructose concentration. Both Fructose solutions of 80% and 100% were found to provide suitable suspension time, but 100% fructose was rejected as an injection vehicle due to its high viscosity and difficult to draw into a syringe or inject; both issues that 80% fructose did not encounter thus it was selected as the injection vehicle for this study.

7.4.2 Microbead Density Calibration and Localization

After the injection vehicle for the microbead was determined the volume per injection site and the distance between injection sites were evaluated for optimal in vivo imaging. Densities of 5 μL and 10 μL of microbeads in 200 μL of fructose solution were examined as they yielded readily observable microbead concentration in initial microbead density tests. Injection volumes ranging from 5 μl to 20 μl were investigated at these microbead densities and it was observed an injected volume of 10 μL of suspended beads at a concentration of 5:200 yielded approximately 7 beads per site while being easy to repeat identical injection volumes (Table 7.1).

After microbead injection volumes were established the spacing between microbead injection sites was examined. Due to the stepping of 500 μm between injection sites was observed to provide clear delineations between injected microbeads.

7.4.3 Micromotion Measures - 2D Orthonormal Video

The first approach attempted to quantify micromotion in this study was by direct measuring of radiopaque microbeads. Initial tests of 2D imaging were performed in

Table 7.1.
Average number of microbeads per injected volume for varied concentration and of microbeads in fructose and volumes.

Microbead concentration	Injected Volume	Average Bead Count
10:200	10 μl	9.4 $\pm$ 4.2
10:200	15 μl	18.8 $\pm$ 8.3
5:200	5 μl	5.7 $\pm$ 3.1
5:200	10 μl	7.1 $\pm$ 3.8
5:200	15 μl	10.1 $\pm$ 4.1
5:200	20 μl	19.8 $\pm$ 7.9

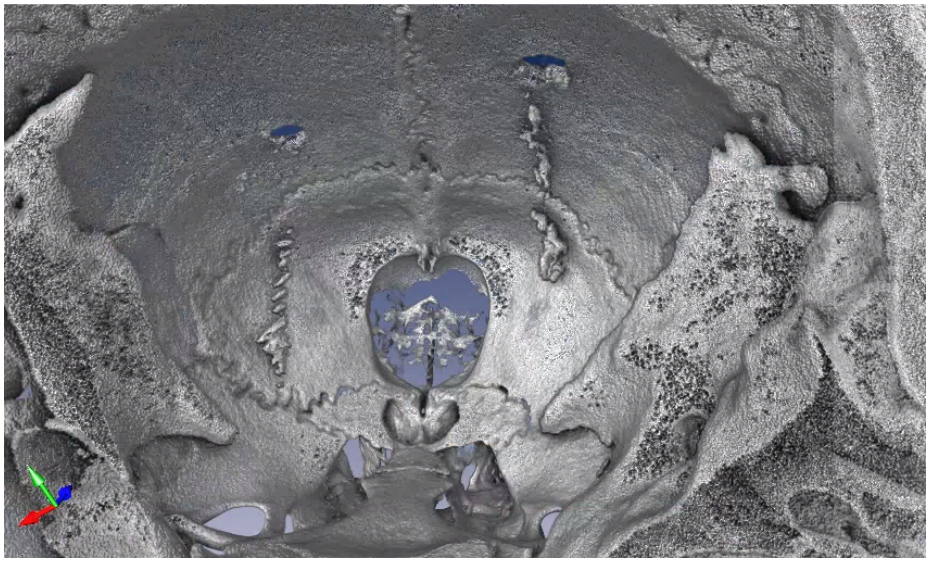

Fig. 7.3. 3D volume reconstruction of implanted microbeads within a rat cadaver. Beads were deposited at 500 μm steps for the track shown on the left whereas the beads were deposited at 250 μm

cadaver animals with manually implanted volumes of microbeads and it was observed that large clusters of microbeads, 100s of beads, were visible through the skull (Figure 7.4). When microbead densities per site were reduced to under 10 beads per site, implanted microbeads were no longer visible, likely due to reduced volume in comparison to the thickness of the skull.

7.4.4 Microbead Density Calibration and Localization

Initial high-resolution 3D volume reconstructions of embedded microbeads in a cadaver animal were obtained to confirm the proper placement and implantation of radiopaque microbeads (Figure 7.5). Imaging was performed at varying fields of view and at imaging resolutions. Individual bead details obtained in the FOV 5mm scans that are not present in the FOV 10mm scans indicate that smaller FOV scans be utilized for proper bead measurements, though little difference was observed between standard and high resolution scans apart from the surface quality of the imaged beads.

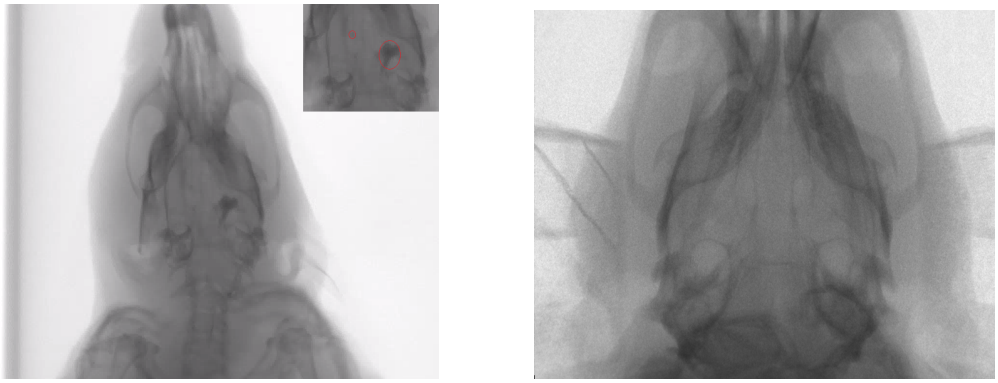

(a) High Microbead Density (b) Low Microbead Density

Fig. 7.4. 2D microCT scans taken of implanted radiopque microbeads in rat cadavers. A) Large volume of microbeads 1000+ in a cluser, microbeads circled in red. B) Low volume of microbeads under 10 beads per site, 3D reconstruction of the volume shown in Figure 7.3

Cadaver scans were followed by scans of live pilot animals implanted with microbeads (Figure 7.6). It was observed that injecting volumes of microbeads previously calibrated in cadavers at 10 μl did not provide sufficient microbead density for imaging. Increasing the injection volume to 20 μl did result in sufficient microbead density in vivo for imaging while providing space between individual beads.

7.4.5 In vivo Measurments

To measure the micromotion of the rat brain two female Sprague Dawley rats were implanted with radiopaque microbeads and imaged via microCT at one-week post surgery in this initial study (Figure 7.7). Micromotion was isolated for each microbead and measured along orthogonal axes defined as X (medial to lateral), Y (anterior to posterior), and Z (superior to inferior). Due to the true diameters of the individual beads being unknown at the current time point the manufacturer maximum (90 μm) and minimum (40 μm) diameters for the microbeads are used as limits to examine the range of possible micromotion observed (Table 7.2). Accurate

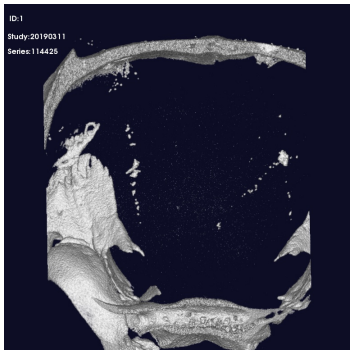

(a) High Res, FOV 10mm

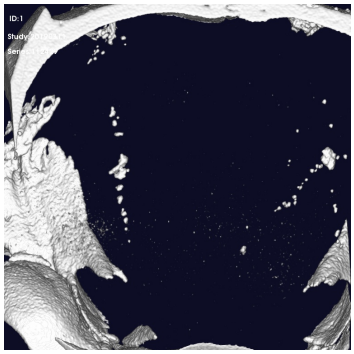

(b) Std Res, FOV 10mm

(c) High Res, FOV 5mm

(d) Std Res, FOV 5mm

Fig. 7.5. Reconstructed volume of radiopaque LUMI microbeads implanted in a cadaver animal. Note the more detailed surfaces on the high resolution scans whereas standard resolution scans have smoothed surfaces

measures of the microbead diameters can be obtained post live imaging sessions when the animal is sacrificed and the beads are imaged with no micromotion.

7.5 Discussion

The aim of this study was to develop a methodology for quantifying the resting state brain motion in rats without the confounds of previous studies into brain micromotion. In doing so a novel method for soft tissue motion quantification was developed such that a live animal could be imaged without severe surgical intervention,

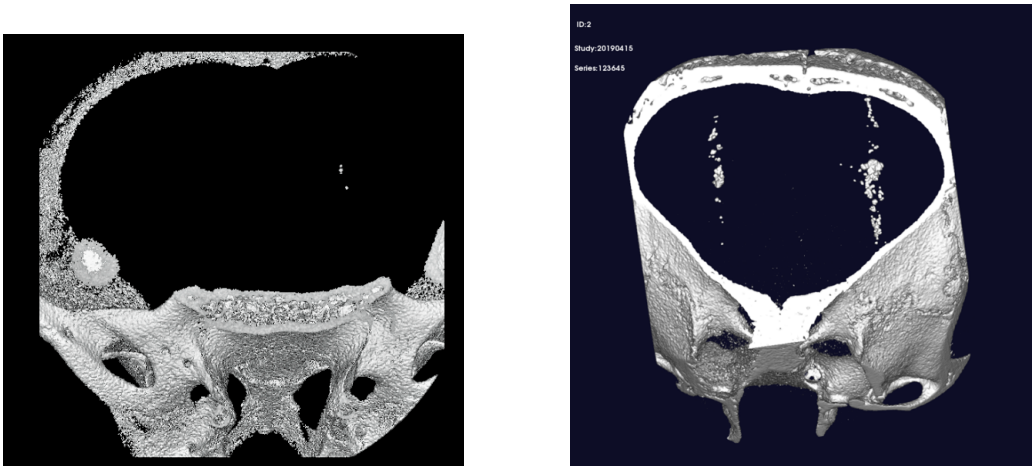

(a) 10 μl volume

(b) 20 μl volume

Fig. 7.6. Reconstructed volume of radiopaque LUMI microbeads implanted in a live animals. Initial injection of 10 μl of microbead mixture and injection of 20 μl of microbead mixture.

Table 7.2.
Average micromotion in μm for implanted microbeads in resting rat brains along the X (medial to lateral), Y (anterior to posterior), and Z (superior to inferior) axis. Number in parenthesis is standard deviation of motion.

Axis of Motion	40 μm bead motion	90 μm bead motion
X	20.4 μm (14.5)	41.8 μm (30.9)
Y	27.6 μm (10.9)	51.1 μm (29.0)
Z	24.2 μm (11.4)	44.8 μm (31.0)

only requiring the injection of radiopaque marker beads. Based on motion artifacts that generated when a sample moves during microCT scanning [272, 273] this study was able to implement a novel scanning technique to quantify the micromotion of the brain that provides high-resolution 3D measures of deep soft tissues.

MicroCT was selected as the imaging modality due to the high spatial resolution provided and functional temporal resolution offered in commercially available systems

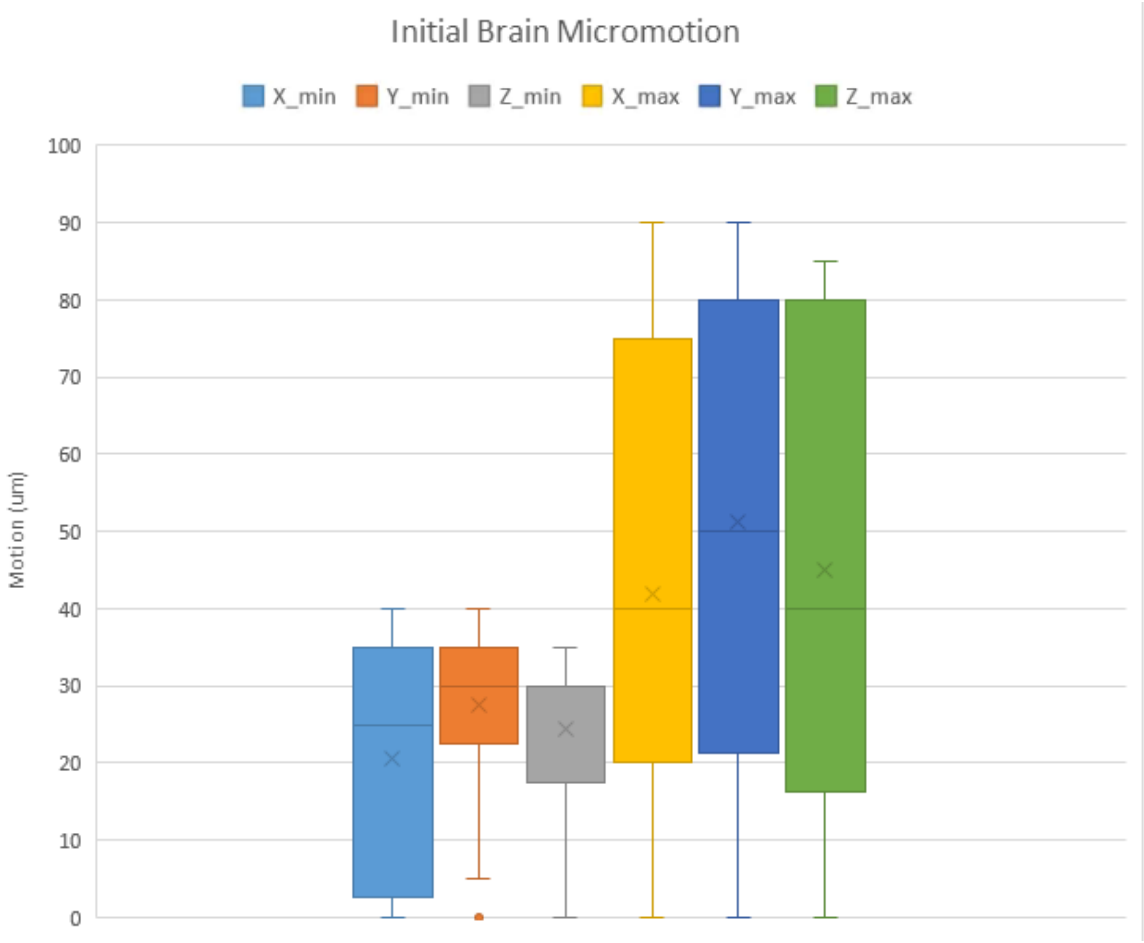

Fig. 7.7. Box and whisker plot of observed micromotion for implanted microbeads. X_{min}, Y_{min}, and Z_{min} represent motion along the x,y, and z axes respectively assuming microbead diameter of 40 μm. X_{max}, Y_{max}, and Z_{max} represent motion along the x,y, and z axes respectively assuming microbead diameter of 90 μm.

(10 Hz sampling rate, whereas the micromotion previously observed occurred at rates of 1-2 Hz for breathing and 2-4 Hz for heart rate). Other methods of quantifying brain micromotion were considered from magnetic resonance imaging (MRI), ultrasound, and direct probing of the brain. But these were discarded in favor for microCT for various reasons such as the relatively low resolution of MRI and ultrasound, the confounds of injury and outside mechanical strain inherent with penetrating probes,

and the inability to visually image through the skull for optical modalities of motion measurement.

The use of microCT imaging implanted microbeads allowed for this study to overcome the limitations of prior research [80] where motion was only quantified at the surface of the cortex at one region of the brain, in one dimension, and possibly confounded by an open craniectomy. In this study, researchers were able to demonstrate a method of micromotion imaging wherein radiopaque beads were implanted throughout the brain at different depths then non-invasively measured via microCT in three dimensions. This not only provides a method for quantifying brain micromotion but the motion of other soft tissues throughout the body at high resolution (4.5 μm) even in the presence of obscuring features such as bone allowing for this imaging modality to quantify the motion of soft tissues throughout the body rather than bone as previous studies have investigated [285–287].

This initial study was able to observe micromotion within the brain from ranging from 20.4 μm of motion up to 51.1 μm. The lower bounds of the motion measured to fall within previously published measures [254], approximately 15 to 30 μm, but as previously discussed those results are limited by a single location of the surface of the cortex and confounded by due to the measures being taken in an open craniotomy. At current, only an approximate range of micromotion can be described from the imaged microbeads as the true volume for each microbead has yet to be quantified. Upon post-sacrifice of the implanted animals a measure of the implanted microbeads without any motion artifacts can be performed to determine the true size for each implanted microbead and by extension the precise motion. Still, the current ranges of brain motion did provide evidence of three-dimensional micromotion with increased motion along the Y (medial/lateral) axis relative to the axes. Future analysis examining the motion of each individual microbead along the implantation tract will provide more accurate measures of the motion of the brain in the region proximal to the implantation tract.

With more accurate measures of brain micromotion, like those that can be quantified using the method developed in this study, existing models can be updated to better reflect motion boundary conditions and electrode designs can be adjusted to fit their particular region of the brain. By more accurately defining the boundary conditions of simulation models of the brain and its nominal motion, both simulation studies exploring the optimization of neural implant design are improved but also models that investigate the nominal physiological environment of the brain, i.e. the resting mechanical strains that various regions of the brain are in balance with and will promote optimal neurological health. Second by defining the motion of the whole brain can inform implementation of existing medical devices for observation and intervention, such as the optimal pathway through the brain that will induce the least amount of motion related strain in the brain; for instance electrodes could target the same deep brain region, but two paths may produce different strains along the length of the wire lead or electrode shaft due to the brain motion along those paths.

While in this study 3D volume reconstruction was implemented to measure the motion of the brain, other microCT based measurements may also be viable with more powerful equipment or comprehensive control systems. 2D microCT scanning sequences, for example, offer a simple and straightforward method to quantify motion providing direct measures of motion paired which can be paired with temporal measures. Regrettably, this approach to imaging requires high power and large doses of radiation per imaging session, both reason why this approach was not be implemented in the current longitudinal study which utilizes a Quantum GX microCT scanner incapable of resolving individual LUMI microbeads within the skull. This is likely due to the low power of the scanner being unable to reach the power level of other imaging systems used by studies that directly imaged inter-cranial LUMI microbeads [275, 279]. Additionally, the obfuscation of the small microbead volumes by the larger and thicker skull even though the microbeads have a higher density compared to the skull, 4000 HU versus 344 HU to 1828 HU [288]. Temporally gated imaging was also considered for this study wherein scans of the brain and bead motion

would only be taken at peaks or troughs of the respiratory cycle or cardiac cycle. This also could not be implemented due to the limitations of the hardware available. But the future implementation of either of these methodologies would allow for further expansion of the findings of this study, in particular, correlating brain micromotion with other physiological processes of the body and refining previous observations that brain motion is influenced by respiratory and cardiac rates [80].

Limitations

The key limitation of the current study is the power of available microCT scanners. Due to the low power scanner available to researchers, LUMI microbeads could only be visualized in 3D volume reconstruction. The load X-ray power does make it safer to perform long term multiscan analysis of micromotion and microbead drift, but limits imaging modalities. As observed in other studies microCT scanners with power over 42 Watt. Additionally, other scanners with higher resolution would be able to resolve the micromotion with greater precision, though this would come at the cost of greater radiation exposure.

Due to restrictions in the current hardware available, this study was unable to measure heart rate and respiration rate at the same time as the microbead imaging. Methods to quantify breathing without impeding the normal biological function of the rat such as a piezoelectric transducer [289] or pneumatic pillow [290] placed under the thorax could be implemented to obtain real-time measures of the respiratory and systolic cycles. This paired with modulating the heart rate and respiration rate by adjusting the ambient temperature of the animals, warming and cooling the rats, to investigate the relationship of both respiration and cardiac cycle on brain motion and determine if brain motion was due to both, one, or neither.

Another key limitation of the current study is that only brain motion of an unconscious animal can be quantified. For internal brain motion, this is likely to be the nominal case, only large impacts to the head are likely to cause deformations

to internal brain structures, but for the cortical surface, there is motion caused by head motion, minor impacts, and gross body movements that are currently unable to be imaged. This is due to the requirement that an animal is locked in position within a scanner to quantify brain motion. Perhaps future investigation can develop a wearable imaging system or the capabilities to quantify and locally register motion of the brain with the skull or other anatomical landmarks.

Though microbead descent tests were performed and imaged to assess the accuracy of the micromotion measures the lack of available microactuators with travel distances between 5 to 100 μm in this study made precise quantification of micromotion limited. With a calibrated microactuator displacements could be applied in all three dimensions rather than the one dimension available in the performed descent tests and the motion could be precisely controlled rather than averaged across the microbeads descending in the observed volume.

7.6 Conclusion

In this study, we have demonstrated a methodology to quantify the brain micromotion via implanted radiopaque beads in the resting rat brain. This approach addresses many of the prior limitations observed in previous work performed by quantifying the brain motion in three dimensions, at different locations in the brain, and in an in vivo model similar to chronic neural implantation. Initial measures found motion ranging between 20 μm and 50 μm, with variance higher motion along the medial/lateral axis. This methodology demonstrates not only the ability to quantify brain micromotion but the motion of soft tissues throughout the body.

8. CONCLUSION

The brain is the center of thought, the origin of all our actions, and the physical matter that makes us who we are; thus, it's crucial that it be protected. Be it the large impacts and TBI that athletes expose themselves to on daily basis or the constant perturbations of a neural electrode implanted deep in the brain, it is paramount that the physical forces acting upon the brain be minimized. And through careful monitoring, improved technique, and intelligent device design, this goal can be accomplished for both contact sports and neural implants.

8.0.1 Conclusions for Contact Sports

Accurate observation of HAEs can allow for precise monitoring of a player's exposure to hits and accumulation of head accelerations, both of which are correlated with changes in neurological health. This information can then be provided to coaches and athletic physicians and serve as a valuable tool in the prevention of harmful neurological changes and to protect the mental well being of their athletes. As has been previously reported, exposure to repeated HEAs is correlated with neurological changes affecting both the structure and function of the brain. By monitoring the accumulation of HAEs, these neurological changes can be avoided by prescribing healing periods or a change in technique that reduces the exposure to HAEs.

In an examination of middle school and high school students, it was found that player age and head size did not significantly affect the amount of accumulated HAEs players experienced. With the measurement systems used, this indicates that players younger, smaller players were exposed to similar forces as older, larger, stronger players, highlighting the risk to younger players. It was also observed that female soccer players experienced similar trends where age and size had little impact on

the amount of HAEs observed. These trends are likely due to the trade-off of player strength and player skill, such that as players become older and more experienced they acquire better play technique and avoid a large number of HAEs that they would have previously experienced, but at the same time they are exposed to far more HAEs due to the size and strength of players at their level. This indicates the need to improved technique at younger levels of play and the need to accurately quantify the exposure to all players over a wide range of ages and head sizes.

To improve the quality of HEA monitoring, a novel automated total head segmentation system was developed that allows for the measurement of player-specific geometries and generation of FEM ready simulation model. The developed head segmentation system analyzes not only the brain like other systems but also the rest of the head and is capable of performing an autonomous batch set analysis. Further, the system does not require a full head scan and can perform tissue segmentation on partial datasets which can occur in large population analyses, further increasing the applicability of the tools developed in this work and their potential to aid in research and possible health intervention and player safety.

Without appropriate head size measures, athletes will typically have underestimated PLA measurements when compared to an average model. Thus a single approach to assuming only one size of the head would be insufficient for an accurate model that aims to quantify the amount of acceleration a player has been exposed to and we must use individual measures to improve the accuracy of these measures, player safety, and quality of research in the field of TBI. And systems for quantifying the head and its individual geometries as demonstrated in chapter 4 are ways that researchers and athletic trainers/physicians can accurately monitor head accelerations and, if need be, intervene for a players health.

8.0.2 Conclusions for Neural Implant Design

A fundamental issue currently facing the widespread implementation of neural implants is the chronic performance of these devices post-implantation. Numerous studies have investigated how the chronic immune response affects implants that lead to their failure through device breakdown, neuronal apoptosis, and isolation of the implant via glial sheath encapsulation. Likewise, numerous researchers have sought ways of overcoming this immune response or bypassing it all together through a variety of means. In light of recent advances of ultrasmall and flexible electrodes [45, 139], it has become apparent the mechanical contribution of neural implants in the brain have a significant influence on the severity of the chronic immune response [138, 268].

While many variations in device design, material properties, and size have been evaluated both in vivo and in simulation, only general trends have been noted in the literature and no ordered ranking of what factors when adjusted produce the largest change in von Mises strain in the brain. To determine the influence that electrode design factors have on the mechanical strain in the brain, directly and relative to one another, a series of simulations were performed where electrodes of various sizes, shapes, and materials were displaced along different axes. From these simulations, Cotter's sensitivity analyses were performed revealing that the most sensitive design factor contributing to mechanical strain in the brain is the motion of the probe. It was found that maximal strain occurs when the probe pierces into the brain, and the lowest strain occurs when loading transverse along the widest face of the probe. Regretfully, brain micromotion is currently ill-defined in three dimensions for different regions of the brain, highlighting the need for further investigation to quantify micromotion of the brain. Bonding between the electrode and the brain was the second most sensitive design factor with frictionless contact producing lower strain in the brain relative to fully bonded contact, though higher peak strains were observed in the immediate vicinity of frictionless bonded probes. The brain to electrode bonding, like micromotion, currently also lacks in vivo metrics defining the degree of bonding

between the two. This highlights the need for well-defined boundary conditions of the brain electrode environment for accurate simulations. Following bonding, the next most sensitive factor is the size of the electrode in a majority of scenarios, with reduced electrode size causing decreased strain. To the authors' knowledge, this is the first study examining the relative influence of electrode design factors on mechanical strain induced in the brain by said electrodes. This study provides novel insights regarding electrode design that could substantially reduce strain, such as the importance of electrode orientation and design on the strain or that in most scenarios, a greater strain reduction could be achieved by minimizing electrode cross-sectional area rather than softening the electrode. This gives tools for researchers to explore electrode design spaces and optimize devices that not only reduce the von Mises strain produced, but also fill specialized design requirements all without resorting to electrode fabrications or animal studies until thoroughly analyzed in virtual space, saving time, money, and animals.

Inspired by the lack of quantified micromotion, a follow-up study was conducted to quantify the amount of micromotion in the brain to provide accurate boundary conditions to neural implant simulations and explore the physiology of the brain tied to brain micromotion. To investigate the brain micromotion, a novel form of motion quantification was developed that would allow the quantification of soft tissue motion in three dimensions throughout the brain without an open craniectomy. To accomplish this, a novel microCT imaging protocol which tracked the motion of embedded radiopaque microbeads in the brain was employed. By quantifying the distortion of the reconstructed microbead volume and then comparing it to the true volume of the microbeads, the motion of the microbead can be quantified over time.

Micromotion data and conclusions will be forthcoming shortly.

In addition to quantifying the brain micromotion, this study demonstrated a method of quantifying deep soft tissue motion throughout the body even when completely obscured by bone.

8.1 Future Research

While the research discussed in this thesis has explored a wide variety of topics regarding traumatic brain injury in contact sports and the mechanics of neural implants, a number of novel avenues for future research became apparent. Such was the case during the investigation of individualized head geometries in contact athletes and the ability to use the generated FEM geometries for more than just monitoring health. Of particular value would be to use the FEM geometries to investigate the mechanisms underlying the neurological changes correlated with TBI and accumulation of HAEs and develop methods to mitigate or relieve asymptomatic neurological changes.

Like the undefined micromotion boundary condition observed in chapter 6 the electrode to brain bonding currently lacks in vivo quantification data and has values ranging from frictionless bonding to completely bonded contacts [82]. From neural implantation studies where electrodes were explanted, it appears that there is some degree of cellular adhesion to the implant shaft, likely a bonded contact, though the degree of the bonding has not been quantified. Thus, to better define the bonding between the electrode and the brain, future research needs to be performed. In this particular case, an electrode pullout test could be performed to define the contact interface between the brain and electrode. Additional research could also be performed to better quantify the micromotion measured in chapter 7, particularly temporal measures. As discussed previously, the existing Quantum GX microCT scanner had relatively low power and could better investigate the contribution of breathing and heart rate of the resultant micromotion. To do this the heart rate and breathing rate can be adjusted by warming or cooling the animal.

8.2 Final Thoughts

With all the injuries that can befall the brain we require methods to accurately monitor, model, and measure our interactions with the nervous system. From the

high-velocity impacts of TBI to the μm motion of an electrode in the brain, accurate methods of modeling these environments are crucial if research and medical advancements are to be performed efficaciously. As we've seen the impacts that youth athletes are subjected to can cause disruptive neurological changes, appropriate monitoring and timed interventions are the best treatments we have at the moment and for that monitoring to be accurate, an individualized model must be used. The same applies to neural implants. While not dealing with person to person variances, electrodes placed in different regions of the brain are subjected to disparate environments and if these neural implants are to function chronically, they will need to be optimized with models personalized to the location and boundary conditions unique to the implant. In conclusion, for any form of modeling, a tool that can allow for accurate measurement and monitoring, or explorations of new design spaces models must be individualized and accurate.

REFERENCES

REFERENCES

[1] R. A. Stern, D. O. Riley, D. H. Daneshvar, C. J. Nowinski, R. C. Cantu, and A. C. McKee, "Long-term consequences of repetitive brain trauma: chronic traumatic encephalopathy," *Pm&r*, vol. 3, no. 10, pp. S460–S467, 2011.

[2] M. L. Alosco, A. B. Kasimis, J. M. Stamm, A. S. Chua, C. M. Baugh, D. H. Daneshvar, C. A. Robbins, M. Mariani, J. Hayden, S. Conneely, R. Au, A. Torres, M. D. McClean, A. C. McKee, R. C. Cantu, J. Mez, C. J. Nowinski, B. M. Martin, C. E. Chaisson, Y. Tripodis, and R. A. Stern, "Age of first exposure to American football and long-term neuropsychiatric and cognitive outcomes," *Transl Psychiatry*, vol. 7, no. 9, p. e1236, 09 2017.

[3] H. S. Martland, "Punch drunk," *Journal of the American Medical Association*, vol. 91, no. 15, pp. 1103–1107, 1928.

[4] T. M. Talavage, E. A. Nauman, and L. J. Leverenz, "The role of medical imaging in the recharacterization of mild traumatic brain injury using youth sports as a laboratory," *Frontiers in Neurology*, vol. 6, p. 273, 2016.

[5] T. M. Talavage, E. A. Nauman, E. L. Breedlove, U. Yoruk, A. E. Dye, K. E. Morigaki, H. Feuer, and L. J. Leverenz, "Functionally-detected cognitive impairment in high school football players without clinically-diagnosed concussion," *Journal of neurotrauma*, vol. 31, no. 4, pp. 327–338, 2014.

[6] C. A. Tagge, A. M. Fisher, O. V. Minaeva, A. Gaudreau-Balderrama, J. A. Moncaster, X.-L. Zhang, M. W. Wojnarowicz, N. Casey, H. Lu, O. N. Kokiko-Cochran *et al.*, "Concussion, microvascular injury, and early tauopathy in young athletes after impact head injury and an impact concussion mouse model," *Brain*, vol. 141, no. 2, pp. 422–458, 2018.

[7] A. C. McKee, R. C. Cantu, C. J. Nowinski, E. T. Hedley-Whyte, B. E. Gavett, A. E. Budson, V. E. Santini, H.-S. Lee, C. A. Kubilus, and R. A. Stern, "Chronic traumatic encephalopathy in athletes: progressive tauopathy after repetitive head injury," *Journal of Neuropathology & Experimental Neurology*, vol. 68, no. 7, pp. 709–735, 2009.

[8] C. M. Baugh, J. M. Stamm, D. O. Riley, B. E. Gavett, M. E. Shenton, A. Lin, C. J. Nowinski, R. C. Cantu, A. C. McKee, and R. A. Stern, "Chronic traumatic encephalopathy: neurodegeneration following repetitive concussive and subconcussive brain trauma," *Brain imaging and behavior*, vol. 6, no. 2, pp. 244–254, 2012.

[9] B. E. Gavett, R. A. Stern, and A. C. McKee, "Chronic traumatic encephalopathy: a potential late effect of sport-related concussive and subconcussive head trauma," *Clin Sports Med*, vol. 30, no. 1, pp. 179–188, Jan 2011.

[10] V. G. Coronado, L. C. McGuire, M. Faul, D. E. Sugerman, and W. S. Pearson, "Traumatic brain injury epidemiology and public health issues," *Brain injury medicine: Principles and practice*, vol. 84, 2012.

[11] C. M. Baugh, P. T. Kiernan, E. Kroshus, D. H. Daneshvar, P. H. Montenigro, A. C. McKee, and R. A. Stern, "Frequency of head-impact–related outcomes by position in ncaa division i collegiate football players," *Journal of neurotrauma*, vol. 32, no. 5, pp. 314–326, 2015.

[12] A. E. Lincoln, S. V. Caswell, J. L. Almquist, R. E. Dunn, J. B. Norris, and R. Y. Hinton, "Trends in concussion incidence in high school sports: a prospective 11-year study," *The American journal of sports medicine*, vol. 39, no. 5, pp. 958–963, 2011.

[13] B. Johnson, K. Zhang, M. Gay, S. Horovitz, M. Hallett, W. Sebastianelli, and S. Slobounov, "Alteration of brain default network in subacute phase of injury in concussed individuals: resting-state fmri study," *Neuroimage*, vol. 59, no. 1, pp. 511–518, 2012.

[14] T. M. Talavage, E. A. Nauman, and L. J. Leverenz, "The Role of Medical Imaging in the Recharacterization of Mild Traumatic Brain Injury Using Youth Sports as a Laboratory," *Front Neurol*, vol. 6, p. 273, 2015.

[15] I. Y. Chun, X. Mao, E. Breedlove, L. Leverenz, E. Nauman, and T. Talavage, "Dti detection of longitudinal wm abnormalities due to accumulated head impacts," *Developmental neuropsychology*, vol. 40, no. 2, pp. 92–97, 2015.

[16] K. Abbas, T. E. Shenk, V. N. Poole, E. L. Breedlove, L. J. Leverenz, E. A. Nauman, T. M. Talavage, and M. E. Robinson, "Alteration of default mode network in high school football athletes due to repetitive subconcussive mild traumatic brain injury: a resting-state functional magnetic resonance imaging study," *Brain connectivity*, vol. 5, no. 2, pp. 91–101, 2015.

[17] K. Abbas, T. E. Shenk, V. N. Poole, M. E. Robinson, L. J. Leverenz, E. A. Nauman, and T. M. Talavage, "Effects of repetitive sub-concussive brain injury on the functional connectivity of default mode network in high school football athletes," *Developmental neuropsychology*, vol. 40, no. 1, pp. 51–56, 2015.

[18] S. Bari, D. O. Svaldi, I. Jang, T. E. Shenk, V. N. Poole, T. Lee, U. Dydak, J. V. Rispoli, E. A. Nauman, and T. M. Talavage, "Dependence on subconcussive impacts of brain metabolism in collision sport athletes: an mr spectroscopic study," *Brain imaging and behavior*, pp. 1–15, 2018.

[19] D. O. Svaldi, C. Joshi, E. C. McCuen, J. P. Music, R. Hannemann, L. J. Leverenz, E. A. Nauman, and T. M. Talavage, "Accumulation of high magnitude acceleration events predicts cerebrovascular reactivity changes in female high school soccer athletes," *Brain imaging and behavior*, pp. 1–11, 2018.

[20] S. Savage, "When u.s. air force discovered the flaw of averages," *The Star*, Jan 2016. [Online]. Available: https://www.thestar.com/news/insight/2016/01/16/when-us-air-force-discovered-the-flaw-of-averages.html

[21] A. F. Roche, D. Mukherjee, S. M. Guo, and W. M. Moore, "Head circumference reference data: birth to 18 years," *Pediatrics*, vol. 79, no. 5, pp. 706–712, May 1987.

[22] B. A. Cordeiro, F. M. Stefani, and E. M. Goldfeder, "Study of the correlation between the linear measurements of the skull and face and palatal wide and length measures," *Codas*, vol. 27, no. 5, pp. 472–477, Sep. 2015.

[23] R. P. Ching, "Relationship between head mass and circumference in human adults," *University of Washington. Technical Brief*, 2007.

[24] K. L. Chou, S. Grube, and P. G. Patil, *Deep brain stimulation: A new life for people with Parkinson's, dystonia, and essential Tremor*. Demos Medical Publishing, 2011.

[25] J. Gardner, "A history of deep brain stimulation: Technological innovation and the role of clinical assessment tools," *Soc. Stud. Sci.*, vol. 43, no. 5, pp. 707–728, Oct. 2013.

[26] A. L. Benabid, S. Chabardes, J. Mitrofanis, and P. Pollak, "Deep brain stimulation of the subthalamic nucleus for the treatment of parkinson's disease," *The Lancet Neurology*, vol. 8, no. 1, pp. 67–81, 2009.

[27] J. L. Abelson, G. C. Curtis, O. Sagher, R. C. Albucher, M. Harrigan, S. F. Taylor, B. Martis, and B. Giordani, "Deep brain stimulation for refractory obsessive-compulsive disorder," *Biological psychiatry*, vol. 57, no. 5, pp. 510–516, 2005.

[28] V. Sturm, D. Lenartz, A. Koulousakis, H. Treuer, K. Herholz, J. C. Klein, and J. Klosterkötter, "The nucleus accumbens: a target for deep-brain stimulation in obsessive-compulsive and anxiety disorders," in *Proceedings of the Medtronic Forum for Neuroscience and Neuro-Technology 2005*. Springer, 2007, pp. 62–67.

[29] A. Taghva, J. D. Corrigan, and A. R. Rezai, "Obesity and brain addiction circuitry: implications for deep brain stimulation," *Neurosurgery*, vol. 71, no. 2, pp. 224–238, Aug 2012.

[30] C. Cusin and D. D. Dougherty, "Somatic therapies for treatment-resistant depression: Ect, tms, vns, dbs," *Biology of Mood & Anxiety Disorders*, vol. 2, no. 1, p. 14, 2012.

[31] R. Varma, T. S. Vajaranant, B. Burkemper, S. Wu, M. Torres, C. Hsu, F. Choudhury, and R. McKean-Cowdin, "Visual Impairment and Blindness in Adults in the United States: Demographic and Geographic Variations From 2015 to 2050," *JAMA Ophthalmol*, vol. 134, no. 7, pp. 802–809, 07 2016.

[32] K. D. Frick, M. C. Roebuck, J. I. Feldstein, C. A. McCarty, and L. L. Grover, "Health services utilization and cost of retinitis pigmentosa," *Archives of Ophthalmology*, vol. 130, no. 5, pp. 629–634, 2012.

[33] F. R. Lin, J. K. Niparko, and L. Ferrucci, "Hearing loss prevalence in the united states," *Archives of internal medicine*, vol. 171, no. 20, pp. 1851–1853, 2011.

[34] D. G. R. Evans, A. Moran, A. King, S. Saeed, N. Gurusinghe, and R. Ramsden, "Incidence of vestibular schwannoma and neurofibromatosis 2 in the north west of england over a 10-year period: higher incidence than previously thought," *Otology & Neurotology*, vol. 26, no. 1, pp. 93–97, 2005.

[35] ——, "Incidence of vestibular schwannoma and neurofibromatosis 2 in the north west of england over a 10-year period: Higher incidence than previously thought," pp. 93–97, 2005.

[36] Chrostopher & Dana Reeve Foundation, "One degree of separation: Paralysis and spinal cord injury in the united states," Chrostopher & Dana Reeve Foundation, Tech. Rep., 2012.

[37] K. Ziegler-Graham, E. J. MacKenzie, P. L. Ephraim, T. G. Travison, and R. Brookmeyer, "Estimating the prevalence of limb loss in the united states: 2005 to 2050," *Arch. Phys. Med. Rehabil.*, vol. 89, no. 3, pp. 422–429, Mar. 2008.

[38] P. A. Romitti, Y. Zhu, S. Puzhankara, K. A. James, S. K. Nabukera, G. K. Zamba, E. Ciafaloni, C. Cunniff, C. M. Druschel, K. D. Mathews, D. J. Matthews, F. J. Meaney, J. G. Andrews, K. M. Conway, D. J. Fox, N. Street, M. M. Adams, and J. Bolen, "Prevalence of Duchenne and Becker muscular dystrophies in the United States," *Pediatrics*, vol. 135, no. 3, pp. 513–521, Mar 2015.

[39] M. A. L. Nicolelis, D. Dimitrov, J. M. Carmena, R. Crist, G. Lehew, J. D. Kralik, and S. P. Wise, "Chronic, multisite, multielectrode recordings in macaque monkeys," *Proc. Natl. Acad. Sci. U. S. A.*, vol. 100, no. 19, pp. 11 041–11 046, Sep. 2003.

[40] R. J. Vetter, J. C. Williams, J. F. Hetke, E. A. Nunamaker, and D. R. Kipke, "Chronic neural recording using silicon-substrate microelectrode arrays implanted in cerebral cortex," *IEEE Trans. Biomed. Eng.*, vol. 51, no. 6, pp. 896–904, Jun. 2004.

[41] S. M. Willerth and S. E. Sakiyama-Elbert, "Approaches to neural tissue engineering using scaffolds for drug delivery," *Advanced drug delivery reviews*, vol. 59, no. 4-5, pp. 325–338, 2007.

[42] R. J. Vetter, J. C. Williams, J. F. Hetke, E. A. Nunamaker, and D. R. Kipke, "Chronic neural recording using silicon-substrate microelectrode arrays implanted in cerebral cortex," *IEEE transactions on biomedical engineering*, vol. 51, no. 6, pp. 896–904, 2004.

[43] J. C. Williams, R. L. Rennaker, and D. R. Kipke, "Long-term neural recording characteristics of wire microelectrode arrays implanted in cerebral cortex," *Brain Research Protocols*, vol. 4, no. 3, pp. 303–313, 1999.

[44] G. C. McConnell, H. D. Rees, A. I. Levey, C.-A. Gutekunst, R. E. Gross, and R. V. Bellamkonda, "Implanted neural electrodes cause chronic, local inflammation that is correlated with local neurodegeneration," *J. Neural Eng.*, vol. 6, no. 5, p. 056003, Oct. 2009.

[45] T. D. Y. Kozai, N. B. Langhals, P. R. Patel, X. Deng, H. Zhang, K. L. Smith, J. Lahann, N. A. Kotov, and D. R. Kipke, "Ultrasmall implantable composite microelectrodes with bioactive surfaces for chronic neural interfaces," *Nature materials*, vol. 11, no. 12, p. 1065, 2012.

[46] L. R. Hochberg, D. Bacher, B. Jarosiewicz, N. Y. Masse, J. D. Simeral, J. Vogel, S. Haddadin, J. Liu, S. S. Cash, P. van der Smagt, and J. P. Donoghue, "Reach and grasp by people with tetraplegia using a neurally controlled robotic arm," *Nature*, vol. 485, no. 7398, pp. 372–375, May 2012.

[47] J. Simeral, S.-P. Kim, M. Black, J. Donoghue, and L. Hochberg, "Neural control of cursor trajectory and click by a human with tetraplegia 1000 days after implant of an intracortical microelectrode array," *Journal of neural engineering*, vol. 8, no. 2, p. 025027, 2011.

[48] B. D. Winslow and P. A. Tresco, "Quantitative analysis of the tissue response to chronically implanted microwire electrodes in rat cortex," *Biomaterials*, vol. 31, no. 7, pp. 1558–1567, Mar. 2010.

[49] R. Biran, D. C. Martin, and P. A. Tresco, "Neuronal cell loss accompanies the brain tissue response to chronically implanted silicon microelectrode arrays," *Experimental neurology*, vol. 195, no. 1, pp. 115–126, 2005.

[50] B. D. Winslow, M. B. Christensen, W.-K. Yang, F. Solzbacher, and P. A. Tresco, "A comparison of the tissue response to chronically implanted parylene-c-coated and uncoated planar silicon microelectrode arrays in rat cortex," *Biomaterials*, vol. 31, no. 35, pp. 9163–9172, 2010.

[51] M. A. Nicolelis, D. Dimitrov, J. M. Carmena, R. Crist, G. Lehew, J. D. Kralik, and S. P. Wise, "Chronic, multisite, multielectrode recordings in macaque monkeys," *Proceedings of the National Academy of Sciences*, vol. 100, no. 19, pp. 11 041–11 046, 2003.

[52] V. S. Polikov, P. A. Tresco, and W. M. Reichert, "Response of brain tissue to chronically implanted neural electrodes," *Journal of neuroscience methods*, vol. 148, no. 1, pp. 1–18, 2005.

[53] T. Kozai, T. Marzullo, F. Hooi, N. Langhals, A. Majewska, E. Brown, and D. Kipke, "Reduction of neurovascular damage resulting from microelectrode insertion into the cerebral cortex using in vivo two-photon mapping," *Journal of neural engineering*, vol. 7, no. 4, p. 046011, 2010.

[54] D. M. Landis, "The early reactions of non-neuronal cells to brain injury," *Annual review of neuroscience*, vol. 17, no. 1, pp. 133–151, 1994.

[55] G. W. Kreutzberg, "Microglia: a sensor for pathological events in the CNS," *Trends Neurosci.*, vol. 19, no. 8, pp. 312–318, Aug. 1996.

[56] W. J. Streit, "Microglial response to brain injury: a brief synopsis," *Toxicol. Pathol.*, vol. 28, no. 1, pp. 28–30, Jan. 2000.

[57] T. D. Y. Kozai, A. L. Vazquez, C. L. Weaver, S.-G. Kim, and X. T. Cui, "In vivo two-photon microscopy reveals immediate microglial reaction to implantation of microelectrode through extension of processes," *Journal of neural engineering*, vol. 9, no. 6, p. 066001, 2012.

[58] E.-A. Ling and W.-C. Wong, "The origin and nature of ramified and amoeboid microglia: a historical review and current concepts," *Glia*, vol. 7, no. 1, pp. 9–18, 1993.

[59] T. Fujita, T. Yoshimine, M. Maruno, and T. Hayakawa, "Cellular dynamics of macrophages and microglial cells in reaction to stab wounds in rat cerebral cortex," *Acta neurochirurgica*, vol. 140, no. 3, pp. 275–279, 1998.

[60] D. Giulian, K. Vaca, and M. Corpuz, "Brain glia release factors with opposing actions upon neuronal survival," *Journal of Neuroscience*, vol. 13, no. 1, pp. 29–37, 1993.

[61] D. Szarowski, M. Andersen, S. Retterer, A. Spence, M. Isaacson, H. Craighead, J. Turner, and W. Shain, "Brain responses to micro-machined silicon devices," *Brain research*, vol. 983, no. 1-2, pp. 23–35, 2003.

[62] J. Turner, W. Shain, D. Szarowski, M. Andersen, S. Martins, M. Isaacson, and H. Craighead, "Cerebral astrocyte response to micromachined silicon implants," *Experimental neurology*, vol. 156, no. 1, pp. 33–49, 1999.

[63] D. B. McCreery, T. G. Yuen, W. F. Agnew, and L. A. Bullara, "A characterization of the effects on neuronal excitability due to prolonged microstimulation with chronically implanted microelectrodes," *IEEE transactions on biomedical engineering*, vol. 44, no. 10, pp. 931–939, 1997.

[64] R. Biran, D. C. Martin, and P. A. Tresco, "Neuronal cell loss accompanies the brain tissue response to chronically implanted silicon microelectrode arrays," *Exp. Neurol.*, vol. 195, no. 1, pp. 115–126, Sep. 2005.

[65] D. J. Edell, V. Toi, V. M. McNeil, and L. Clark, "Factors influencing the biocompatibility of insertable silicon microshafts in cerebral cortex," *IEEE Transactions on Biomedical Engineering*, vol. 39, no. 6, pp. 635–643, 1992.

[66] V. S. Polikov, M. L. Block, J.-M. Fellous, J.-S. Hong, and W. M. Reichert, "In vitro model of glial scarring around neuroelectrodes chronically implanted in the cns," *Biomaterials*, vol. 27, no. 31, pp. 5368–5376, 2006.

[67] D. H. Szarowski, M. D. Andersen, S. Retterer, A. J. Spence, M. Isaacson, H. G. Craighead, J. N. Turner, and W. Shain, "Brain responses to micro-machined silicon devices," *Brain Res.*, vol. 983, no. 1-2, pp. 23–35, Sep. 2003.

[68] B. D. Winslow and P. A. Tresco, "Quantitative analysis of the tissue response to chronically implanted microwire electrodes in rat cortex," *Biomaterials*, vol. 31, no. 7, pp. 1558–1567, 2010.

[69] A. J. Woolley, H. A. Desai, and K. J. Otto, "Chronic intracortical microelectrode arrays induce non-uniform, depth-related tissue responses," *Journal of neural engineering*, vol. 10, no. 2, p. 026007, 2013.

[70] J. P. Frampton, M. R. Hynd, M. L. Shuler, and W. Shain, "Effects of glial cells on electrode impedance recorded from neural prosthetic devices in vitro," *Annals of biomedical engineering*, vol. 38, no. 3, pp. 1031–1047, 2010.

[71] A. J. Woolley, H. A. Desai, M. A. Steckbeck, N. K. Patel, and K. J. Otto, "In situ characterization of the brain–microdevice interface using device capture histology," *Journal of neuroscience methods*, vol. 201, no. 1, pp. 67–77, 2011.

[72] I. B. Wanner, A. Deik, M. Torres, A. Rosendahl, J. T. Neary, V. P. Lemmon, and J. L. Bixby, "A new in vitro model of the glial scar inhibits axon growth," *Glia*, vol. 56, no. 15, pp. 1691–1709, 2008.

[73] G. McConnell, R. Butera, and R. Bellamkonda, "Bioimpedance modeling to monitor astrocytic response to chronically implanted electrodes," *Journal of neural engineering*, vol. 6, no. 5, p. 055005, 2009.

[74] M. D. Johnson, K. J. Otto, and D. R. Kipke, "Repeated voltage biasing improves unit recordings by reducing resistive tissue impedances," *IEEE Transactions on neural systems and rehabilitation engineering*, vol. 13, no. 2, pp. 160–165, 2005.

[75] J. D. Weiland and D. J. Anderson, "Chronic neural stimulation with thin-film, iridium oxide electrodes," *IEEE Transactions on Biomedical Engineering*, vol. 47, no. 7, pp. 911–918, 2000.

[76] J. C. Williams, J. A. Hippensteel, J. Dilgen, W. Shain, and D. R. Kipke, "Complex impedance spectroscopy for monitoring tissue responses to inserted neural implants," *Journal of neural engineering*, vol. 4, no. 4, p. 410, 2007.

[77] M. L. Block, L. Zecca, and J.-S. Hong, "Microglia-mediated neurotoxicity: uncovering the molecular mechanisms," *Nat. Rev. Neurosci.*, vol. 8, no. 1, pp. 57–69, Jan. 2007.

[78] K. A. Potter, A. C. Buck, W. K. Self, and J. R. Capadona, "Stab injury and device implantation within the brain results in inversely multiphasic neuroinflammatory and neurodegenerative responses," *Journal of neural engineering*, vol. 9, no. 4, p. 046020, 2012.

[79] G. C. McConnell, H. D. Rees, A. I. Levey, C.-A. Gutekunst, R. E. Gross, and R. V. Bellamkonda, "Implanted neural electrodes cause chronic, local inflammation that is correlated with local neurodegeneration," *Journal of neural engineering*, vol. 6, no. 5, p. 056003, 2009.

[80] A. Gilletti and J. Muthuswamy, "Brain micromotion around implants in the rodent somatosensory cortex," *J. Neural Eng.*, vol. 3, no. 3, pp. 189–195, Sep. 2006.

[81] J. Subbaroyan, D. C. Martin, and D. R. Kipke, "A finite-element model of the mechanical effects of implantable microelectrodes in the cerebral cortex," *Journal of neural engineering*, vol. 2, no. 4, p. 103, 2005.

[82] J. K. Nguyen, D. J. Park, J. L. Skousen, A. E. Hess-Dunning, D. J. Tyler, S. J. Rowan, C. Weder, and J. R. Capadona, "Mechanically-compliant intracortical implants reduce the neuroinflammatory response," *J. Neural Eng.*, vol. 11, no. 5, p. 056014, Oct. 2014.

[83] M. Polanco, H. Yoon, and S. Bawab, "Micromotion-induced dynamic effects from a neural probe and brain tissue interface," p. 023009, 2014.

[84] L. W. Ostrow, T. M. Suchyna, and F. Sachs, "Stretch induced endothelin-1 secretion by adult rat astrocytes involves calcium influx via stretch-activated ion channels (SACs)," *Biochem. Biophys. Res. Commun.*, vol. 410, no. 1, pp. 81–86, Jun. 2011.

[85] B. A. Rzigalinski, J. T. Weber, K. A. Willoughby, and E. F. Ellis, "Intracellular free calcium dynamics in stretch-injured astrocytes," *J. Neurochem.*, vol. 70, no. 6, pp. 2377–2385, Jun. 1998.

[86] L. Karumbaiah, S. E. Norman, N. B. Rajan, S. Anand, T. Saxena, M. Betancur, R. Patkar, and R. V. Bellamkonda, "The upregulation of specific interleukin (il) receptor antagonists and paradoxical enhancement of neuronal apoptosis due to electrode induced strain and brain micromotion," *Biomaterials*, vol. 33, no. 26, pp. 5983–5996, 2012.

[87] C. A. Dinarello, "Immunological and inflammatory functions of the interleukin-1 family," *Annual review of immunology*, vol. 27, pp. 519–550, 2009.

[88] J. Jourquin, E. Tremblay, N. Décanis, G. Charton, S. Hanessian, A.-M. Chollet, T. Le Diguardher, M. Khrestchatisky, and S. Rivera, "Neuronal activity-dependent increase of net matrix metalloproteinase activity is associated with mmp-9 neurotoxicity after kainate," *European Journal of Neuroscience*, vol. 18, no. 6, pp. 1507–1517, 2003.

[89] J.-Y. C. Hsu, R. McKeon, S. Goussev, Z. Werb, J.-U. Lee, A. Trivedi, and L. J. Noble-Haeusslein, "Matrix metalloproteinase-2 facilitates wound healing events that promote functional recovery after spinal cord injury," *Journal of Neuroscience*, vol. 26, no. 39, pp. 9841–9850, 2006.

[90] S. Golde, A. Coles, J. A. Lindquist, and A. Compston, "Decreased inos synthesis mediates dexamethasone-induced protection of neurons from inflammatory injury in vitro," *European Journal of Neuroscience*, vol. 18, no. 9, pp. 2527–2537, 2003.

[91] W. Shain, L. Spataro, J. Dilgen, K. Haverstick, S. Retterer, M. Isaacson, M. Saltzman, and J. N. Turner, "Controlling cellular reactive responses around neural prosthetic devices using peripheral and local intervention strategies," *IEEE transactions on neural systems and rehabilitation engineering*, vol. 11, no. 2, pp. 186–188, 2003.

[92] L. Spataro, J. Dilgen, S. Retterer, A. Spence, M. Isaacson, J. Turner, and W. Shain, "Dexamethasone treatment reduces astroglia responses to inserted neuroprosthetic devices in rat neocortex," *Experimental neurology*, vol. 194, no. 2, pp. 289–300, 2005.

[93] J. L. Brugnano, B. K. Chan, B. L. Seal, and A. Panitch, "Cell-penetrating peptides can confer biological function: regulation of inflammatory cytokines in human monocytes by mk2 inhibitor peptides," *Journal of controlled release*, vol. 155, no. 2, pp. 128–133, 2011.

[94] R. Delgado, A. Carlin, L. Airaghi, M. T. Demitri, L. Meda, D. Galimberti, P. Baron, J. M. Lipton, and A. Catania, "Melanocortin peptides inhibit production of proinflammatory cytokines and nitric oxide by activated microglia," *Journal of leukocyte biology*, vol. 63, no. 6, pp. 740–745, 1998.

[95] T. Ichiyama, H. Zhao, A. Catania, S. Furukawa, and J. M. Lipton, "α-melanocyte-stimulating hormone inhibits nf-κb activation and iκbα degradation in human glioma cells and in experimental brain inflammation," *Experimental neurology*, vol. 157, no. 2, pp. 359–365, 1999.

[96] A. Golabchi, B. Wu, X. Li, D. L. Carlisle, T. D. Kozai, R. M. Friedlander, and X. T. Cui, "Melatonin improves quality and longevity of chronic neural recording," *Biomaterials*, vol. 180, pp. 225–239, 2018.

[97] E. J. Huang and L. F. Reichardt, "Neurotrophins: roles in neuronal development and function," *Annual review of neuroscience*, vol. 24, no. 1, pp. 677–736, 2001.

[98] R. Grill, K. Murai, A. Blesch, F. Gage, and M. Tuszynski, "Cellular delivery of neurotrophin-3 promotes corticospinal axonal growth and partial functional recovery after spinal cord injury," *Journal of Neuroscience*, vol. 17, no. 14, pp. 5560–5572, 1997.

[99] H. Ma, B. Yu, L. Kong, Y. Zhang, and Y. Shi, "Neural stem cells over-expressing brain-derived neurotrophic factor (bdnf) stimulate synaptic protein expression and promote functional recovery following transplantation in rat model of traumatic brain injury," *Neurochemical research*, vol. 37, no. 1, pp. 69–83, 2012.

[100] M. L. Willson, C. McElnea, J. Mariani, A. M. Lohof, and R. M. Sherrard, "Bdnf increases homotypic olivocerebellar reinnervation and associated fine motor and cognitive skill," *Brain*, vol. 131, no. 4, pp. 1099–1112, 2008.

[101] H. Craighead, S. Turner, R. Davis, C. James, A. Perez, P. S. John, M. Isaacson, L. Kam, W. Shain, J. Turner *et al.*, "Chemical and topographical surface modification for control of central nervous system cell adhesion," *Biomedical Microdevices*, vol. 1, no. 1, pp. 49–64, 1998.

[102] W. He, G. C. McConnell, and R. V. Bellamkonda, "Nanoscale laminin coating modulates cortical scarring response around implanted silicon microelectrode arrays," *J Neural Eng*, vol. 3, no. 4, pp. 316–326, Dec 2006.

[103] L. Kam, W. Shain, J. Turner, and R. Bizios, "Selective adhesion of astrocytes to surfaces modified with immobilized peptides," *Biomaterials*, vol. 23, no. 2, pp. 511–515, 2002.

[104] Y. Zhong, G. McConnell, J. Ross, S. DeWeerth, and R. Bellamkonda, "A novel dexamethasone-releasing, anti-inflammatory coating for neural implants," in *Conference Proceedings. 2nd International IEEE EMBS Conference on Neural Engineering, 2005.* IEEE, 2005, pp. 522–525.

[105] J. O. Winter, S. F. Cogan, and J. F. Rizzo III, "Neurotrophin-eluting hydrogel coatings for neural stimulating electrodes," *Journal of Biomedical Materials Research Part B: Applied Biomaterials: An Official Journal of The Society for Biomaterials, The Japanese Society for Biomaterials, and The Australian Society for Biomaterials and the Korean Society for Biomaterials*, vol. 81, no. 2, pp. 551–563, 2007.

[106] D. Lewitus, K. L. Smith, W. Shain, and J. Kohn, "Ultrafast resorbing polymers for use as carriers for cortical neural probes," *Acta biomaterialia*, vol. 7, no. 6, pp. 2483–2491, 2011.

[107] S. P. Massia, M. M. Holecko, and G. R. Ehteshami, "In vitro assessment of bioactive coatings for neural implant applications," *Journal of Biomedical Materials Research Part A: An Official Journal of The Society for Biomaterials, The Japanese Society for Biomaterials, and The Australian Society for Biomaterials and the Korean Society for Biomaterials*, vol. 68, no. 1, pp. 177–186, 2004.

[108] R. Wadhwa, C. F. Lagenaur, and X. T. Cui, "Electrochemically controlled release of dexamethasone from conducting polymer polypyrrole coated electrode," *Journal of controlled release*, vol. 110, no. 3, pp. 531–541, 2006.

[109] S. M. Gutowski, K. L. Templeman, A. B. South, J. C. Gaulding, J. T. Shoemaker, M. C. LaPlaca, R. V. Bellamkonda, L. A. Lyon, and A. J. García, "Host response to microgel coatings on neural electrodes implanted in the brain," *Journal of Biomedical Materials Research Part A*, vol. 102, no. 5, pp. 1486–1499, 2014.

[110] K. A. Ludwig, J. D. Uram, J. Yang, D. C. Martin, and D. R. Kipke, "Chronic neural recordings using silicon microelectrode arrays electrochemically deposited with a poly (3, 4-ethylenedioxythiophene)(pedot) film," *Journal of neural engineering*, vol. 3, no. 1, p. 59, 2006.

[111] S. J. Wilks, S. M. Richardson-Burn, J. L. Hendricks, D. Martin, and K. J. Otto, "Poly (3, 4-ethylene dioxythiophene)(pedot) as a micro-neural interface material for electrostimulation," *Frontiers in neuroengineering*, vol. 2, p. 7, 2009.

[112] S. J. Wilks, A. J. Woolley, L. Ouyang, D. C. Martin, and K. J. Otto, "In vivo polymerization of poly (3, 4-ethylenedioxythiophene)(pedot) in rodent cerebral cortex," in *2011 Annual International Conference of the IEEE Engineering in Medicine and Biology Society*. IEEE, 2011, pp. 5412–5415.

[113] X. Cui, V. A. Lee, Y. Raphael, J. A. Wiler, J. F. Hetke, D. J. Anderson, and D. C. Martin, "Surface modification of neural recording electrodes with conducting polymer/biomolecule blends," *Journal of Biomedical Materials Research: An Official Journal of The Society for Biomaterials, The Japanese Society for Biomaterials, and The Australian Society for Biomaterials and the Korean Society for Biomaterials*, vol. 56, no. 2, pp. 261–272, 2001.

[114] H. Yamato, M. Ohwa, and W. Wernet, "Stability of polypyrrole and poly (3, 4-ethylenedioxythiophene) for biosensor application," *Journal of Electroanalytical Chemistry*, vol. 397, no. 1-2, pp. 163–170, 1995.

[115] A. L. Pierce, S. Sommakia, J. L. Rickus, and K. J. Otto, "Thin-film silica sol–gel coatings for neural microelectrodes," *Journal of Neuroscience Methods*, vol. 180, no. 1, pp. 106–110, 2009.

[116] S. S. Jedlicka, J. L. Rickus, and D. Y. Zemlyanov, "Surface analysis by x-ray photoelectron spectroscopy of sol- gel silica modified with covalently bound peptides," *The Journal of Physical Chemistry B*, vol. 111, no. 40, pp. 11 850–11 857, 2007.

[117] S. S. Jedlicka, K. M. Little, D. E. Nivens, D. Zemlyanov, and J. L. Rickus, "Peptide ormosils as cellular substrates," *Journal of Materials Chemistry*, vol. 17, no. 48, pp. 5058–5067, 2007.

[118] K. J. Otto, M. D. Johnson, and D. R. Kipke, "Voltage pulses change neural interface properties and improve unit recordings with chronically implanted microelectrodes," *IEEE transactions on biomedical engineering*, vol. 53, no. 2, pp. 333–340, 2006.

[119] J. C. Lilly, J. R. Hughes, E. C. Alvord Jr, and T. W. Galkin, "Brief, noninjurious electric waveform for stimulation of the brain." *Science*, 1955.

[120] D. McCreery, W. Agnew, T. Yuen, and L. Bullara, "Comparison of neural damage induced by electrical stimulation with faradaic and capacitor electrodes," *Annals of biomedical engineering*, vol. 16, no. 5, pp. 463–481, 1988.

[121] D. R. Merrill, M. Bikson, and J. G. Jefferys, "Electrical stimulation of excitable tissue: design of efficacious and safe protocols," *Journal of neuroscience methods*, vol. 141, no. 2, pp. 171–198, 2005.

[122] S. Brummer and M. Turner, "Electrical stimulation of the nervous system: the principle of safe charge injection with noble metal electrodes," *Bioelectrochemistry and Bioenergetics*, vol. 2, no. 1, pp. 13–25, 1975.

[123] A. S. Koivuniemi and K. J. Otto, "Asymmetric versus symmetric pulses for cortical microstimulation," *IEEE Transactions on Neural Systems and Rehabilitation Engineering*, vol. 19, no. 5, pp. 468–476, 2011.

[124] A. Koivuniemi, S. J. Wilks, A. J. Woolley, and K. J. Otto, "Multimodal, longitudinal assessment of intracortical microstimulation," in *Progress in brain research*. Elsevier, 2011, vol. 194, pp. 131–144.

[125] A. Antal, N. Brepohl, C. Poreisz, K. Boros, G. Csifcsak, and W. Paulus, "Transcranial direct current stimulation over somatosensory cortex decreases experimentally induced acute pain perception," *Clin J Pain*, vol. 24, no. 1, pp. 56–63, Jan 2008.

[126] H. W. Lee, M. W. Youngblood, P. Farooque, X. Han, S. Jhun, W. C. Chen, I. Goncharova, K. Vives, D. D. Spencer, H. Zaveri, L. J. Hirsch, and H. Blumenfeld, "Seizure localization using three-dimensional surface projections of intracranial EEG power," *Neuroimage*, vol. 83, pp. 616–626, Dec 2013.

[127] L. A. Johnson, J. D. Wander, D. Sarma, D. K. Su, E. E. Fetz, and J. G. Ojemann, "Direct electrical stimulation of the somatosensory cortex in humans using electrocorticography electrodes: a qualitative and quantitative report," *J Neural Eng*, vol. 10, no. 3, p. 036021, Jun 2013.

[128] E. C. Leuthardt, Z. Freudenberg, D. Bundy, and J. Roland, "Microscale recording from human motor cortex: implications for minimally invasive electrocorticographic brain-computer interfaces," *Neurosurg Focus*, vol. 27, no. 1, p. E10, Jul 2009.

[129] M. Hallett, "Transcranial magnetic stimulation: a primer," *Neuron*, vol. 55, no. 2, pp. 187–199, 2007.

[130] K. Y. Kwon, H.-M. Lee, M. Ghovanloo, A. Weber, and W. Li, "Design, fabrication, and packaging of an integrated, wirelessly-powered optrode array for optogenetics application," *Frontiers in systems neuroscience*, vol. 9, p. 69, 2015.

[131] A. M. Aravanis, L.-P. Wang, F. Zhang, L. A. Meltzer, M. Z. Mogri, M. B. Schneider, and K. Deisseroth, "An optical neural interface: in vivo control of rodent motor cortex with integrated fiberoptic and optogenetic technology," *Journal of neural engineering*, vol. 4, no. 3, p. S143, 2007.

[132] S. Thongpang, T. J. Richner, S. K. Brodnick, A. Schendel, J. Kim, J. A. Wilson, J. Hippensteel, L. Krugner-Higby, D. Moran, A. S. Ahmed, D. Neimann, K. Sillay, and J. C. Williams, "A micro-electrocorticography platform and deployment strategies for chronic BCI applications," *Clin. EEG Neurosci.*, vol. 42, no. 4, pp. 259–265, Oct. 2011.

[133] J.-W. Jeong, G. Shin, S. I. Park, K. J. Yu, L. Xu, and J. A. Rogers, "Soft materials in neuroengineering for hard problems in neuroscience," *Neuron*, vol. 86, no. 1, pp. 175–186, Apr. 2015.

[134] T. Kim, A. Branner, T. Gulati, and S. F. Giszter, "Braided multi-electrode probes: mechanical compliance characteristics and recordings from spinal cords," *Journal of neural engineering*, vol. 10, no. 4, p. 045001, 2013.

[135] H. S. Sohal, A. Jackson, R. Jackson, G. J. Clowry, K. Vassilevski, A. O'Neill, and S. N. Baker, "The sinusoidal probe: a new approach to improve electrode longevity," *Front Neuroeng*, vol. 7, p. 10, 2014.

[136] B. J. Black, M. Ecker, A. Stiller, R. Rihani, V. R. Danda, I. Reed, W. E. Voit, and J. J. Pancrazio, "In vitro compatibility testing of thiol-ene/acrylate-based shape memory polymers for use in implantable neural interfaces," *J Biomed Mater Res A*, vol. 106, no. 11, pp. 2891–2898, Nov 2018.

[137] J. P. Seymour and D. R. Kipke, "Fabrication of polymer neural probes with sub-cellular features for reduced tissue encapsulation," *Conf. Proc. IEEE Eng. Med. Biol. Soc.*, vol. 1, pp. 4606–4609, 2006.

[138] J. Thelin, H. Jörntell, E. Psouni, M. Garwicz, J. Schouenborg, N. Danielsen, and C. E. Linsmeier, "Implant size and fixation mode strongly influence tissue reactions in the cns," *PloS one*, vol. 6, no. 1, p. e16267, 2011.

[139] L. Luan, X. Wei, Z. Zhao, J. J. Siegel, O. Potnis, C. A. Tuppen, S. Lin, S. Kazmi, R. A. Fowler, S. Holloway, A. K. Dunn, R. A. Chitwood, and C. Xie, "Ultraflexible nanoelectronic probes form reliable, glial scar–free neural integration," *Science Advances*, vol. 3, no. 2, p. e1601966, 2017.

[140] H.-Y. Lai, L.-D. Liao, C.-T. Lin, J.-H. Hsu, X. He, Y.-Y. Chen, J.-Y. Chang, H.-F. Chen, S. Tsang, and Y.-Y. I. Shih, "Design, simulation and experimental validation of a novel flexible neural probe for deep brain stimulation and multichannel recording," *J. Neural Eng.*, vol. 9, no. 3, p. 036001, Jun. 2012.

[141] W. Zhang, J. Tang, Z. Li, and Y. Ma, "A novel neural electrode with micromotion-attenuation capability based on compliant mechanisms-physical design concepts and evaluations," *Med. Biol. Eng. Comput.*, vol. 56, no. 10, pp. 1911–1923, Oct. 2018.

[142] J. P. Seymour and D. R. Kipke, "Neural probe design for reduced tissue encapsulation in cns," *Biomaterials*, vol. 28, no. 25, pp. 3594–3607, 2007.

[143] R. Khilwani, P. J. Gilgunn, T. D. Y. Kozai, X. C. Ong, E. Korkmaz, P. K. Gunalan, X. T. Cui, G. K. Fedder, and O. B. Ozdoganlar, "Ultra-miniature ultra-compliant neural probes with dissolvable delivery needles: design, fabrication and characterization," *Biomed. Microdevices*, vol. 18, no. 6, p. 97, Dec. 2016.

[144] Z. J. Du, C. L. Kolarcik, T. D. Y. Kozai, S. D. Luebben, S. A. Sapp, X. S. Zheng, J. A. Nabity, and X. T. Cui, "Ultrasoft microwire neural electrodes improve chronic tissue integration," *Acta Biomater.*, vol. 53, pp. 46–58, Apr. 2017.

[145] J. L. Skousen, S. M. E. Merriam, O. Srivannavit, G. Perlin, K. D. Wise, and P. A. Tresco, "Reducing surface area while maintaining implant penetrating profile lowers the brain foreign body response to chronically implanted planar silicon microelectrode arrays," in *Progress in brain research*. Elsevier, 2011, vol. 194, pp. 167–180.

[146] N. T. Markwardt, J. Stokol, and R. L. Rennaker, 2nd, "Sub-meninges implantation reduces immune response to neural implants," *J. Neurosci. Methods*, vol. 214, no. 2, pp. 119–125, Apr. 2013.

[147] R. Biran, D. C. Martin, and P. A. Tresco, "The brain tissue response to implanted silicon microelectrode arrays is increased when the device is tethered to the skull," *Journal of Biomedical Materials Research Part A*, vol. 82, no. 1, pp. 169–178, 2007.

[148] D. K. Menon, K. Schwab, D. W. Wright, A. I. Maas *et al.*, "Position statement: definition of traumatic brain injury," *Archives of physical medicine and rehabilitation*, vol. 91, no. 11, pp. 1637–1640, 2010.

[149] S. T. DeKosky, M. D. Ikonomovic, and S. Gandy, "Traumatic brain injuryfootball, warfare, and long-term effects," *New England Journal of Medicine*, vol. 363, no. 14, pp. 1293–1296, 2010.

[150] E. L. Breedlove, M. Robinson, T. M. Talavage, K. E. Morigaki, U. Yoruk, K. O'Keefe, J. King, L. J. Leverenz, J. W. Gilger, and E. A. Nauman, "Biomechanical correlates of symptomatic and asymptomatic neurophysiological impairment in high school football," *Journal of biomechanics*, vol. 45, no. 7, pp. 1265–1272, 2012.

[151] J. A. Langlois, W. Rutland-Brown, and M. M. Wald, "The epidemiology and impact of traumatic brain injury: a brief overview," *The Journal of head trauma rehabilitation*, vol. 21, no. 5, pp. 375–378, 2006.

[152] A. M. Black, L. E. Sergio, and A. K. Macpherson, "The epidemiology of concussions: number and nature of concussions and time to recovery among female and male canadian varsity athletes 2008 to 2011," *Clinical journal of sport medicine*, vol. 27, no. 1, pp. 52–56, 2017.

[153] M. McCrea, T. Hammeke, G. Olsen, P. Leo, and K. Guskiewicz, "Unreported concussion in high school football players: implications for prevention," *Clin. J. Sport Med.*, vol. 14, no. 1, pp. 13–17, Jan. 2004.

[154] L. M. Gessel, S. K. Fields, C. L. Collins, R. W. Dick, and R. D. Comstock, "Concussions among united states high school and collegiate athletes," *Journal of athletic training*, vol. 42, no. 4, p. 495, 2007.

[155] A. Schwarz, "Congress examines nfl concussions," *New York Times*, 2010.

[156] M. Marar, N. M. McIlvain, S. K. Fields, and R. D. Comstock, "Epidemiology of concussions among united states high school athletes in 20 sports," *The American journal of sports medicine*, vol. 40, no. 4, pp. 747–755, 2012.

[157] M. Locker, "Football head impacts can cause brain changes without concussion," *Time Magazine*, 2014.

[158] G. Reynolds, "A single concussion may have a lasting impact," *New York Times*, 2016.

[159] B. I. Omalu, S. T. DeKosky, R. L. Minster, M. I. Kamboh, R. L. Hamilton, and C. H. Wecht, "Chronic traumatic encephalopathy in a national football league player," *Neurosurgery*, vol. 57, no. 1, pp. 128–134, 2005.

[160] B. I. Omalu, S. T. DeKosky, R. L. Hamilton, R. L. Minster, M. I. Kamboh, A. M. Shakir, and C. H. Wecht, "Chronic traumatic encephalopathy in a national football league player: part ii," *Neurosurgery*, vol. 59, no. 5, pp. 1086–1093, 2006.

[161] B. I. Omalu, R. L. Hamilton, M. I. Kamboh, S. T. DeKosky, and J. Bailes, "Chronic traumatic encephalopathy (cte) in a national football league player: Case report and emerging medicolegal practice questions," *Journal of forensic nursing*, vol. 6, no. 1, pp. 40–46, 2010.

[162] J. Corsellis, C. Bruton, and F.-B. D., "The aftermath of boxing," *Psychological medicine*, no. 3, pp. 270–303, 1973.

[163] J. Mez, D. H. Daneshvar, P. T. Kiernan, B. Abdolmohammadi, V. E. Alvarez, B. R. Huber, M. L. Alosco, T. M. Solomon, C. J. Nowinski, L. McHale *et al.*, "Clinicopathological evaluation of chronic traumatic encephalopathy in players of american football," *Jama*, vol. 318, no. 4, pp. 360–370, 2017.

[164] J. E. Bailes, A. L. Petraglia, B. I. Omalu, E. Nauman, and T. Talavage, "Role of subconcussion in repetitive mild traumatic brain injury: a review," *Journal of neurosurgery*, vol. 119, no. 5, pp. 1235–1245, 2013.

[165] M. C. Stevens, D. Lovejoy, J. Kim, H. Oakes, I. Kureshi, and S. T. Witt, "Multiple resting state network functional connectivity abnormalities in mild traumatic brain injury," *Brain Imaging Behav.*, vol. 6, no. 2, pp. 293–318, 2012.

[166] M. E. Robinson, T. E. Shenk, E. L. Breedlove, L. J. Leverenz, E. A. Nauman, and T. M. Talavage, "The role of location of subconcussive head impacts in fmri brain activation change," *Developmental neuropsychology*, vol. 40, no. 2, pp. 74–79, 2015.

[167] T. E. Shenk, M. E. Robinson, D. O. Svaldi, K. Abbas, K. M. Breedlove, L. J. Leverenz, E. A. Nauman, and T. M. Talavage, "Fmri of visual working memory in high school football players," *Developmental neuropsychology*, vol. 40, no. 2, pp. 63–68, 2015.

[168] B. Johnson, T. Neuberger, M. Gay, M. Hallett, and S. Slobounov, "Effects of subconcussive head trauma on the default mode network of the brain," *Journal of neurotrauma*, vol. 31, no. 23, pp. 1907–1913, 2014.

[169] Y. Zhou, M. P. Milham, Y. W. Lui, L. Miles, J. Reaume, D. K. Sodickson, R. I. Grossman, and Y. Ge, "Default-mode network disruption in mild traumatic brain injury," *Radiology*, vol. 265, no. 3, pp. 882–892, 2012.

[170] D. C. Zhu, T. Covassin, S. Nogle, S. Doyle, D. Russell, R. L. Pearson, J. Monroe, C. M. Liszewski, J. K. DeMarco, and D. I. Kaufman, "A potential biomarker in sports-related concussion: brain functional connectivity alteration of the default-mode network measured with longitudinal resting-state fmri over thirty days," *Journal of neurotrauma*, vol. 32, no. 5, pp. 327–341, 2015.

[171] R. Zhu, G. L. Huang, H. Yoon, C. S. Smith, and V. K. Varadan, "Biomechanical strain analysis at the interface of brain and nanowire electrodes on a neural probe," p. 031001, 2011.

[172] E. J. Matser, A. G. Kessels, M. D. Lezak, B. D. Jordan, and J. Troost, "Neuropsychological impairment in amateur soccer players," *Jama*, vol. 282, no. 10, pp. 971–973, 1999.

[173] A. D. Witol and F. M. Webbe, "Soccer heading frequency predicts neuropsychological deficits," *Archives of Clinical Neuropsychology*, vol. 18, no. 4, pp. 397–417, 2003.

[174] M. L. Lipton, N. Kim, M. E. Zimmerman, M. Kim, W. F. Stewart, C. A. Branch, and R. B. Lipton, "Soccer heading is associated with white matter microstructural and cognitive abnormalities," *Radiology*, vol. 268, no. 3, pp. 850–857, 2013.

[175] I. K. Koerte, E. Nichols, Y. Tripodis, V. Schultz, S. Lehner, R. Igbinoba, A. Z. Chuang, M. Mayinger, E. M. Klier, M. Muehlmann *et al.*, "Impaired cognitive performance in youth athletes exposed to repetitive head impacts," *Journal of neurotrauma*, vol. 34, no. 16, pp. 2389–2395, 2017.

[176] I. K. Koerte, A. P. Lin, M. Muehlmann, S. Merugumala, H. Liao, T. Starr, D. Kaufmann, M. Mayinger, D. Steffinger, B. Fisch *et al.*, "Altered neurochemistry in former professional soccer players without a history of concussion," *Journal of neurotrauma*, vol. 32, no. 17, pp. 1287–1293, 2015.

[177] M. R. Zhang, S. D. Red, A. H. Lin, S. S. Patel, and A. B. Sereno, "Evidence of cognitive dysfunction after soccer playing with ball heading using a novel tablet-based approach," *PloS one*, vol. 8, no. 2, p. e57364, 2013.

[178] W. F. Stewart, N. Kim, C. S. Ifrah, R. B. Lipton, T. A. Bachrach, M. E. Zimmerman, M. Kim, and M. L. Lipton, "Symptoms from repeated intentional and unintentional head impact in soccer players," *Neurology*, vol. 88, no. 9, pp. 901–908, 2017.

[179] D. O. Svaldi, E. C. McCuen, C. Joshi, M. E. Robinson, Y. Nho, R. Hannemann, E. A. Nauman, L. J. Leverenz, and T. M. Talavage, "Cerebrovascular reactivity changes in asymptomatic female athletes attributable to high school soccer participation," *Brain imaging and behavior*, vol. 11, no. 1, pp. 98–112, 2017.

[180] J. W. OKane, A. Spieker, M. R. Levy, M. Neradilek, N. L. Polissar, and M. A. Schiff, "Concussion among female middle-school soccer players," *JAMA pediatrics*, vol. 168, no. 3, pp. 258–264, 2014.

[181] E. McCuen, D. Svaldi, K. Breedlove, N. Kraz, B. Cummiskey, E. L. Breedlove, J. Traver, K. F. Desmond, R. E. Hannemann, E. Zanath *et al.*, "Collegiate women's soccer players suffer greater cumulative head impacts than their high school counterparts," *Journal of biomechanics*, vol. 48, no. 13, pp. 3720–3723, 2015.

[182] B. Cummiskey, D. Schiffmiller, T. M. Talavage, L. Leverenz, J. J. Meyer, D. Adams, and E. A. Nauman, "Reliability and accuracy of helmet-mounted and head-mounted devices used to measure head accelerations," *Proceedings of the Institution of Mechanical Engineers, Part P: Journal of Sports Engineering and Technology*, vol. 231, no. 2, pp. 144–153, 2017.

[183] J. Caffy, "The whiplash shaken infant syndrome: Manual shaking by the extremities with whiplash-induced intracranial and intraocular bleeds, linked with residual permanent brain damage and mental retardation," *Pediatrics*, vol. 54, pp. 396–403, 1974.

[184] A. N. Guthkelch, "Infantile subdural haematoma and its relationship to whiplash injuries," *Br Med J*, vol. 2, no. 5759, pp. 430–431, 1971.

[185] L. Barnsley, S. Lord, and N. Bogduk, "Whiplash injury," *Pain*, vol. 58, no. 3, pp. 283–307, 1994.

[186] K. Kentaro, T. Mamoru, K. Satoru, N. Masaru, K. Keiji, N. Takayuki, and K. Naoki, "Activated irregular spike and wave complex in traumatic cervical syndrome," *Brain and Nerve* , vol. 24, no. 1, pp. 49–55, 1972.

[187] A. K. Ommaya, F. Faas, and P. Yarnell, "Whiplash injury and brain damage: an experimental study," *Jama*, vol. 204, no. 4, pp. 285–289, 1968.

[188] F. TORRES and S. K. Shapiro, "Electroencephalograms in whiplash injury: a comparison of electroencephalographic abnormalities with those present in closed head injuries," *Archives of neurology*, vol. 5, no. 1, pp. 28–35, 1961.

[189] J. R. Gay and K. H. Abbott, "Common whiplash injuries of the neck," *Journal of the American Medical Association*, vol. 152, no. 18, pp. 1698–1704, 1953.

[190] A. Dmitrienko, C. Chuang-Stein, and R. B. D'Agostino, *Pharmaceutical statistics using SAS: a practical guide*. SAS Institute, 2007.

[191] K. M. Breedlove, E. L. Breedlove, M. Robinson, V. N. Poole, J. R. King, P. Rosenberger, M. Rasmussen, T. M. Talavage, L. J. Leverenz, and E. A. Nauman, "Detecting neurocognitive and neurophysiological changes as a result of subconcussive blows among high school football athletes," *Athletic Training and Sports Health Care*, vol. 6, no. 3, pp. 119–127, 2014.

[192] K. M. Guskiewicz, J. P. Mihalik, V. Shankar, S. W. Marshall, D. H. Crowell, S. M. Oliaro, M. F. Ciocca, and D. N. Hooker, "Measurement of head impacts in collegiate football players: relationship between head impact biomechanics and acute clinical outcome after concussion," *Neurosurgery*, vol. 61, no. 6, pp. 1244–1253, 2007.

[193] J. M. Stamm, A. P. Bourlas, C. M. Baugh, N. G. Fritts, D. H. Daneshvar, B. M. Martin, M. D. McClean, Y. Tripodis, and R. A. Stern, "Age of first exposure to football and later-life cognitive impairment in former NFL players," *Neurology*, vol. 84, no. 11, pp. 1114–1120, Mar 2015.

[194] M. L. Alosco, J. Mez, Y. Tripodis, P. T. Kiernan, B. Abdolmohammadi, L. Murphy, N. W. Kowall, T. D. Stein, B. R. Huber, L. E. Goldstein *et al.*, "Age of first exposure to tackle football and chronic traumatic encephalopathy," *Annals of neurology*, vol. 83, no. 5, pp. 886–901, 2018.

[195] G. E. Schneider, "Is it really better to have your brain lesion early? a revision of the kennard principle," *Neuropsychologia*, vol. 17, no. 6, pp. 557–583, 1979.

[196] M. Field, M. W. Collins, M. R. Lovell, and J. Maroon, "Does age play a role in recovery from sports-related concussion? a comparison of high school and collegiate athletes," *The Journal of pediatrics*, vol. 142, no. 5, pp. 546–553, 2003.

[197] R. Pullela, J. Raber, T. Pfankuch, D. M. Ferriero, C. P. Claus, S.-E. Koh, T. Yamauchi, R. Rola, J. R. Fike, and L. J. Noble-Haeusslein, "Traumatic injury to the immature brain results in progressive neuronal loss, hyperactivity and delayed cognitive impairments," *Developmental neuroscience*, vol. 28, no. 4-5, pp. 396–409, 2006.

[198] A. V. Lavallee, R. P. Ching, and D. J. Nuckley, "Developmental biomechanics of neck musculature," *Journal of biomechanics*, vol. 46, no. 3, pp. 527–534, 2013.

[199] R. C. Cantu and M. Hyman, *Concussions and our kids: America's leading expert on how to protect young athletes and keep sports safe.* Houghton Mifflin Harcourt, 2012.

[200] V. N. Poole, K. Abbas, T. E. Shenk, E. L. Breedlove, K. M. Breedlove, M. E. Robinson, L. J. Leverenz, E. A. Nauman, T. M. Talavage, and U. Dydak, "Mr spectroscopic evidence of brain injury in the non-diagnosed collision sport athlete," *Developmental neuropsychology*, vol. 39, no. 6, pp. 459–473, 2014.

[201] V. N. Poole, E. L. Breedlove, T. E. Shenk, K. Abbas, M. E. Robinson, L. J. Leverenz, E. A. Nauman, U. Dydak, and T. M. Talavage, "Sub-concussive hit characteristics predict deviant brain metabolism in football athletes," *Developmental neuropsychology*, vol. 40, no. 1, pp. 12–17, 2015.

[202] E. A. Nauman, K. M. Breedlove, E. L. Breedlove, T. M. Talavage, M. E. Robinson, and L. J. Leverenz, "Post-season neurophysiological deficits assessed by impact and fmri in athletes competing in american football," *Developmental neuropsychology*, vol. 40, no. 2, pp. 85–91, 2015.

[203] K. Merchant-Borna, P. Asselin, D. Narayan, B. Abar, C. M. Jones, and J. J. Bazarian, "Novel method of weighting cumulative helmet impacts improves correlation with brain white matter changes after one football season of subconcussive head blows," *Annals of biomedical engineering*, vol. 44, no. 12, pp. 3679–3692, 2016.

[204] S. P. Broglio, T. Surma, and J. A. Ashton-Miller, "High school and collegiate football athlete concussions: a biomechanical review," *Annals of biomedical engineering*, vol. 40, no. 1, pp. 37–46, 2012.

[205] J. T. Eckner, M. Sabin, J. S. Kutcher, and S. P. Broglio, "No evidence for a cumulative impact effect on concussion injury threshold," *Journal of neurotrauma*, vol. 28, no. 10, pp. 2079–2090, 2011.

[206] B. Schnebel, J. T. Gwin, S. Anderson, and R. Gatlin, "In vivo study of head impacts in football: a comparison of national collegiate athletic association division i versus high school impacts," *Neurosurgery*, vol. 60, no. 3, pp. 490–496, 2007.

[207] S. M. Duma, S. J. Manoogian, W. R. Bussone, P. G. Brolinson, M. W. Goforth, J. J. Donnenwerth, R. M. Greenwald, J. J. Chu, and J. J. Crisco, "Analysis of real-time head accelerations in collegiate football players," *Clinical Journal of Sport Medicine*, vol. 15, no. 1, pp. 3–8, 2005.

[208] J. J. Crisco, R. Fiore, J. G. Beckwith, J. J. Chu, P. G. Brolinson, S. Duma, T. W. McAllister, A.-C. Duhaime, and R. M. Greenwald, "Frequency and location of head impact exposures in individual collegiate football players," *Journal of athletic training*, vol. 45, no. 6, pp. 549–559, 2010.

[209] J. P. Mihalik, D. R. Bell, S. W. Marshall, and K. M. Guskiewicz, "Measurement of head impacts in collegiate football players: an investigation of positional and event-type differences," *Neurosurgery*, vol. 61, no. 6, pp. 1229–1235, Dec 2007.

[210] K. M. Guskiewicz, S. W. Marshall, J. Bailes, M. McCrea, H. P. Harding, Jr, A. Matthews, J. R. Mihalik, and R. C. Cantu, "Recurrent concussion and risk of depression in retired professional football players," *Med. Sci. Sports Exerc.*, vol. 39, no. 6, pp. 903–909, Jun. 2007.

[211] A. H. Ropper and K. C. Gorson, "Concussion," *New England Journal of Medicine*, vol. 356, no. 2, pp. 166–172, 2007.

[212] K. Blennow, J. Hardy, and H. Zetterberg, "The neuropathology and neurobiology of traumatic brain injury," *Neuron*, vol. 76, no. 5, pp. 886–899, 2012.

[213] D. H. Smith, V. E. Johnson, and W. Stewart, "Chronic neuropathologies of single and repetitive tbi: substrates of dementia?" *Nature Reviews Neurology*, vol. 9, no. 4, p. 211, 2013.

[214] K. M. Guskiewicz, S. W. Marshall, J. Bailes, M. McCrea, R. C. Cantu, C. Randolph, and B. D. Jordan, "Association between recurrent concussion and late-life cognitive impairment in retired professional football players," *Neurosurgery*, vol. 57, no. 4, pp. 719–726, 2005.

[215] B. E. Gavett, R. A. Stern, R. C. Cantu, C. J. Nowinski, and A. C. McKee, "Mild traumatic brain injury: a risk factor for neurodegeneration," *Alzheimer's research & therapy*, vol. 2, no. 3, p. 18, 2010.

[216] S. M. Slobounov, A. Walter, H. C. Breiter, D. C. Zhu, X. Bai, T. Bream, P. Seidenberg, X. Mao, B. Johnson, and T. M. Talavage, "The effect of repetitive subconcussive collisions on brain integrity in collegiate football players over a single football season: a multi-modal neuroimaging study," *Neuroimage: clinical*, vol. 14, pp. 708–718, 2017.

[217] D. O. Svaldi, C. Joshi, M. E. Robinson, T. E. Shenk, K. Abbas, E. A. Nauman, L. J. Leverenz, and T. M. Talavage, "Cerebrovascular reactivity alterations in asymptomatic high school football players," *Developmental neuropsychology*, vol. 40, no. 2, pp. 80–84, 2015.

[218] S. P. Broglio, J. J. Sosnoff, S. Shin, X. He, C. Alcaraz, and J. Zimmerman, "Head impacts during high school football: a biomechanical assessment," *Journal of athletic training*, vol. 44, no. 4, pp. 342–349, 2009.

[219] S. P. Broglio, J. T. Eckner, D. Martini, J. J. Sosnoff, J. S. Kutcher, and C. Randolph, "Cumulative head impact burden in high school football," *Journal of neurotrauma*, vol. 28, no. 10, pp. 2069–2078, 2011.

[220] D. Nevins, L. Smith, and J. Kensrud, "Laboratory evaluation of wireless head impact sensor," *Procedia Engineering*, vol. 112, pp. 175–179, 2015.

[221] M. L. Dashnaw, A. L. Petraglia, and J. E. Bailes, "An overview of the basic science of concussion and subconcussion: where we are and where we are going," *Neurosurgical focus*, vol. 33, no. 6, p. E5, 2012.

[222] O. Salvado, C. Hillenbrand, S. Zhang, and D. L. Wilson, "Method to correct intensity inhomogeneity in mr images for atherosclerosis characterization," *IEEE transactions on medical imaging*, vol. 25, no. 5, pp. 539–552, 2006.

[223] P. Perona and J. Malik, "Scale-space and edge detection using anisotropic diffusion," *IEEE Trans. Pattern Anal. Mach. Intell.*, vol. 12, no. 7, pp. 629–639, 1990.

[224] Y. Zhang, B. J. Matuszewski, L.-K. Shark, and C. J. Moore, "Medical image segmentation using new hybrid Level-Set method," in *2008 Fifth International Conference BioMedical Visualization: Information Visualization in Medical and Biomedical Informatics*, 2008.

[225] Marcel Lüthi, Anita Lerch, Thomas Albrecht, Zdzislaw Krol, Thomas Vetter, "A hierarchical, multi-resolution approach for model-based skull-segmentation in mri volumes," *Conference Proceedings D*, vol. 3, 2009.

[226] B. O. Igbinedion and O. U. Ogbeide, "Measurement of normal ocular volume by the use of computed tomography. - PubMed - NCBI," https://www.ncbi.nlm.nih.gov/pubmed/23771452, accessed: 2019-2-11.

[227] C. E. Clauser, J. T. McConville, and J. W. Young, "Weight, volume, and center of mass of segments of the human body," Antioch Coll Yellow Springs OH, Tech. Rep., 1969.

[228] A. K. Miller, R. L. Alston, and J. A. Corsellis, "Variation with age in the volumes of grey and white matter in the cerebral hemispheres of man: measurements with an image analyser," *Neuropathol. Appl. Neurobiol.*, vol. 6, no. 2, pp. 119–132, Mar. 1980.

[229] M. Desbrun, M. Meyer, P. Schröder, and A. H. Barr, "Implicit fairing of irregular meshes using diffusion and curvature flow," in *Proceedings of the 26th annual conference on Computer graphics and interactive techniques - SIGGRAPH '99*, 1999.

[230] A. Aitkenhead, "CONVERT_stl_to_sat," Jun. 2012.

[231] Qianqian Fang, Q. Fang, and D. A. Boas, "Tetrahedral mesh generation from volumetric binary and grayscale images," in *2009 IEEE International Symposium on Biomedical Imaging: From Nano to Macro*, 2009.

[232] S. Holcombe, "stlwrite," Nov. 2011.

[233] A. F. Roche, D. Mukherjee, S. Guo, and W. M. Moore, "Head circumference reference data: birth to 18 years," *Pediatrics*, vol. 79, no. 5, pp. 706–712, 1987.

[234] A. J. Padgaonkar, K. Krieger, and A. King, "Measurement of angular acceleration of a rigid body using linear accelerometers," *Journal of Applied Mechanics*, vol. 42, no. 3, pp. 552–556, 1975.

[235] B. Cummiskey, "Characterization and evaluation of head impact sensors and varsity football helmets [ms thesis]," *Purdue University, West Lafayette, Ind, USA*, 2015.

[236] Y. Chen and M. Ostoja-Starzewski, "Mri-based finite element modeling of head trauma: spherically focusing shear waves," *Acta Mechanica*, vol. 213, no. 1-2, pp. 155–167, 2010.

[237] A. S. Koivuniemi and K. J. Otto, "The depth, waveform and pulse rate for electrical microstimulation of the auditory cortex," *Conf Proc IEEE Eng Med Biol Soc*, vol. 2012, pp. 2489–2492, 2012.

[238] S. J. Wilks, A. S. Koivuniemi, S. Thongpang, J. C. Williams, and K. J. Otto, "Evaluation of micro-electrocorticographic electrodes for electrostimulation," *Conf Proc IEEE Eng Med Biol Soc*, vol. 2009, pp. 5510–5513, 2009.

[239] A. S. Koivuniemi, O. B. Regele, J. H. Brenner, and K. J. Otto, "Rat behavioral model for high-throughput parametric studies of intracortical microstimulation," *Conf Proc IEEE Eng Med Biol Soc*, vol. 2011, pp. 7541–7544, 2011.

[240] S. J. Wilks, T. J. Richner, S. K. Brodnick, D. R. Kipke, J. C. Williams, and K. J. Otto, "Voltage biasing, cyclic voltammetry, and electrical impedance spectroscopy for neural interfaces," *J Vis Exp*, no. 60, Feb 2012.

[241] V. Gilja, C. Pandarinath, C. H. Blabe, P. Nuyujukian, J. D. Simeral, A. A. Sarma, B. L. Sorice, J. A. Perge, B. Jarosiewicz, L. R. Hochberg, K. V. Shenoy, and J. M. Henderson, "Clinical translation of a high-performance neural prosthesis," *Nat. Med.*, vol. 21, no. 10, pp. 1142–1145, Oct. 2015.

[242] J. L. Collinger, B. Wodlinger, J. E. Downey, W. Wang, E. C. Tyler-Kabara, D. J. Weber, A. J. McMorland, M. Velliste, M. L. Boninger, and A. B. Schwartz, "High-performance neuroprosthetic control by an individual with tetraplegia," *The Lancet*, vol. 381, no. 9866, pp. 557–564, 2013.

[243] M. S. Schwartz, S. R. Otto, R. V. Shannon, W. E. Hitselberger, and D. E. Brackmann, "Auditory brainstem implants," *Neurotherapeutics*, vol. 5, no. 1, pp. 128–136, 2008.

[244] B. H. Bewernick, R. Hurlemann, A. Matusch, S. Kayser, C. Grubert, B. Hadrysiewicz, N. Axmacher, M. Lemke, D. Cooper-Mahkorn, M. X. Cohen *et al.*, "Nucleus accumbens deep brain stimulation decreases ratings of depression and anxiety in treatment-resistant depression," *Biological psychiatry*, vol. 67, no. 2, pp. 110–116, 2010.

[245] J. Subbaroyan, D. C. Martin, and D. R. Kipke, "A finite-element model of the mechanical effects of implantable microelectrodes in the cerebral cortex," *J. Neural Eng.*, vol. 2, no. 4, pp. 103–113, Dec. 2005.

[246] S. Takeuchi, T. Suzuki, K. Mabuchi, and H. Fujita, "3d flexible multichannel neural probe array," *Journal of micromechanics and microengineering*, vol. 14, no. 1, p. 104, 2003.

[247] C. Xie, J. Liu, T.-M. Fu, X. Dai, W. Zhou, and C. M. Lieber, "Three-dimensional macroporous nanoelectronic networks as minimally invasive brain probes," *Nat. Mater.*, vol. 14, no. 12, pp. 1286–1292, Dec. 2015.

[248] T. D. Y. Kozai, N. B. Langhals, P. R. Patel, X. Deng, H. Zhang, K. L. Smith, J. Lahann, N. A. Kotov, and D. R. Kipke, "Ultrasmall implantable composite microelectrodes with bioactive surfaces for chronic neural interfaces," *Nat. Mater.*, vol. 11, no. 12, pp. 1065–1073, Dec. 2012.

[249] H. Lee, R. V. Bellamkonda, W. Sun, and M. E. Levenston, "Biomechanical analysis of silicon microelectrode-induced strain in the brain," *J. Neural Eng.*, vol. 2, no. 4, pp. 81–89, Dec. 2005.

[250] A. Sridharan, J. K. Nguyen, J. R. Capadona, and J. Muthuswamy, "Compliant intracortical implants reduce strains and strain rates in brain tissue in vivo," *J. Neural Eng.*, vol. 12, no. 3, p. 036002, Jun. 2015.

[251] M. Polanco, S. Bawab, and H. Yoon, "Computational assessment of neural probe and brain tissue interface under transient motion," *Biosensors*, vol. 6, no. 2, p. 27, Jun. 2016.

[252] K. D. Wise, A. M. Sodagar, Y. Yao, M. N. Gulari, G. E. Perlin, and K. Najafi, "Microelectrodes, microelectronics, and implantable neural microsystems," pp. 1184–1202, 2008.

[253] L. Luan, X. Wei, Z. Zhao, J. J. Siegel, O. Potnis, C. A. Tuppen, S. Lin, S. Kazmi, R. A. Fowler, S. Holloway, A. K. Dunn, R. A. Chitwood, and C. Xie, "Ultraflexible nanoelectronic probes form reliable, glial scar–free neural integration," p. e1601966, 2017.

[254] A. Gilletti and J. Muthuswamy, "Brain micromotion around implants in the rodent somatosensory cortex," *Journal of neural engineering*, vol. 3, no. 3, p. 189, 2006.

[255] J. T. Neary, Y. Kang, K. A. Willoughby, and E. F. Ellis, "Activation of extracellular signal-regulated kinase by stretch-induced injury in astrocytes involves extracellular ATP and P2 purinergic receptors," *J. Neurosci.*, vol. 23, no. 6, pp. 2348–2356, Mar. 2003.

[256] L. Karumbaiah, T. Saxena, D. Carlson, K. Patil, R. Patkar, E. A. Gaupp, M. Betancur, G. B. Stanley, L. Carin, and R. V. Bellamkonda, "Relationship between intracortical electrode design and chronic recording function," *Biomaterials*, vol. 34, no. 33, pp. 8061–8074, 2013.

[257] S. C. Cotter, "A screening design for factorial experiments with interactions," p. 317, 1979.

[258] H. Lee, R. V. Bellamkonda, W. Sun, and M. E. Levenston, "Biomechanical analysis of silicon microelectrode-induced strain in the brain," *Journal of neural engineering*, vol. 2, no. 4, p. 81, 2005.

[259] A. Prasad, Q.-S. Xue, V. Sankar, T. Nishida, G. Shaw, W. J. Streit, and J. C. Sanchez, "Comprehensive characterization and failure modes of tungsten microwire arrays in chronic neural implants," *J. Neural Eng.*, vol. 9, no. 5, p. 056015, Oct. 2012.

[260] A. Shah Idil and N. Donaldson, "The use of tungsten as a chronically implanted material," *J. Neural Eng.*, vol. 15, no. 2, p. 021006, Apr. 2018.

[261] W. Zhang, "10.5405/jmbe.1444," p. 386, 2014.

[262] J. Subbaroyan and D. R. Kipke, "The role of flexible polymer interconnects in chronic tissue response induced by intracortical microelectrodes - a modeling and an in vivo study," in *2006 International Conference of the IEEE Engineering in Medicine and Biology Society*, 2006.

[263] H. C. Lee, F. Ejserholm, J. Gaire, S. Currlin, J. Schouenborg, L. Wallman, M. Bengtsson, K. Park, and K. J. Otto, "Histological evaluation of flexible neural implants; flexibility limit for reducing the tissue response?" *J. Neural Eng.*, vol. 14, no. 3, p. 036026, Jun. 2017.

[264] A. Sridharan, S. D. Rajan, and J. Muthuswamy, "Long-term changes in the material properties of brain tissue at the implant-tissue interface," *J. Neural Eng.*, vol. 10, no. 6, p. 066001, Dec. 2013.

[265] H. S. Sohal, A. Jackson, R. Jackson, G. J. Clowry, K. Vassilevski, A. O'Neill, and S. N. Baker, "The sinusoidal probe: a new approach to improve electrode longevity," *Front. Neuroeng.*, vol. 7, p. 10, Apr. 2014.

[266] H. H. Draz, S. R. I. Gabran, M. Basha, H. Mostafa, M. F. Abu-Elyazeed, and A. Zaki, "Comparative mechanical analysis of deep brain stimulation electrodes," *Biomed. Eng. Online*, vol. 17, no. 1, p. 123, Sep. 2018.

[267] J. P. Seymour and D. R. Kipke, "Neural probe design for reduced tissue encapsulation in CNS," *Biomaterials*, vol. 28, no. 25, pp. 3594–3607, Sep. 2007.

[268] K.-K. Lee, J. He, A. Singh, S. Massia, G. Ehteshami, B. Kim, and G. Raupp, "Polyimide-based intracortical neural implant with improved structural stiffness," *Journal of Micromechanics and Microengineering*, vol. 14, no. 1, p. 32, 2003.

[269] P. J. Rousche, D. S. Pellinen, D. P. Pivin, J. C. Williams, R. J. Vetter, and D. R. Kipke, "Flexible polyimide-based intracortical electrode arrays with bioactive capability," *IEEE Transactions on biomedical engineering*, vol. 48, no. 3, pp. 361–371, 2001.

[270] M. Polanco, S. Bawab, and H. Yoon, "Computational assessment of neural probe and brain tissue interface under transient motion," *Biosensors*, vol. 6, no. 2, p. 27, Jun. 2016.

[271] W. Zhang, Z. Li, M. Gilles, and D. Wu, "Mechanical simulation of neural electrode-brain tissue interface under various micromotion conditions," *J. Med. Biol. Eng*, vol. 34, pp. 386–392, 2014.

[272] G. T. Chen, J. H. Kung, and K. P. Beaudette, "Artifacts in computed tomography scanning of moving objects," in *Seminars in Radiation Oncology*, vol. 14, no. 1. Elsevier, 2004, pp. 19–26.

[273] J. H. Lewis and S. B. Jiang, "A theoretical model for respiratory motion artifacts in free-breathing ct scans," *Physics in Medicine & Biology*, vol. 54, no. 3, p. 745, 2009.

[274] J. R. v. S. de Koste, F. J. Lagerwaard, H. C. De Boer, M. R. Nijssen-Visser, and S. Senan, "Are multiple ct scans required for planning curative radiotherapy in lung tumors of the lower lobe?" *International Journal of Radiation Oncology* Biology* Physics*, vol. 55, no. 5, pp. 1394–1399, 2003.

[275] K. Ashrafi, Y. Tang, H. Britton, O. Domenge, D. Blino, A. J. Bushby, K. Shuturminska, M. den Hartog, A. Radaelli, A. H. Negussie, A. S. Mikhail, D. L. Woods, V. Krishnasamy, E. B. Levy, B. J. Wood, S. L. Willis, M. R. Dreher, and A. L. Lewis, "Characterization of a novel intrinsically radiopaque drug-eluting bead for image-guided therapy: Dc bead lumi," *Journal of Controlled Release*, vol. 250, pp. 36 – 47, 2017. [Online]. Available: http://www.sciencedirect.com/science/article/pii/S0168365917300561

[276] R. Duran, K. Sharma, M. R. Dreher, K. Ashrafi, S. Mirpour, M. Lin, R. E. Schernthaner, T. R. Schlachter, V. Tacher, A. L. Lewis *et al.*, "A novel inherently radiopaque bead for transarterial embolization to treat liver cancer-a pre-clinical study," *Theranostics*, vol. 6, no. 1, p. 28, 2016.

[277] E. B. Levy, V. P. Krishnasamy, A. L. Lewis, S. Willis, C. Macfarlane, V. Anderson, I. M. van der Bom, A. Radaelli, M. R. Dreher, K. V. Sharma *et al.*, "First human experience with directly image-able iodinated embolization microbeads," *Cardiovascular and interventional radiology*, vol. 39, no. 8, pp. 1177–1186, 2016.

[278] S. Sharma, E. G. Moros, M. Boerma, V. Sridharan, E. Y. Han, R. Clarkson, M. Hauer-Jensen, and P. M. Corry, "A novel technique for image-guided local heart irradiation in the rat," *Technol. Cancer Res. Treat.*, vol. 13, no. 6, pp. 593–603, Dec. 2014.

[279] A. Hagan, G. J. Phillips, W. M. Macfarlane, A. W. Lloyd, P. Czuczman, and A. L. Lewis, "Preparation and characterisation of vandetanib-eluting radiopaque beads for locoregional treatment of hepatic malignancies," *Eur. J. Pharm. Sci.*, vol. 101, pp. 22–30, Apr. 2017.

[280] H. C. Nam, B. Jang, and M. J. Song, "Transarterial chemoembolization with drug-eluting beads in hepatocellular carcinoma," *World J. Gastroenterol.*, vol. 22, no. 40, pp. 8853–8861, Oct 2016.

[281] R. Kuehl, P. S. Brunetto, A.-K. Woischnig, M. Varisco, Z. Rajacic, J. Vosbeck, L. Terracciano, K. M. Fromm, and N. Khanna, "Preventing implant-associated infections by silver coating," *Antimicrobial Agents and Chemotherapy*, vol. 60, no. 4, pp. 2467–2475, 2016. [Online]. Available: https://aac.asm.org/content/60/4/2467

[282] A. Singh, H. Zhu, and J. He, "Improving mechanical stiffness of coated benzocyclobutene (BCB) based neural implant," *Conf. Proc. IEEE Eng. Med. Biol. Soc.*, vol. 6, pp. 4298–4301, 2004.

[283] S. A. Oppelt, W. Zhang, and D. R. Tolan, "Specific regions of the brain are capable of fructose metabolism," *Brain research*, vol. 1657, pp. 312–322, 2017.

[284] S. Burleson, J. Baker, A. T. Hsia, and Z. Xu, "Use of 3D printers to create a patient-specific 3D bolus for external beam therapy," *J. Appl. Clin. Med. Phys.*, vol. 16, no. 3, p. 5247, May 2015.

[285] V. Malfroy Camine, H. A. Rüdiger, D. P. Pioletti, and A. Terrier, "Full-field measurement of micromotion around a cementless femoral stem using micro-CT imaging and radiopaque markers," *J. Biomech.*, vol. 49, no. 16, pp. 4002–4008, Dec. 2016.

[286] C. Sukjamsri, D. M. Geraldes, T. Gregory, F. Ahmed, D. Hollis, S. Schenk, A. Amis, R. Emery, and U. Hansen, "Digital volume correlation and micro-CT: An in-vitro technique for measuring full-field interface micromotion around polyethylene implants," *J. Biomech.*, vol. 48, no. 12, pp. 3447–3454, Sep. 2015.

[287] M. Gortchacow, M. Wettstein, D. P. Pioletti, and A. Terrier, "A new technique to measure micromotion distribution around a cementless femoral stem," *J. Biomech.*, vol. 44, no. 3, pp. 557–560, Feb. 2011.

[288] S. Patrick, N. P. Birur, K. Gurushanth, A. S. Raghavan, S. Gurudath *et al.*, "Comparison of gray values of cone-beam computed tomography with hounsfield units of multislice computed tomography: An in vitro study," *Indian Journal of Dental Research*, vol. 28, no. 1, p. 66, 2017.

[289] C. M. Zehendner, H. J. Luhmann, and J.-W. Yang, "A simple and novel method to monitor breathing and heart rate in awake and Urethane-Anesthetized newborn rodents," *PLoS One*, vol. 8, no. 5, 2013.

[290] L. M. Burk, Y. Z. Lee, J. M. Wait, J. Lu, and O. Z. Zhou, "Non-contact respiration monitoring for in-vivo murine micro computed tomography: characterization and imaging applications," *Phys. Med. Biol.*, vol. 57, no. 18, pp. 5749–5763, Sep. 2012.

APPENDICES

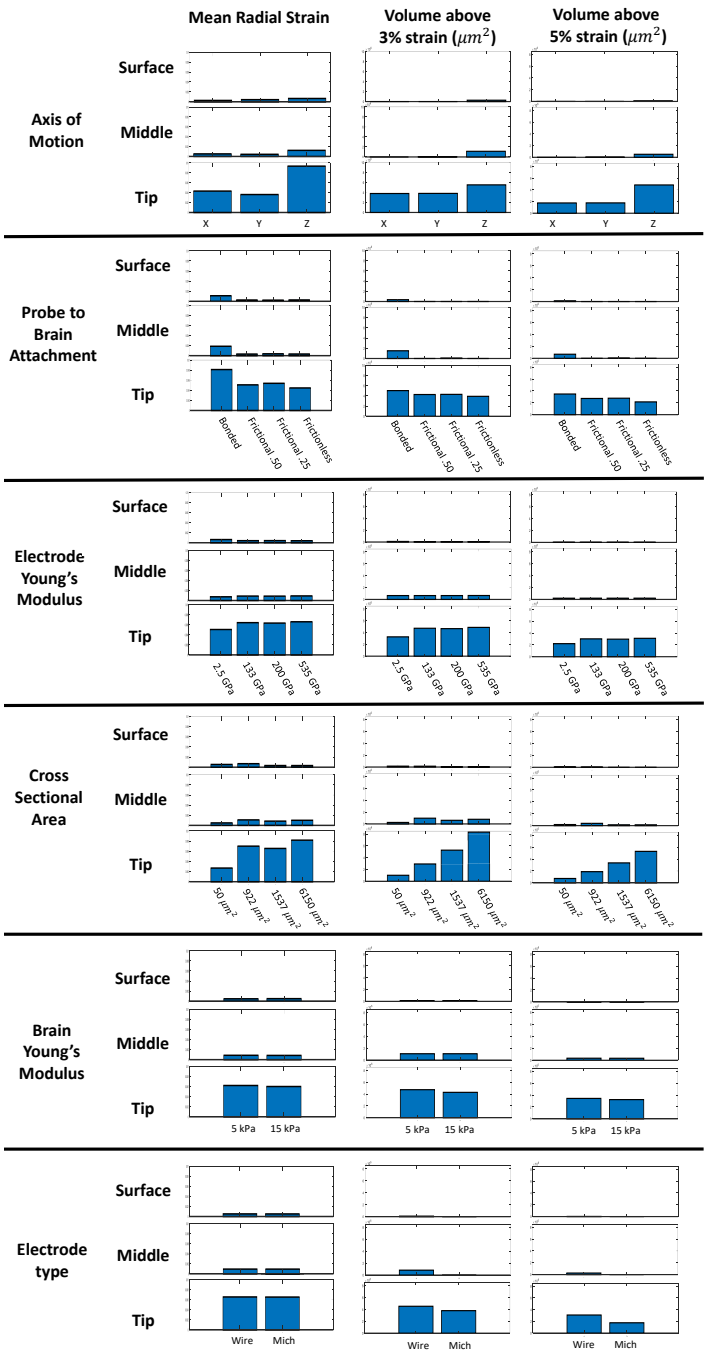

Fig. 1. Grouped measures for each design factor examined in this study. Each factor is examined for the weighted radial mean strain, maximum strain, the volume of the brain above 3% strain, the volume of the brain above 5% strain that they produce in the brain and for each region of the electrode (surface, middle, tip). Mean strains displayed range 0 to 0.1 and volumes measured range from 0 of 0.0085 mm3(units in μm^3).

VITA

VITA

Roy J. Lycke

2447 Kestral Blvd Apt G
West Lafayette, IN 47906

rlycke@purdue.edu
641-751-2354

Education

Doctorate of Philosophy — 2012 - May 2019
Purdue University — West Lafayette, IN
Biomedical Engineering

Masters of Science — 2011 - 2012
Iowa State University — Ames, IA
Computer Engineering

Bachelors of Science — 2006 - 2011
Iowa State University — Ames, IA
Computer Engineering

Research Interests

Brain-machine Interfaces, Neuroprostheses, Sensory Repair and Analysis, Neural Coding and Plasticity, Image Segmentation, MRI Analysis, Mechanical Modeling and Simulation

Research Experience

Graduate Research Assistant — August 2014 - Present
Purdue University — West Lafayette, IN
School of Mechanical Engineering — Advisor: Dr. Eric Nauman

Performed intra-lab and interdisciplinary, cross-college research projects investigating: traumatic brain injury, cellular mechanics, tissue & organ structure, athletic injury prevention, electrode design, and brain biomechanics. Developed novel software for analyzing and segmenting MRI brain scans, MicroCT tissue samples, and histological slices. Analyzed micro and macro biological systems utilizing finite element software. Mentored undergraduate and graduate researchers, performed cadaver dissections, developed course materials, invented sensored sports equipment, and rapid prototyped braces for Purdue Men's Basketball team.

Graduate Research Assistant — August 2012 – August 2014
Purdue University — West Lafayette, IN
School of Biomedical Engineering — Advisor: Dr. Kevin Otto

Designed and conducted in vivo animal studies investigating novel neural implants, their performance, and subsequent immune response. Developed new surgical techniques for device implementation and programs for analyzing recorded brain activity. Mentored undergraduate research students, designed research plans & experiments, and managed laboratory assets.

Graduate Research Assistant August 2010 – August 2012
Iowa State University Ames, IA
Department of Computer & Electrical Engineering Advisor: Santosh Pandey

Conducted research on *C elegans*, investigating response and efficacy to novel drug treatments. Designed novel microfluidic systems and fabricated devices for testing cellular cultures and micro-organisms in collaborative research.

Teaching Interests

Biomedical Engineering, Computer Engineering, Applied Physiology, Neuroscience, Neural Implants

Teaching Experience

College Course Design Fall 2018
Purdue University West Lafayette

Developed lecture material and laboratory curriculum for teaching programming, circuit design, and implementation of varied electronic components in a multi-computer system.

Volunteer Teaching Assistant Fall 2015
GK-12 Volunteer Program West Lafayette, IN
Purdue University

Taught regional middle schools students basics sciences and collaborated with teaching staff to improve existing lessons. Developed lessons and exploratory lab that was taught and implemented for future years.

SURF Mentor Summer 2014
Summer Undergraduate Research Fellowship Program West Lafayette, IN
Purdue University

Advised undergraduate researcher, instructing and teaching experimental techniques, research methods, and study design.

Awards

Robert B Truitt Fellowship Awarded 2017
Fearnot-Laufman-Greatbatch Award Awarded 2014
NSF Graduate Fellowship Award Awarded 2011

Professional Organizations

Tau Beta Pi (Engineering Honor Society)	Member Since 2008
Eta Kappa Nu (Electrical Engineering Honor Society)	Member Since 2009

Publications

Lee, T., Lycke, R., Lee, P., Cudal, C., Torolski, K., Bucherl, S., Molano, N., Auerbach, P., Talavage, T., Nauman, E. Distribution of Head Acceleration Events Varies by Position and Play Type in North American Football. *Clinical Journal of Sport Medicine*. (In Review)

Jang, I., Chun, I., Bari, S., Breedlove, E., Cummisky, B., Lee, T., Lycke, R., Poole, V., Shenk, T., Svaldi, D., Tamer, G., Leverenz, L., Nauman, E., Talavage, T. Every Hit Matters: White Matter Integrity Changes in High School Football Athletes Are Correlated with Repetitive Head Acceleration Event Exposure. *NeuroImage: Clinical*. (In Review)

Zhai, X., Nauman, E., Nie Y., Liao H., Lycke, R., Chen, W. Mechanical response of human muscle at intermediate strain rates. *Journal of Biomechanical Engineering*. (In Review)

Lycke, R., Walls, M., Calve, S. Computational modeling of developing cartilage using experimentally determined geometries and compressive moduli. *Journal of Biomechanical Engineering*. (In Review)

Lee, T., Lycke, R., Auger, J., Music, J., Dziekan, M., Newman, S., Talavage, T., Nauman, E. Head Acceleration Event Metrics in Youth Athletes More Dependent on Sport than Level of Play. *Journal of Applied Biomechanics*. (In Review)

Lycke, R., Kurfman, J., Nauman, E. (July 2018). A Model relating the Mechanical Properties of Neural Electrode Design and Chronic Neural Immune Response. World Congress of Biomechanics 2018 Conference. Dublin, Ireland.

Lin, J., Phillips, E., Riggins, T., Sangha, G., Chakraborty, S., Lee, J., Lycke, R., Hernandez, C., Soepriatna, A., Thorne, B., Yrineo, A., Goergen, C. (2015). Imaging of Small Animal Peripheral Artery Disease Models: Recent Advancements and Translational Potential. *International Journal of Molecular Sciences*, *16*(5), 11131–11177. doi:10.3390/ijms160511131

Lycke, R., Parashar, A., & Pandey, S. (2013). Microfluidics-enabled method to identify modes of Caenorhabditis elegans paralysis in four anthelmintics. *Biomicrofluidics*, *7*(6).

Lycke RJ, Schendel A, Williams JC, Otto. K. (2014). In vivo evaluation of a μECoG array for chronic stimulation. *Proc. of 36th Ann Conf EMBS*, 1294–1297. doi:10.1109/EMBC.2014.6943835

Pandey, S. (2011). Decision-making by nematodes in complex microfluidic mazes. *Advances in Bioscience and Biotechnology*, *02*(06), 409–415. doi:10.4236/abb.2011.26060

Parashar, A., Lycke, R., Carr, J. A., & Pandey, S. (2011). Amplitude-modulated sinusoidal microchannels for observing adaptability in C. elegans locomotion. *Biomicrofluidics*, *5*(2).